

2013-01-01

Exploring New Concepts In Directional Solidification By Electron Beam Melting and Selective Laser Melting

Edwin Martinez

University of Texas at El Paso, emartinez21@miners.utep.edu

Follow this and additional works at: https://digitalcommons.utep.edu/open_etd



Part of the [Engineering Commons](#)

Recommended Citation

Martinez, Edwin, "Exploring New Concepts In Directional Solidification By Electron Beam Melting and Selective Laser Melting" (2013). *Open Access Theses & Dissertations*. 1876.
https://digitalcommons.utep.edu/open_etd/1876

This is brought to you for free and open access by DigitalCommons@UTEP. It has been accepted for inclusion in Open Access Theses & Dissertations by an authorized administrator of DigitalCommons@UTEP. For more information, please contact lweber@utep.edu.

EXPLORING NEW CONCEPTS IN DIRECTIONAL SOLIDIFICATION BY
ELECTRON BEAM MELTING AND SELECTIVE LASER MELTING

EDWIN MARTINEZ

Department of Metallurgical and Materials Engineering

APPROVED:

Lawrence E. Murr, Ph.D., Chair

Stephen W. Stafford, Ph.D.

Russell R. Chianelli, Ph.D.

Benjamin C. Flores, Ph.D.
Dean of the Graduate School

Dedicated to my family and friends

EXPLORING NEW CONCEPTS IN DIRECTIONAL SOLIDIFICATION BY
ELECTRON BEAM MELTING AND SELECTIVE LASER MELTING

by

EDWIN MARTINEZ, BS

THESIS

Presented to the Faculty of the Graduate School of

The University of Texas at El Paso

in Partial Fulfillment

of the Requirements

for the Degree of

Master of Science

Department of Metallurgical and Materials Engineering

THE UNIVERSITY OF TEXAS AT EL PASO

May 2013

Acknowledgements

I would like to thank my mentor and advisor Dr. Lawrence E. Murr who took a chance with me coming out of high school and giving me the opportunity to be his research assistant as well as to learn from him. It has been a privilege to work for and to learn from one of the most recognized person in the field of Metallurgical and Materials Engineering. I would also like to thank the students and faculty from the Metallurgical and Material Engineering department; you have made my college experience one that I will forever treasure. I would also like to thank the students and the faculty from the W.M. Keck Center for 3D Innovation at the University of Texas at El Paso for providing the samples that I used to conduct my research. Finally I would like to thank all of my family for the love and support they provided every day throughout my educational journey.

Abstract

Unlike more conventional directional solidification, electron and laser-beam melting technologies involve building 3D components through layer-by-layer melt/solidification thermal cycling which creates novel, directional microstructural architectures. In this study we compared various the columnar microstructures of various components manufactured by EBM and SLM; image composite observations of columnar microstructural architectures in Cu, Co-29-Cr-6Mo-0.2C alloy, Ni-22Cr-9Mo-4Nb (alloy 625) fabricated by electron beam melting (EBM), and Ni-19Cr-19Fe-5Nb-1Al (alloy 718) by selective laser melting (SLM) as well as stainless steel 17-4 PH (SLM). Cu produced discontinuous columns of Cu_2O precipitates while the Co-base alloy exhibited similar columns of Cr_{23}C_6 precipitates. The alloy 625 produced columns of Ni_3Nb (γ'' -bct) precipitates. All of the EBM-produced columnar microstructure arrays were spaced $\sim 2\text{ }\mu\text{m}$. In contrast, the SLM fabricated alloy 718 contained columnar microstructural arrays of Ni_3Nb (γ'') spaced $\sim 0.8\mu\text{m}$, the 17-4 PH stainless steel produced martensitic structures dependent on the gas used for manufacturing. The manufactured components were observed by optical microscopy, SEM, XRD and by TEM in order to understand the microstructural development.

Table of Contents

Acknowledgements.....	iv
Abstract.....	v
Table of Contents.....	vi
List of Figures.....	viii
Chapter 1.....	1
Introduction.....	1
1.1 Electron Beam Melting (EBM)	2
1.2 Selective Laser Melting (SLM)	4
1.3 Experimental Equipment	6
1.4 Directional solidification	6
1.5 Eutectic Solidification	9
1.6 Building Strategies and Importance of Powder Properties	13
Chapter 2.....	15
Co-Base Superalloy Components by EBM	15
2.1 Optical Microscopy	15
2.2 Transmission Electron Microscopy	21
Chapter 3.....	26
Copper Components Fabricated by EBM.....	26
3.1 Optical Microscopy	26
3.2 Scanning Electron Microscopy.....	30
3.3 Transmission Electron Microscopy	32
Chapter 4.....	39
Manufacturing of Inconel 625 by EBM and SLM.....	39
4.1 Inconel 625 EBM Optical Microscopy.....	39
4.2 XRD and TEM of EBM Manufactured Components	43
4.3 Inconel 625 Manufactured by SLM.....	47

Chapter 5.....	54
17-4 PH Stainless Steel Microstructures from SLM	54
5.1 17-4 PH Stainless Steel Powders	54
5.2 Ar and N2 powder components manufactured in Argon.....	57
5.3 N2/N2 Manufactured Components	63
Chapter 6.....	71
Inconel 718 Manufactured by SLM.....	71
6.1 Inconel 718 powders and Fabrication	71
6.2 Microstructures for SLM fabricated components by LOM	72
6.3 XRD and TEM analysis.....	78
Chapter 7.....	82
Conclusion	82
References.....	83
Appendix.....	86
Publications.....	87
Presentations	92
Vita	96

List of Figures

Figures 1.1.1 Arcam A2 EBM system with schematic illustrating the inside of the machine	3
Figure 1.1.2 Example of powders used by EBM as seen by SEM	3
Figure 1.2.1 EOS M270 SLM system with diagram of inside of the machine.....	5
Figure 1.2.2a.) Columnar grains and melt pool center-oriented microstructures b.) Columnar microstructures associated with melt pool edges.....	5
Figure 1.4.1 Eutectic Solidification forming rod like or lamellar structure	8
Figure 1.4.2 Microstructure of polished MnSb	8
Figure 1.5.1 a) Showing a lamellar structure b) rod like structure	9
Figure 1.5.2 Eutectic diagram at T_E	11
Figure 1.5.3 a) Molar free energy at $T_E - T_0$ b) growth rate calculation model.....	12
Figure 1.5.4 Eutectic diagram showing relationship between ΔX and ΔX_0	12
Figure 1.6.1 Idealized powder packing a.) Top view b.) Small particle packing side view c.) Large particle packing side view	13
Figure 1.6.2 Schematic representation of the build process	14
Figure 2.1.1 Co-29Cr-6Mo-0.22C powder	16
Figure 2.1.2 Example of simple geometry components manufactured by EBM, arrow shows build direction	17
Figure 2.1.3 3D Micrograph showing carbide columns of Co-base superalloy by EBM, arrow shows build direction.....	18
Figure 2.1.4 Magnified LOM 3D micrograph of columnar carbides in Co-Base superalloy by EBM.....	19
Figure 2.1.5 Schematic representation for the development of columnar carbides in Co-base superalloy manufactured by EBM.....	20
Figure 2.2.1 3D TEM image showing columns formed by $Cr_{23}C_6$ carbides	22
Figure 2.2.2 Magnified 3D TEM image showing the cubic structure of the $Cr_{23}C_6$ carbides	23
Figure 2.2.3 a) $Cr_{23}C_6$ carbides and stacking faults b) isolated carbide c) and d) show cubic geometries of the $Cr_{23}C_6$ carbides.....	24
Figure 2.2.4 a) Horizontal micrograph showing $Cr_{23}C_6$ carbides as seen by light optical microscopy b) horizontal low mag view of carbides c) horizontal high mag view of carbides with SAED diffraction insert	25
Figure 3.1.1 Cross section of copper etched powder showing equiaxed like grains	27
Figure 3.1.2 Example of some meshes manufactured with copper powder	27
Figure 3.1.3 3D light optical micrograph showing columnar microstructures, arrow shows build direction	28
Figure 3.1.4 Magnified 3D LOM section of figure 3.1.3	29
Figure 3.2.1 Copper powder distribution with an average size of $65\ \mu m$	31
Figures 3.2.2 a) Cellular-like structure resultant from etch pits b) Magnified view of a section from image a).	31
Figures 3.2.3 SEM images from copper powder a) shows the grains in the etched powder b) magnified image of a) showing the etched out precipitates in the grain boundaries	32
Figure 3.3.1 Horizontal plane bright field TEM image showing precipitate-dislocation arrays.....	34
Figure 3.3.2 Magnified view for the horizontal plane showing precipitate-dislocation arrays with corresponding SAED insert [110].....	35
Figure 3.3.3 Vertical plane bright field TEM image showing precipitate-dislocations arrays with selective precipitate etching and corresponding SAED diffraction.....	36

Figure 3.3.4 3D TEM image showing Cu ₂ O precipitate-dislocation arrays in both horizontal and vertical plane, arrow is build direction	37
Figure 3.3.5 EBM geometry scan illustrating the formation of precipitate-dislocation arrays. Preheat scans, p(x) p(y) and melt scans m(x) m(y).	38
Figure 4.1.1 Inconel 625 powder as seen by SEM showing microdendritic structure	40
Figure 4.1.2 LOM cross section of etched Inconel 625 powders showing microdendritic structure	40
Figure 4.1.3 3D LOM image showing columnar microstructure, arrow shows build direction.....	41
Figure 4.1.4 LOM image composition showing columnar platelet precipitates.....	42
Figure 4.2.1 XRD spectra for Inconel 625 powders.....	44
Figure 4.2.2 XRD spectra horizontal and vertical planes for sample from figure 4.1.4.....	45
Figure 4.2.3 3D TEM image composition showing platelet precipitate arrays	46
Figure 4.3.1 Inconel 625 manufactured by SLM in z-axis showing columnar microstructure and melt pools.....	48
Figure 4.3.2 3D image composite of SLM component manufactured in xy axis.....	49
Figure 4.3.3 XRD Spectra for Z oriented component manufactured by SLM	50
Figure 4.3.4 XRD Spectra for xy oriented component manufactured by SLM.....	51
Figure 4.3.5 3D TEM image composition showing high dislocation density and columnar precipitates.....	52
Figure 4.3.6 a) LOM vertical plane b) low magnification SEM showing γ formation at melt pool c) magnified SEM image showing precipitation	53
Figure 5.1.1 a) cross section of argon atomized powder b) cross section of nitrogen atomized powder ..	54
Figure 5.1.2 a) argon atomized powder b) nitrogen atomized powder.....	55
Figure 5.1.3 XRD Spectra for precursor powders	56
Figure 5.2.1 Argon powder as fab in argon gas.....	58
Figure 5.2.2 XRD spectra for Ar/Ar components.....	59
Figure 5.2.3 Nitrogen powder as fab in argon gas.....	60
Figure 5.2.4 XRD spectra for N ₂ /Ar components.....	61
Figure 5.2.5 TEM image for vertical reference plane	62
Figure 5.3.1 N ₂ /N ₂ 3D LOM showing austenitic microstructure	64
Figure 5.3.2 XRD spectra for N ₂ /N ₂ manufactured component.....	65
Figure 5.3.3 TEM bright field image for the vertical reference plane N ₂ /N ₂ component	66
Figure 5.3.4 3D LOM of Ar-N ₂ alternating manufactured component	67
Figure 5.3.5 XRD spectra for top section of cylindrical component.....	68
Figure 5.3.6 3D LOM of bottom of cylinder of alternating gas component	69
Figure 5.3.7 XRD spectra for bottom portion of cylindrical component	70
Figure 6.1.1 a) Inconel 718 powder as seen by SEM b) Cross section LOM of etched powder.....	72
Figure 6.2.1 a) Melt pool feature seen in vertical plane b) columnar grains observed in vertical plane..	74
Figure 6.2.2 3D LOM for as-fabricated cylinder in argon (x-axis build).....	75
Figure 6.2.3 3D LOM for x-axis component manufactured in argon and HIPed in argon	76
Figure 6.2.4 Vertical plane view for x-axis fabricated component in nitrogen.....	76
Figure 6.2.5 z-axis manufactured component in argon gas and HIPed	77
Figure 6.3.1 XRD spectra of powder and as-fab components.....	79
Figure 6.3.2 3D TEM image composite showing dense precipitates	80
Figure 6.3.3 TEM image for vertical plane section of columnar precipitates	81

Chapter 1

Introduction

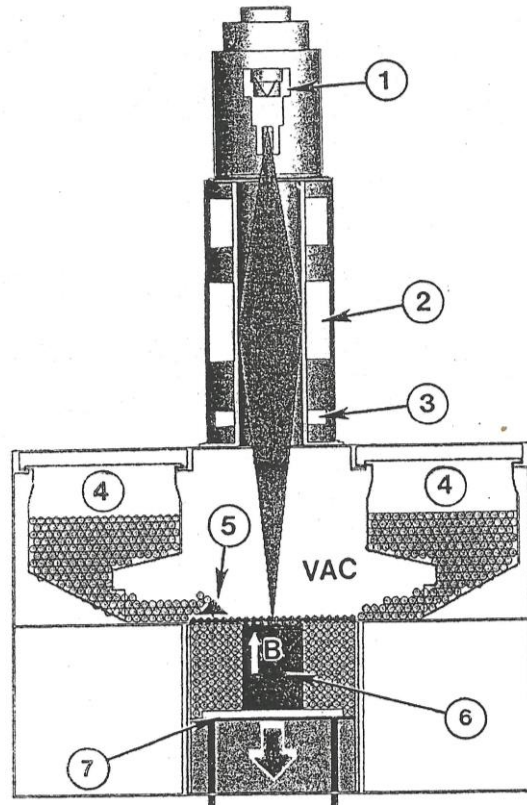
The focus of this thesis was to explore new concepts involving directional solidification and to analyze and compare the microstructures of many materials which were built by electron beam melting and selective laser melting, also known as additive manufacturing. Additive Manufacturing, or 3D printing, has become a worldwide phenomenon; this technology was initially off limits for commercial use but the improved development of such systems has made this possible. The advantage of this technology is that there is minimal material loss, 95% of the powder used in the build process can be recycled. A computer-aided design (CAD) is created and then uploaded into the printing system, the system is equipped with software that allows the user to change the layer thickness of the part as well as the desired size; most, if not all, of the printing systems use an STL file format. This technology has some major advantages compared to other manufacturing methods, you can create any geometry that you can imagine the only limitation is your CAD abilities and your imagination. Initially 3D printers were used to produce complex polymer prototypes but of course things improve and now we are also able to manufacture metallic components from metal powder by means of Electron Beam Melting (EBM) or by Selective Laser Melting (SLM). These systems allow us to build complex metallic components which can't be built by conventional processes of wrought or cast precursors. The best part of building metallic parts via layer by layer manufacturing of pre-alloyed powder is that we obtain some unique directional microstructures which are a result of a small melt pools which rapidly solidify. These unique microstructures, referred to as microstructural architecture, may provide for an improvement in mechanical properties of the metal as well as a vast improvement in performance.

Many components have been analyzed, which were manufactured by both EBM and SLM, these include a cobalt base superalloy, Inconel 625, Inconel 718, copper, and stainless steel 17-4. All of these components showed a microstructural architecture which was analyzed using optical microscopy, Scanning Electron Microscopy (SEM), Transmission Electron Microscopy (TEM), as well as X-ray Diffraction (XRD). By analyzing such components we can appreciate the importance of additive manufacturing and see how it can help improve our current technology especially in the context of new

directional solidification concepts. This thesis is a compilation of every material that I helped analyze throughout my academic career. To learn more about these materials please see the published works, seen in the appendix and in the references, on which this thesis is based.

1.1 ELECTRON BEAM MELTING (EBM)

The components which we analyzed came in a range of geometries from cylinders and blocks to foams and meshes; these were manufactured either by EBM or SLM. Both systems are unique but also share some similarities. The systems used to manufacture our samples were an Arcam A2 system which is manufactured by Arcam AB in Sweden and also an EOS M270 SLM which is manufactured by EOS GmbH located in Germany, these systems are the EBM and SLM respectively. In order to manufacture parts in the Arcam A2 system you take a pre-alloyed metallic powder and insert it into the powder containers. The Arcam A2 system can be seen in Figure 1.1.1 which also contains an image of the inner workings of the machine. (1) The EBM contains an electron optical column which generates electrons and are accelerated with a 60 kV potential, the electrons are then focused using (2) electromagnetic lenses and electromagnetically scanned by the CAD software (3) that is included in the system. (4) The powders in the EBM are gravity fed from the cassettes and are raked (5) onto the build table. Once we have a powder layer on our (7) build table the focused electron beam is initially scanned multiple times with a scan rate and beam current dependent on the material being used; this is done in order to preheat the powder bed, or initial layer, to ~ 0.5 to 0.8 of the melting temperature, T_m . The final melt scan has a reduced or increased scan rate and beam current which again depend on the material. The final melt scan produces melt pools or zones that are related to the diameter of the beam as well as the scan spacing, this is important in helping us understand the microstructures of our components. Note that the systems build chamber is in a vacuum of $<10^{-4}$ Torr and the powder is melted in layers of up to $50\text{ }\mu\text{m}$. As was mentioned earlier, the powders are gravity fed from the containers and after the initial layers of our components are built the build table is lowered (6) in order to allow for new powder to be raked onto the build table and the new layer can be built.



Figures 1.1.1 Arcam A2 EBM system with schematic illustrating the inside of the machine

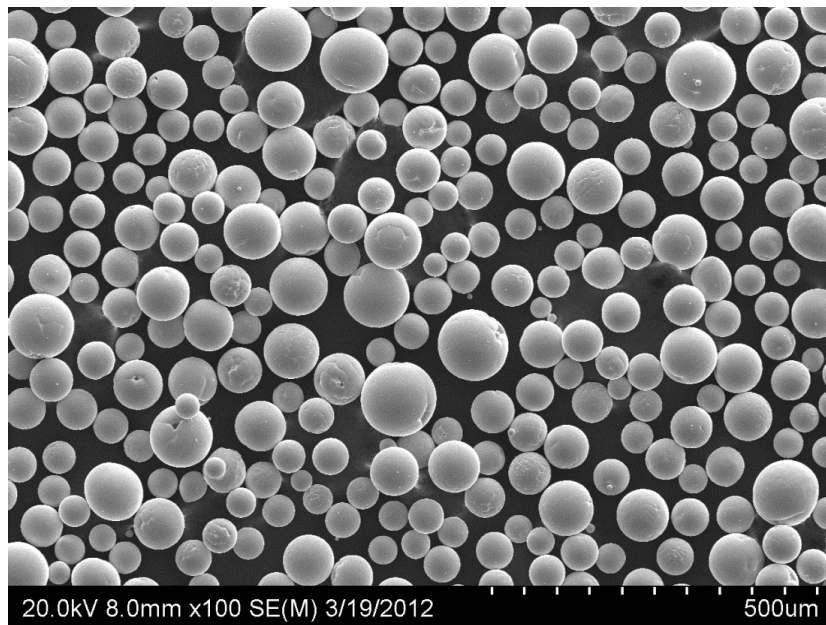


Figure 1.1.2 Example of powders used by EBM as seen by SEM

1.2 SELECTIVE LASER MELTING (SLM)

Unlike the EBM system which uses focused electron beams, the EOS M270 SLM system uses a focused laser beam with a 100 μm diameter; it utilizes a 0.2 kW Yb fiber: YAG fiber laser at a wavelength of 1070 nm. The EOS SLM system can be seen in figure 1.2.1 which also contains a diagram of the inside of the machine illustrating the built table and the laser among other components all labeled in the diagram. The laser is scanned by a CAD driven rotating mirror system and focused onto the powder bed. In contrast to the EBM which contains powder cassettes the SLM contains a powder feeder or supply container, the powder is not gravity fed but is raised from the powder feeder and then raked onto the build table; the raking system in the SLM is similar to the one found in the EBM. The SLM also contains an overflow container for the excess powder to drop onto. The build table is heated to $\sim 90^\circ\text{C}$ and it is roughly maintained to that temperature. The laser scans between 800 and 1200 mm/s in x-y and forms a melt pool similar to the ones formed by the EBM; note that the scanning can be in x-y or x or y in alternating layers. If you recall the EBM system had the build chamber in vacuum, in this case the SLM build chamber is in an argon or nitrogen (N_2) environment; this helps protect the powders from oxidation by purging the oxygen from the system. The thermal conductivity of nitrogen gas is about 40% higher than argon up to around 2000 K, the build cooling for the SLM system is usually more rapid than for the EBM. The powder sizes used in both the SLM and EBM can range from $\sim 10\ \mu\text{m}$ to 60 μm with a nominal size at around 40 μm . Both systems produce microstructural architectures and the grain growth in the systems takes place, or can be altered, because we can adjust the beam scan speed, beam size, scan spacing and the melt scan can be repeated in order to melt each layer again.

Both the EBM and SLM have formations of melt pools which are created in the x-y beam scanning; this is shown schematically in figures 1.2.2a and 1.2.2b which show columnar growth features near the center of the melt pools as well as cylindrical like microstructural features near the edges of the melt pool, respectively. The melt pool dimensions are dependent on the beam focus, scan rate and on the coupling of the beam with the raked or rolled powder layers. The slowest scanned electron beam usually produces a larger melt pool dimension than the more rapidly scanned laser beam.

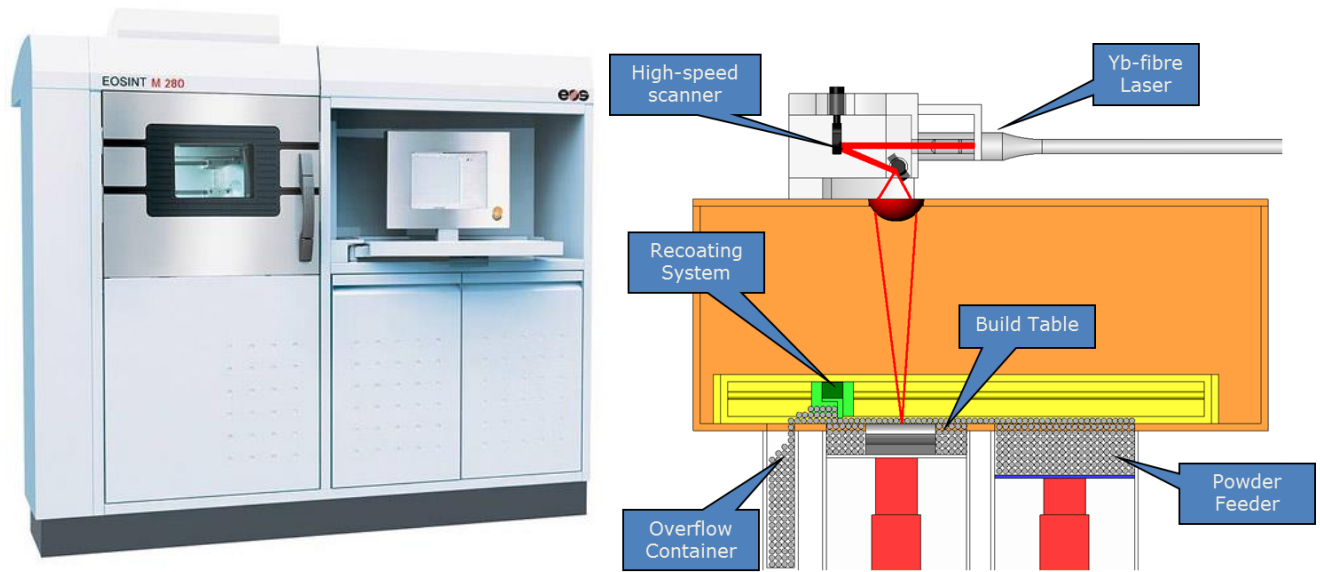


Figure 1.2.1 EOS M270 SLM system with diagram of inside of the machine

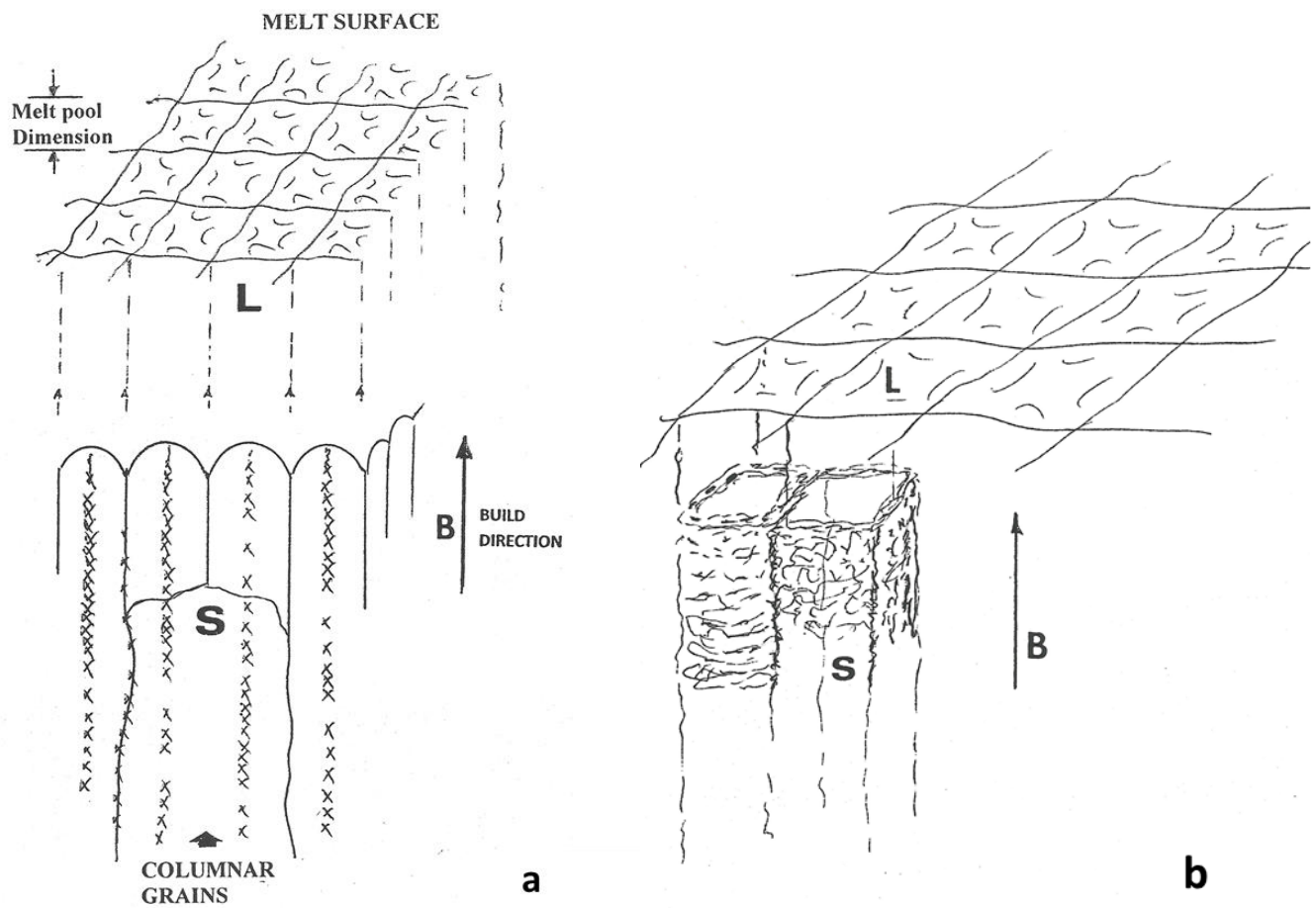


Figure 1.2.2 a.) Columnar grains and melt pool center-oriented microstructures b.) Columnar microstructures associated with melt pool edges

1.3 EXPERIMENTAL EQUIPMENT

All of the manufactured components were analyzed by light optical microscopy OM, using a Reichert MEF-4 A/M metallograph using digital image. The samples were all observed in both the horizontal, perpendicular to the build direction, and in the vertical plane, parallel to the build direction. They were all mounted, ground, polished and etched with different solutions and some with different methods. The manufactured components as well as the powders used were analyzed by x-ray diffraction (XRD) using a Brucker AXS-D8 Discover machine with a copper target; for the manufactured components the horizontal and vertical plane were analyzed. The Scanning Electron Microscopy (SEM) images were obtained using a Hitachi S-4800 field emission (FE) SEM fitted with an EDAX-EDS system; some of the images were taken in bright field and a few others were taken in dark field. The Transmission Electron Microscopy (TEM) images were obtained using a Hitachi H-9500, high resolution, digital imaging system operated at 300 kV. The samples were cut and ground up to a thickness of ~ 0.2 mm and coupons or discs of 3 mm were punched from the thin sections before they were electropolished using different solutions at different temperatures in order to be observed in the TEM, the solutions used will be mentioned in each material section. Hardness testing was also done on the samples by microindentation (Vickers-HV) hardness using a Shimadzu HMV-2000 digital measuring system.

1.4 DIRECTIONAL SOLIDIFICATION

The microstructural architecture that we obtain in our samples can be understood by fundamentals that were developed nearly one hundred years ago; these techniques are known as the Czochralski method and the Bridgeman method. The melting point is considered the temperature where the free energies of the solid and the liquid phases can co-exist in equilibrium. As solidification takes place the liquid that is found in front of the interface is at a temperature that is slightly lower than the equilibrium liquidus temperature, this is known as supercooled; this arises from a compositional change rather than a temperature change so it is known as constitutional supercooling. Single crystal growth for a single phase composition system can be achieved by taking a solid oriented seed crystal and pulling it from the melt or it may also be achieved by cooling molten material and moving it through a

temperature gradient in a furnace. In addition to crystal growth we also have dendritic solidification which happens because of rapid solidification, this is notable in most of the powder that was analyzed; it happens because it involves a small volume regime.

Directional solidification can also take place by binary eutectics. The solid phases α and β as can be seen in the eutectic phase diagram figure 1.4.1, will solidify from the liquid (L) simultaneously creating a unique structure. The α and β phases will grow in the direction noted by the arrow in figure 1.4.1, the now two-phase unidirectional eutectic can be lamellar or rod like structure and this will depend on the conditions for growth as well as the total free energy minimization; this type of structure is considered a composite because the rods add strength, in the growth direction, to the material. Figure 1.4.2 shows a 3D composition of light microscopy images containing fibers, dark rod phase, in the as-polished condition; the material is MnSb in Sb matrix. The MnSb microstructure provides a reference point to our microstructures, note this is considered a more conventional method compared to the new directional solidification that is associated with EBM and SLM. It is important to understand the fundamentals for directional solidification in order to understand and improve this type of solidification for our new systems.

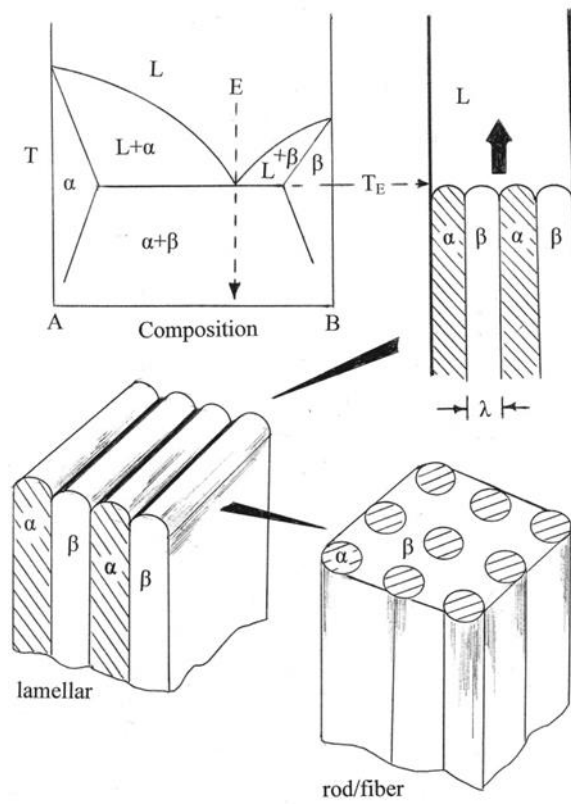


Figure 1.4.1 Eutectic Solidification forming rod like or lamellar structure

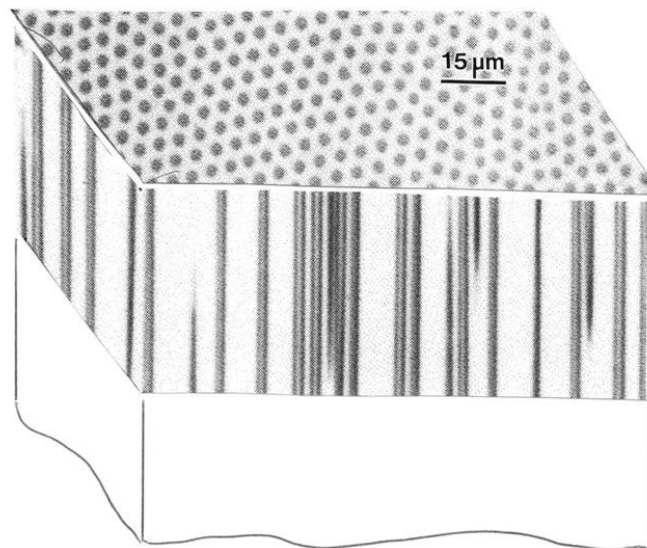


Figure 1.4.2 Microstructure of polished MnSb

1.5 EUTECTIC SOLIDIFICATION

Eutectic solidification is important because of the structures it can create like the ones seen in figure 1.5.1. Figure 1.5.1b shows rods of minor phase that are a part of the other phase, in essence they act like a composite, this phenomenon can also be seen in additive manufacturing of metallic samples where we have columnar grains and precipitates that are elongated similar to the rods found in figure 1.5.1b. Eutectic solidification is when two solid phases take place simultaneously from the liquid phase, $L \rightarrow \alpha + \beta$ and can be seen as normal and anomalous; normal structures are when the phases have low entropies of fusion and anomalous structures occur when one phase has high entropy compared to the other.

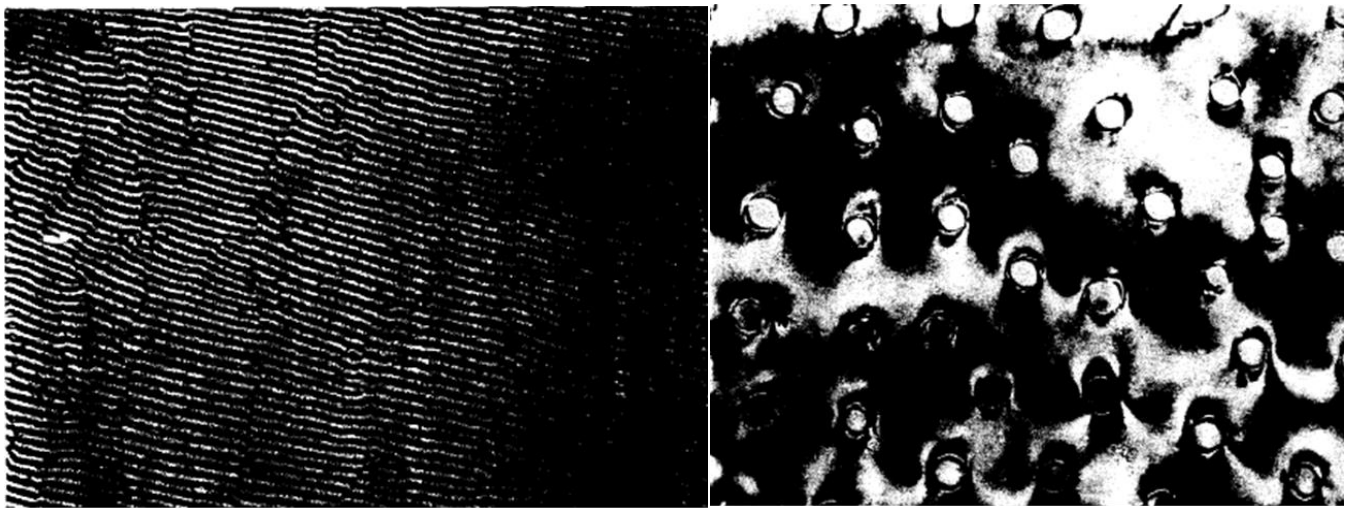


Figure 1.5.1 a) Showing a lamellar structure b) rod like structure

In figure 1.4.1 we can see how the α and β grow with the liquid, the growth occurs when say A-rich atoms from the α phase begin to solidify and the excess B atoms will diffuse into the β phase thus making the β phase grow; the α phase grows in a similar way by obtaining the excess A atoms that diffuse away from the β phase. As mentioned earlier we can obtain a lamellar structure or a rod/fiber like structure when we have the growth of the lamellar eutectics, the microstructures obtain will depend on the growth conditions and the total free energy minimization.

The eutectic growth rate will be dependent on the λ which is the interlamellar spacing as seen in figure 1.4.1; a small λ yields a fast growth rate while a large λ yields a slower growth rate. In order to determine the free energy change that is associated with solidification we can use

$$\Delta G(\lambda) = -\Delta G(\infty) + \frac{2\gamma_{\alpha\beta}V_m}{\lambda}$$

$\gamma_{\alpha\beta}$ is the interfacial energy in the system, V_m is the molar volume of the eutectic and $\Delta G(\infty)$ is the free energy decrease when λ is very high. From figure 1.5.2 we can see that as $\Delta G(\lambda)$ is positive then $\Delta G(\infty)$ must also be large in order to make up for the $\gamma_{\alpha\beta}$; our eutectic/liquid interface will have to be undercooled below the eutectic temperature. Figure 1.5.3(a) also shows that when the interlamellar spacing is

$$\lambda^* = \frac{2\gamma_{\alpha\beta}V_mT_E}{\Delta H \Delta T_0}$$

then all of the phases will be in equilibrium; the α/β raise the free energies of the phases from $\Delta G(\infty)$ to $\Delta G(\lambda^*)$. The increase in free energy will be different for both of the phases but in our case we are only considering a simple case which is $2\gamma_{\alpha\beta}V/\lambda$. When $\lambda=\lambda^*$ the growth will take a very long time because the liquid will be touching both α and the β phase meaning that the liquid will be at X_e , figure 1.5.2. It can be seen on figure 1.5.3 that when $\lambda>\lambda^*$ and we get a reduction in the free energies of α and β phases. When the eutectic growth rate is proportional to the flux of the solute through the liquid we can assume that the growth taking place is diffusion controlled, in turn the α and β interfaces with the liquid will be highly mobile. Figure 1.5.4 shows a eutectic phase diagram with relationship between ΔX and ΔX_0 , from this graph we can obtain the following equation

$$v = k_2 D \Delta T_0 \frac{1}{\lambda} \left(1 - \frac{\lambda^*}{\lambda}\right)$$

where v is the growth rate. This equation states that the growth rate and the interlamellar spacing will vary independently by varying the interface undercooling and it also states that at $\lambda = 2\lambda^*$ the growth

rate will be at its maximum capacity for a given undercooling; when the growth rate is max we can consider this to be optimum conditions. The total undercooling at the eutectic front has to contributions as given by

$$\Delta T_0 = \Delta T_r + \Delta T_D$$

ΔT_0 is the total undercooling, ΔT_r is the undercooling required to overcome interfacial curvature and ΔT_D is the undercooling required in order to drive the diffusion. The front of the eutectic as seen in figure 1.4.1 are not always stable and when this is the case we get cellular eutectic solidification; in order to obtain cellular eutectic solidification our alloy must contain some impurities which break up the interface. In the cell formation in eutectic alloys the planar interface can be controlled by solidifying in high temperatures. [1]

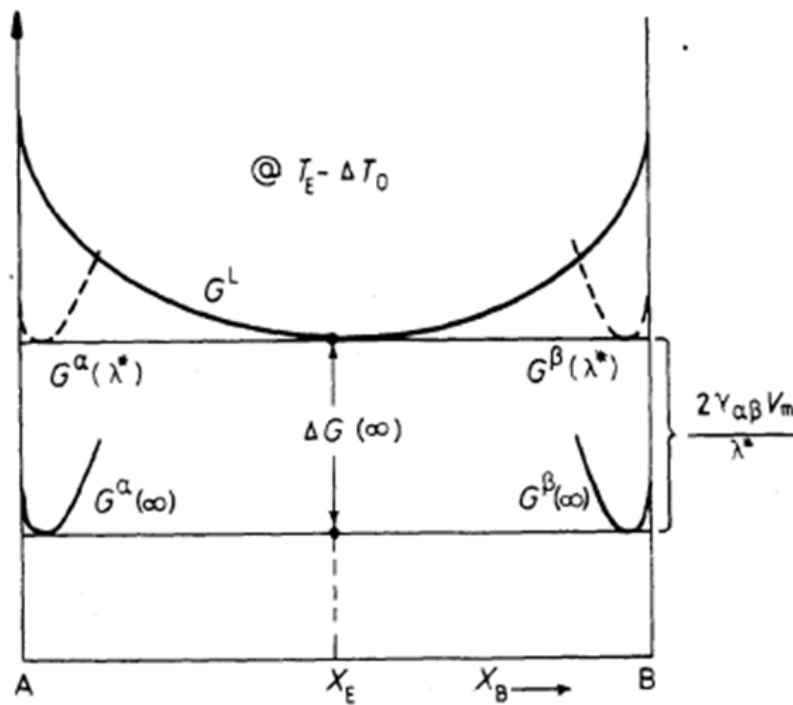


Figure 1.5.2 Eutectic diagram at T_E

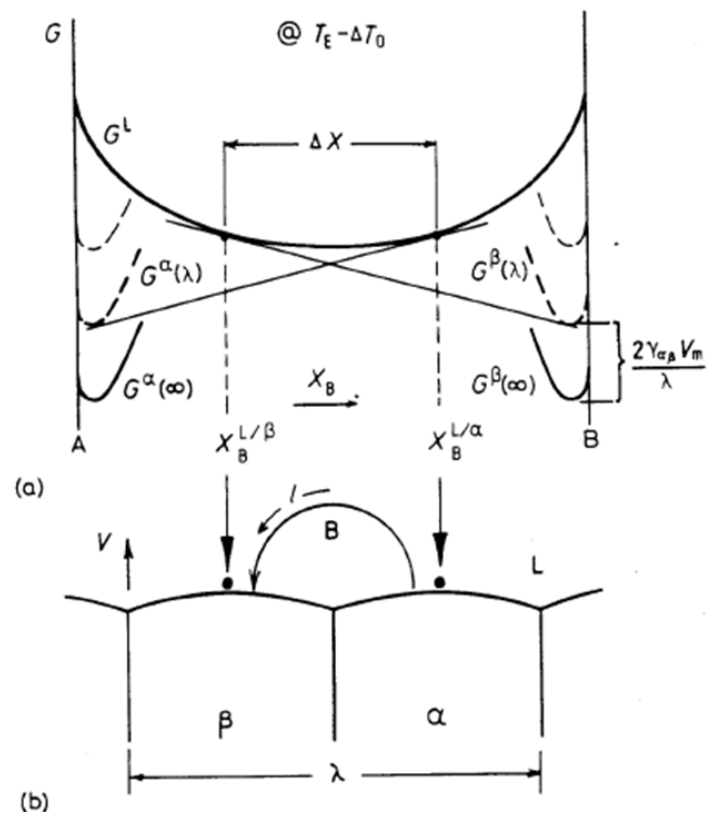


Figure 1.5.3 a) Molar free energy at $T_E - T_0$ b) growth rate calculation model

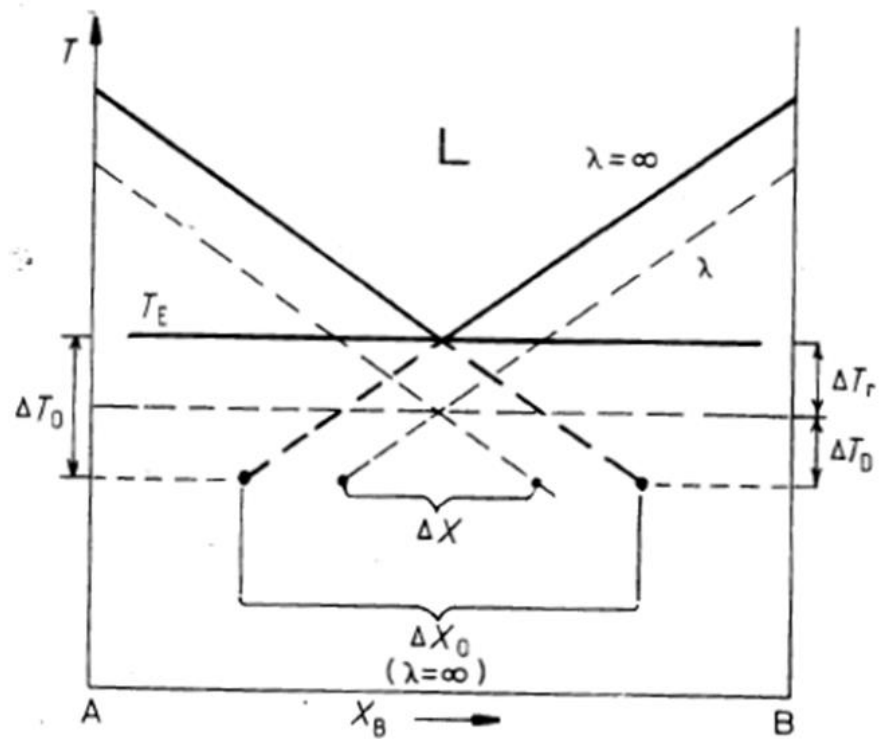


Figure 1.5.4 Eutectic diagram showing relationship between ΔX and ΔX_0

1.6 BUILDING STRATEGIES AND IMPORTANCE OF POWDER PROPERTIES

The packing of the powders with each new layer as well as the flow of the powders is very important for the EBM and SLM process. The flowability of the powder is affected by the shapes of the powders, if the powders are spherical the flowability will be high but if the powders have irregular shapes one can expect poor flowability. An example of good powder can be seen in figure 1.1.2. The smaller powder particles work best in the SLM system while powders with a good bimodal distribution work well in the EBM system where the smaller powder particles can fill voids in the layers and provide for a denser product. The illustration that can be seen in figure 1.6.1 shows the idealized powder packing which shows the smaller particles shown, in figure 1.6.1b, with a more packed layer than the large particles illustrated by figure 1.6.1c. The larger particles create voids which smaller powder particles can fill; this will enhance melting and sintering. Figure 1.6.2 is a schematic representation of the build process where the powder layers are selectively melting and eventually form a complex 3D component. The schematic also shows some unmelted powder, this powder can be reused in another build so no powder goes to waste. There are limitations in the feature size, $\sim 100\text{ }\mu\text{m}$, because of the layer melting and heat retention of the built products; smaller feature sizes will create sintered powdered in unmelted areas which prevents the powder from being removed. [8]

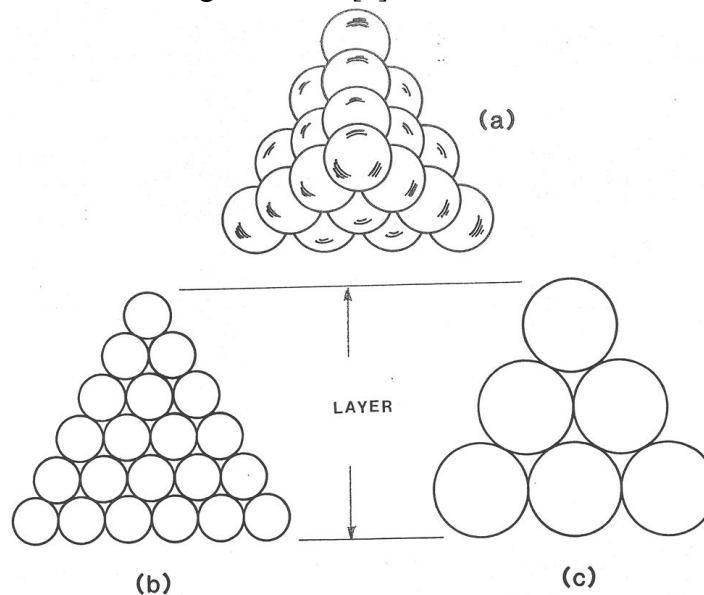


Figure 1.6.1 Idealized powder packing a.) Top view b.) Small particle packing side view c.) Large particle packing side view

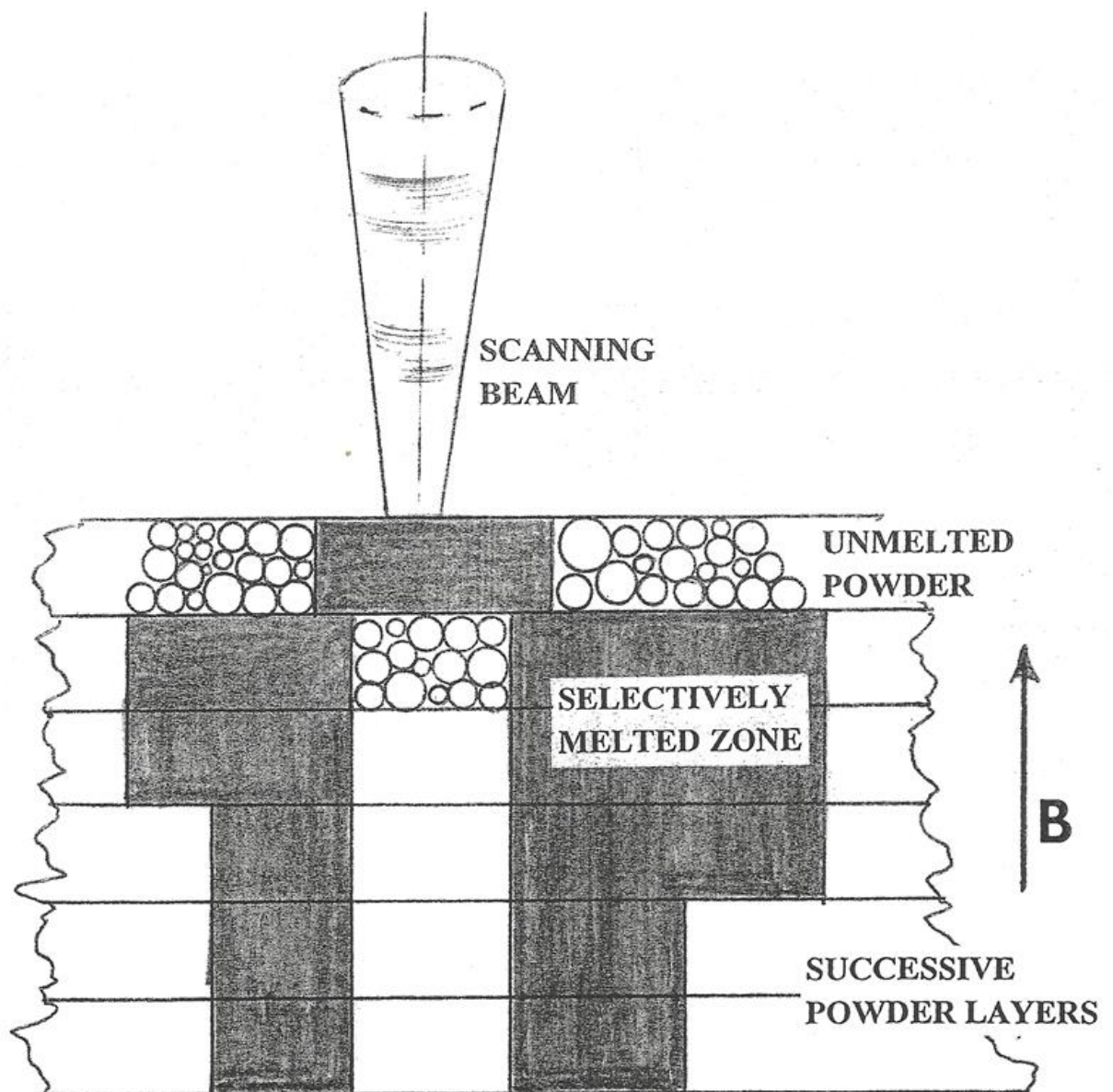


Figure 1.6.2 Schematic representation of the build process

Chapter 2

Co-Base Superalloy Components by EBM

2.1 OPTICAL MICROSCOPY

Some of the first components that we analyzed were cobalt base superalloys, Co-29Cr-6Mo-0.22C, many components were manufactured with different geometries; figure 2.1.2 shows an example of some geometries manufactured by EBM; arrow shows build direction. Cobalt base superalloys are important because they can be used in implants for people; the ability to manufacture components straight from CAD has a great advantage for this. No longer will we have set sizes for implants but the patient can have his/her custom fabricated implant by additive manufacturing, for more on this see Murr et al [6]. Figure 2.1.1 shows a magnified image of the Co-29Cr-6Mo-0.22C powder that was used to manufacture the components in the EBM, the powder had a nominal size of 40 μm . Sections from the components seen in figure 2.1.2, as well as other geometries, were cut, mounted, polished and etched in order to observe the microstructure; both the horizontal and vertical planes from the components were observed by light optical microscopy. The microstructure obtained showed a strong similarity to the MnSb microstructure that was previously mention, but in our case the Co-Cr was etched using a 6:1 solution of HCl:H₂O₂ for 16 hours at room temperature. This method was done before I knew of electrolytic etching which was done for some of the components which will be mentioned in the later sections. The etching process proved to be unconventional since the samples were left unattended for long periods of time, but the result obtained was acceptable. [7]

Figure 2.1.3 shows the strong similarity to the MnSb microstructure, in this figure we have a 3D micrograph depicting the horizontal and vertical planes of the components. The arrow in the image shows the build direction, as can be in the image the vertical plane shows some elongated grains and it also indicates that there is some carbide precipitate segregation. The spacing of the precipitates is more notable in the horizontal plane where we can calculate the spacing to be $\sim 2 \mu\text{m}$, the horizontal plane also has some equiaxed grains. Figure 2.1.4 is a magnified view of the columnar microstructure seen in the Co-Cr components; in this image we can see how the precipitate columns are discontinuous. The spacing of the carbides represents the approximate dimension of spatial x-y melt scans or melt pool

development in the powder layer; this is seen schematically in figure 2.1.4. The pre-heat and melt scans, $p(x) p(y)$ and $m(x) m(y)$ as noted in the figure, produce the thermal gradient and solidification velocity; these are determined by the scanning beam parameters like the beam focus, beam current and scan speed. Since the melt occurs in spatial pools in each layer, small variations in the beam parameters will affect the efficiency of the precipitate column formation which can produce continuity or discontinuity in the structure. [3,5,6]

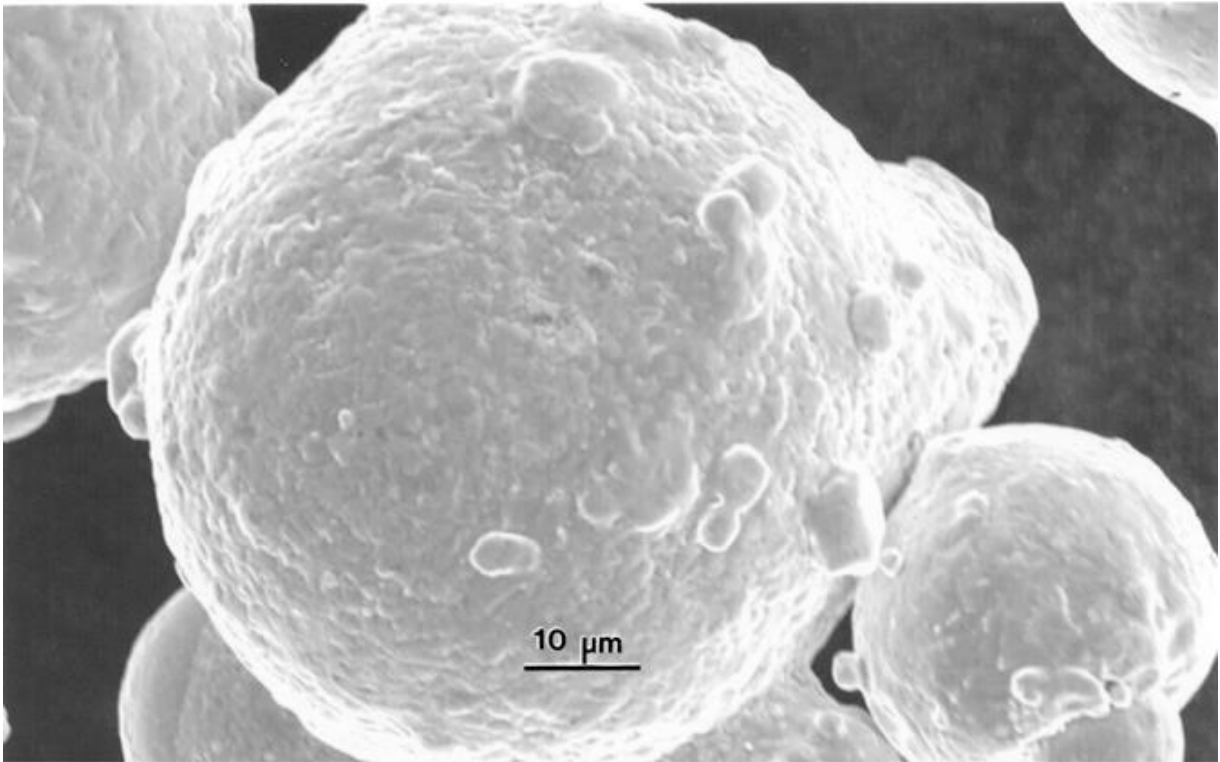


Figure 2.1.1 Co-29Cr-6Mo-0.22C powder

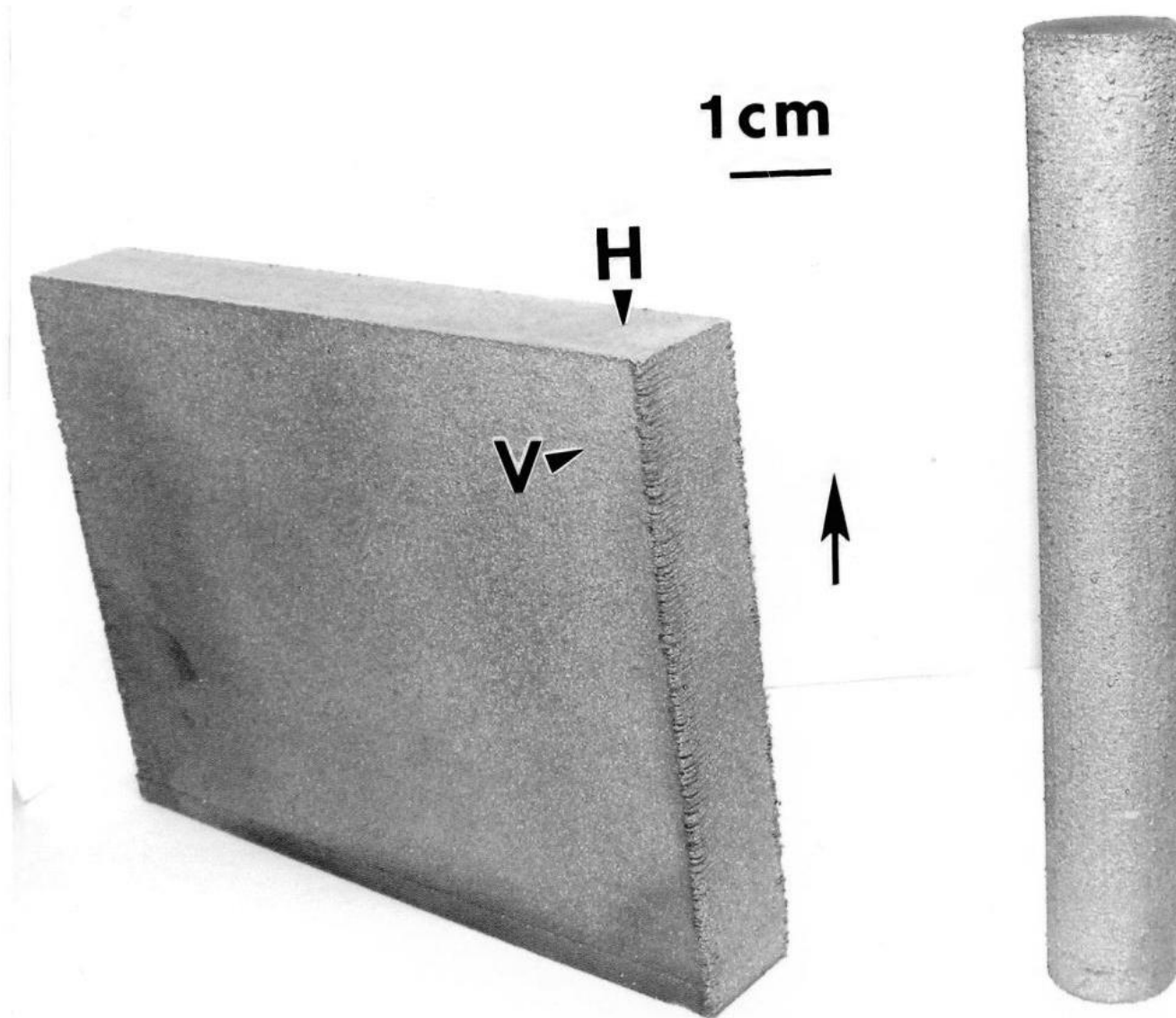


Figure 2.1.2 Example of simple geometry components manufactured by EBM, arrow shows build direction

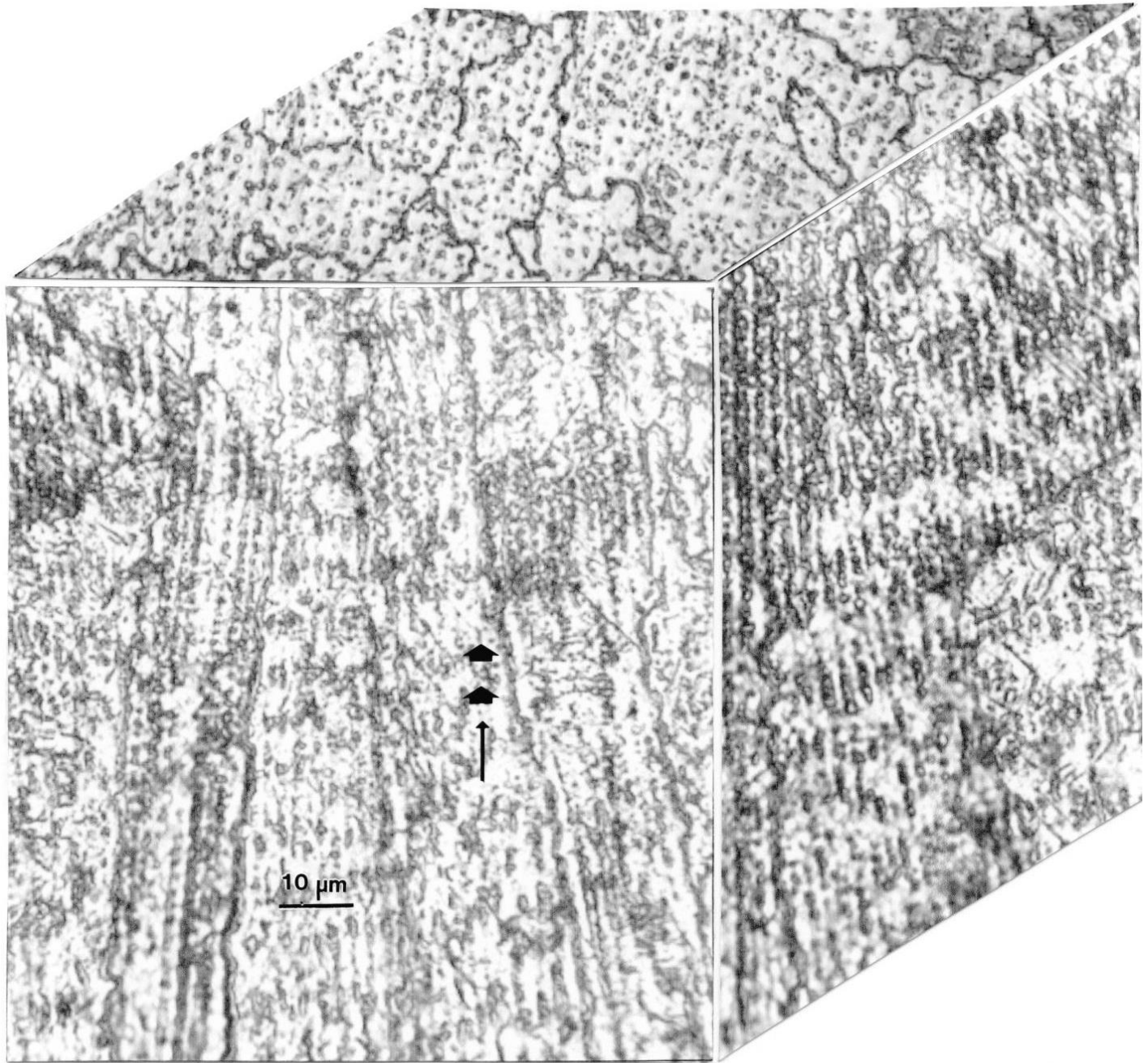


Figure 2.1.3 3D Micrograph showing carbide columns of Co-base superalloy by EBM, arrow shows build direction

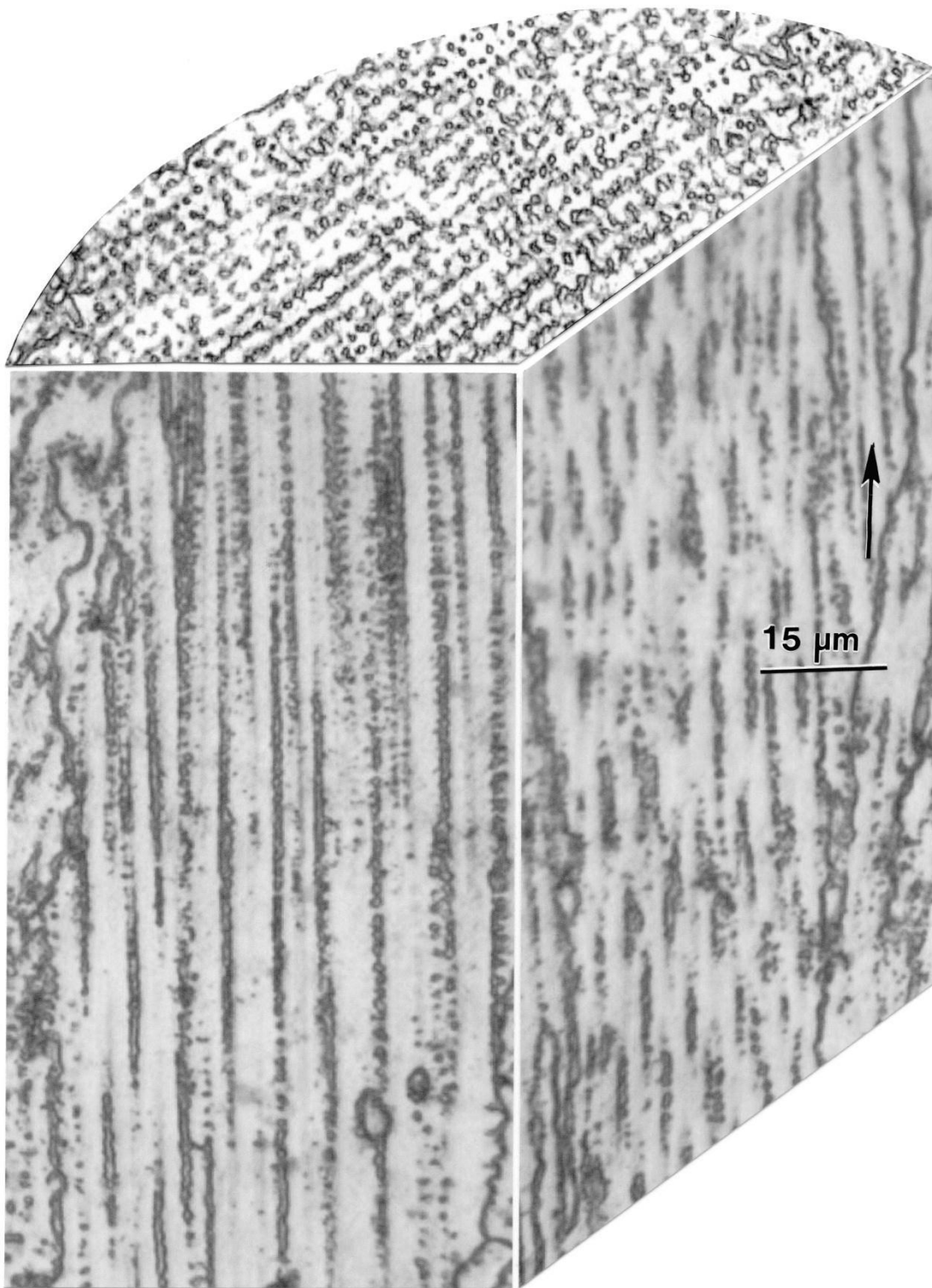


Figure 2.1.4 Magnified LOM 3D micrograph of columnar carbides in Co-Base superalloy by EBM

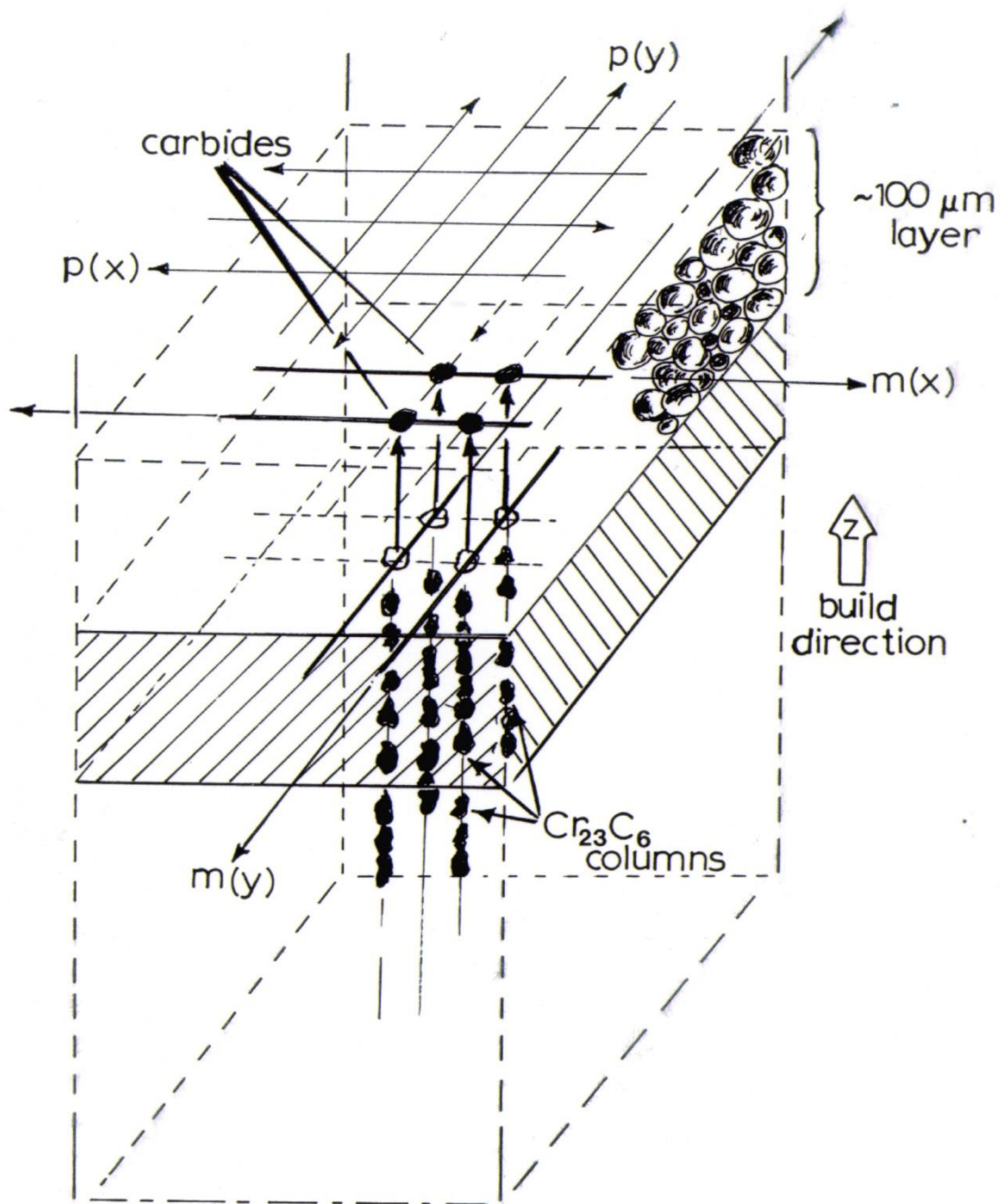


Figure 2.1.5 Schematic representation for the development of columnar carbides in Co-base superalloy manufactured by EBM

2.2 TRANSMISSION ELECTRON MICROSCOPY

As mentioned in section 2.1 the precipitate columns are discontinuous precipitate columns, these precipitates were identified to be Cr_{23}C_6 carbides. Figure 2.2.1 shows a 3D TEM image showing the cubic morphology of the Cr_{23}C_6 precipitates, these precipitates form from the 0.2% carbon in the fcc CoCr matrix within the melt pool. The TEM image also shows how the precipitates are discontinuous and reminiscent of the beam diameter. It also confirms what was seen with optical microscopy, the spacing of the precipitate columns was indeed $\sim 2\text{ }\mu\text{m}$. Note figure 2.2.1 is a compilation of many images that is why there is the square outlines that can be seen in the image. Figure 2.2.2 is a magnified 3D view of figure 2.2.1 which more clearly shows the cubic precipitates, the arrow in both images shows the build direction. Figure 2.2.2 shows that the Cr_{23}C_6 particles are spaced from 100 to 200 nm; this is seen in the columns or in the vertical direction of the 3D TEM image. The horizontal and vertical plane in this figure shows contrast fringes indicating linear stacking-fault features along with dense dislocation arrangements intermingled in the Cr_{23}C_6 precipitates. Figure 2.2.3 is magnified views of the Cr_{23}C_6 carbides which compose the columnar structure, image a) shows the carbide particles as well as stacking faults, b) is an isolated carbide and c) and d) show the cubic geometries of some of the particles. Figure 2.2.4 is images in the horizontal plane for comparison purposed, image a is an optical image showing the carbide particles, b) and c) are low and high magnification, respectively, TEM images showing the carbide particles and the SAED insert in c) shows the (100) plane orientation.[4]

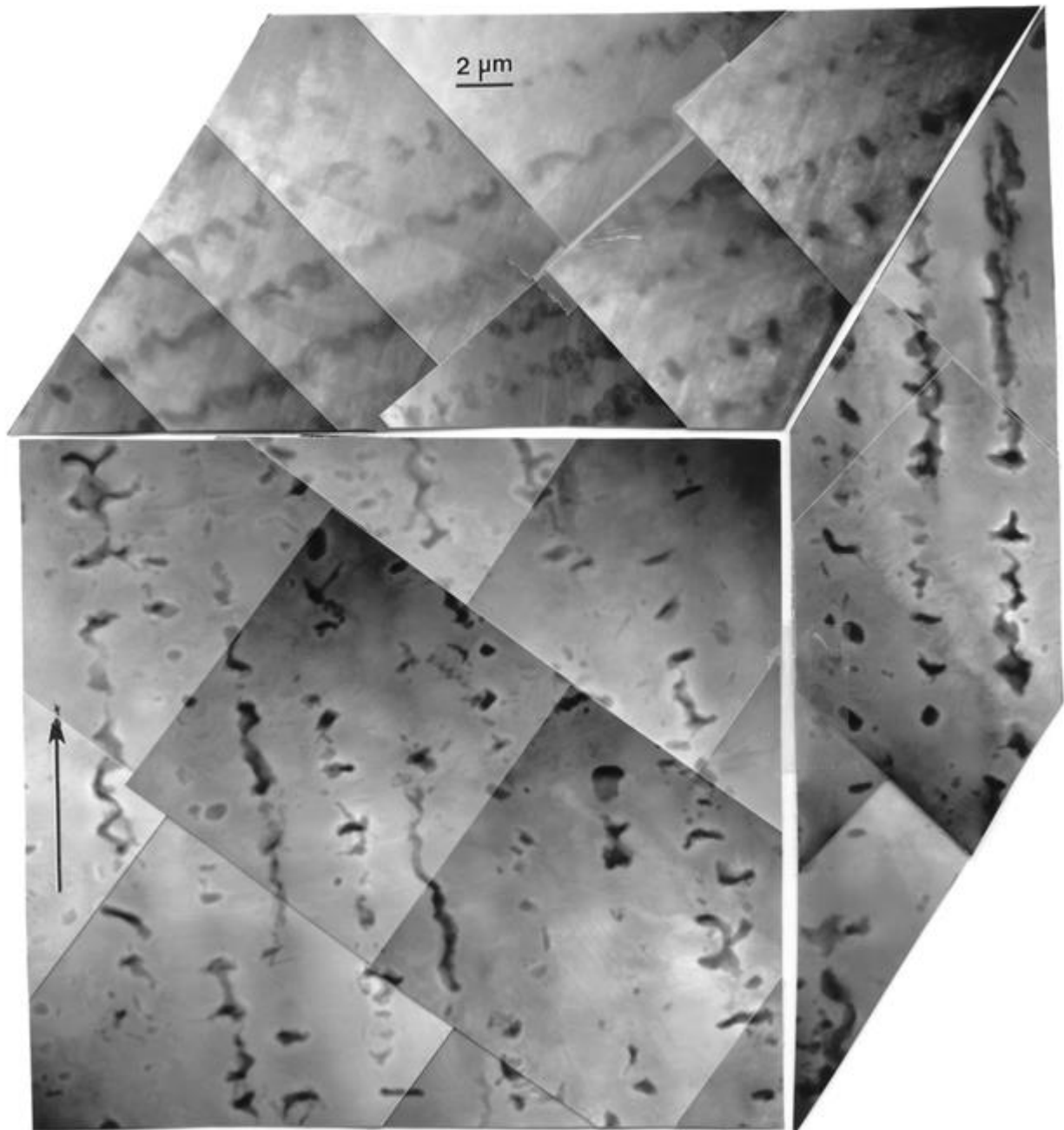


Figure 2.2.1 3D TEM image showing columns formed by Cr_{23}C_6 carbides

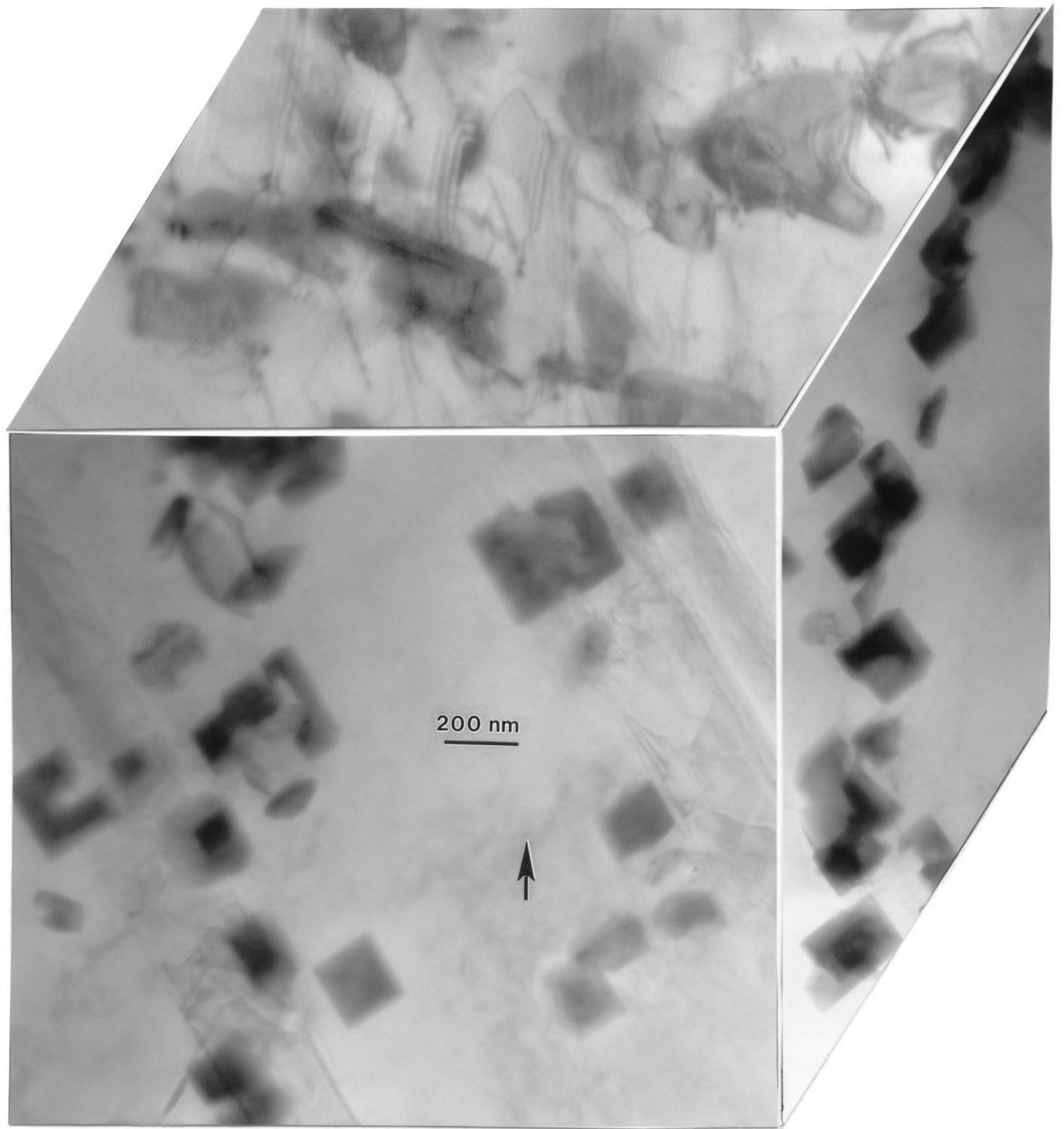


Figure 2.2.2 Magnified 3D TEM image showing the cubic structure of the Cr_{23}C_6 carbides

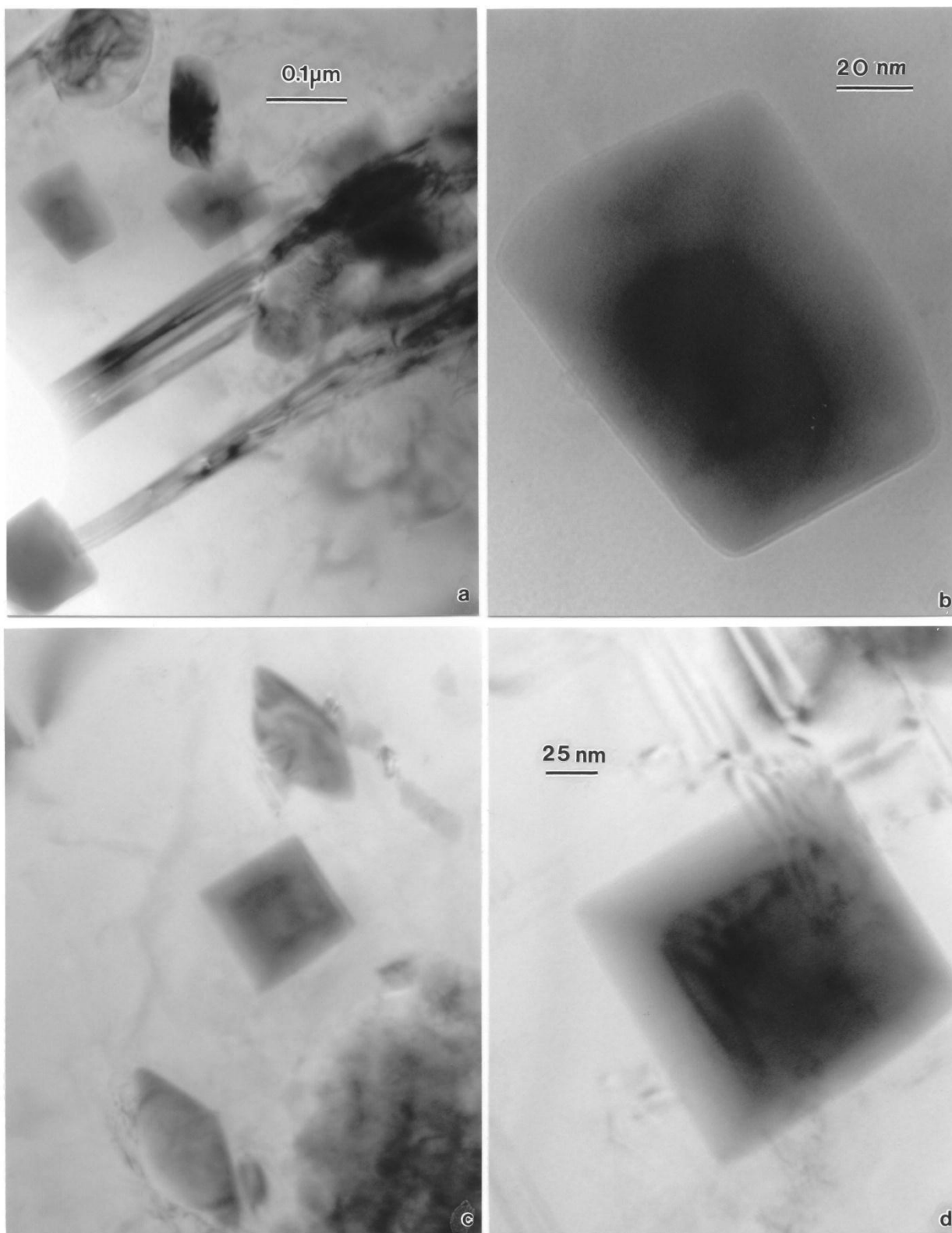


Figure 2.2.3 a) Cr_{23}C_6 carbides and stacking faults b) isolated carbide c) and d) show cubic geometries of the Cr_{23}C_6 carbides

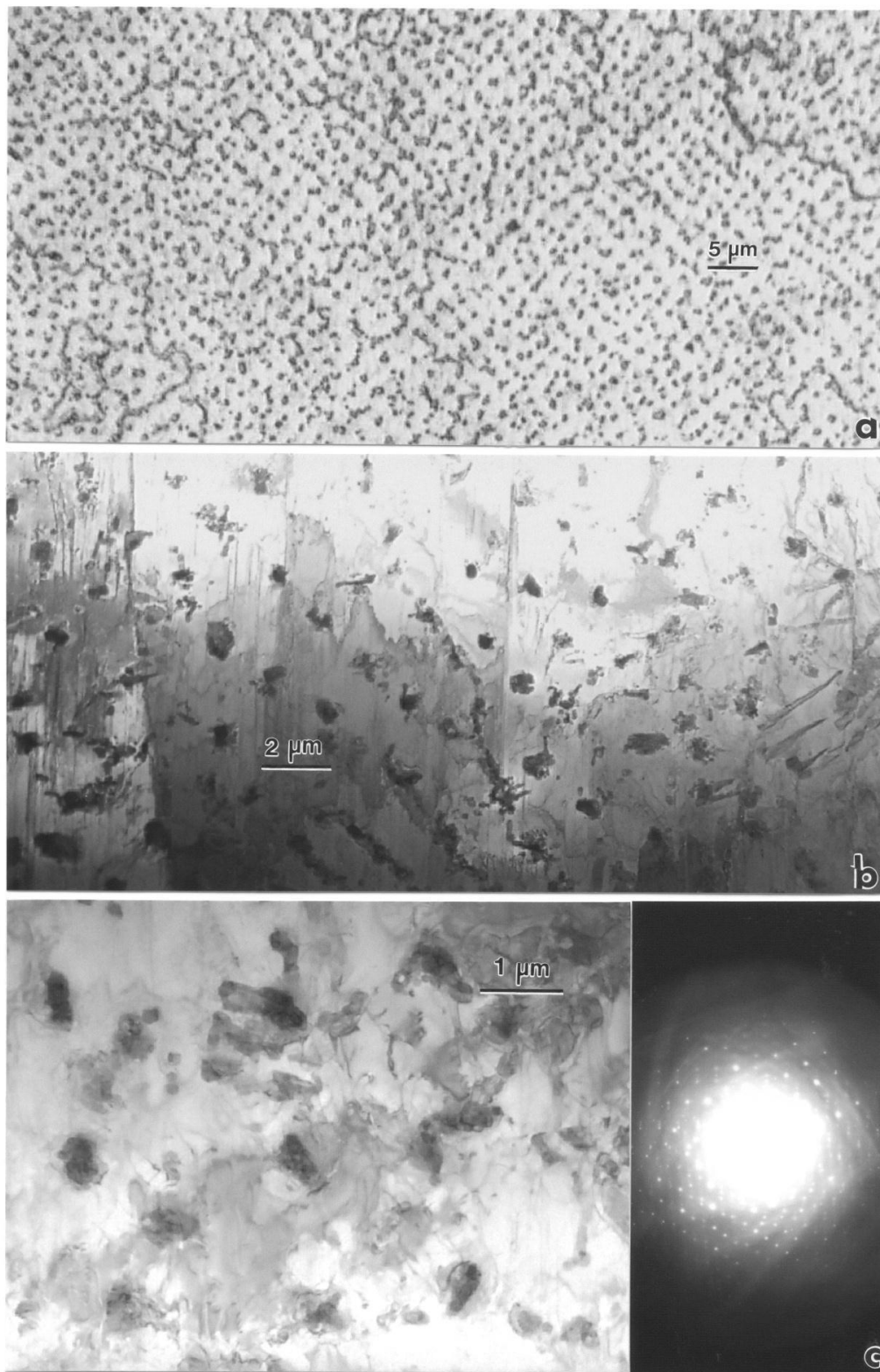


Figure 2.2.4 a) Horizontal micrograph showing Cr_{23}C_6 carbides as seen by light optical microscopy b) horizontal low mag view of carbides c) horizontal high mag view of carbides with SAED diffraction insert

Chapter 3

Copper Components Fabricated by EBM

3.1 OPTICAL MICROSCOPY

Like the Co-Cr the copper components which were fabricated by EBM contained directional microstructure that is also similar to the one seen in MnSb. The copper samples were etched with using a solution of 100 mL water, 8 mL sulfuric acid, 4 mL sodium chloride, and 2 g of potassium perchlorate. The components were manufactured using an atomized copper powder with a nominal purity of 99.8% copper. The copper powder was analyzed by light microscopy by mounting it in an epoxy, ground it, polished it and etched using the solution mentioned earlier. The features of the etched powder can be seen in figure 3.1.1; this image shows the grains of the powders which had an average grain size of 6 μm . The copper powders were also analyzed by SEM to analyze the microstructures a bit more as well as to get a particle size average; this will be discussed more in detail in section 3.2. In figure 3.1.2 we see some meshes with varying densities that were manufactured using the copper powder; cylinders as well as blocks were also manufactured for this analysis.

Figure 3.1.3 is a 3D micrograph for a cylindrical component showing small, equiaxed cells in the horizontal direction, perpendicular to the build direction, and connected elongated structures in the vertical plane parallel to the build direction. The corresponding Vickers, HV, average measurements can be seen in the horizontal, $\sim\text{HV } 83$, and vertical $\sim\text{HV } 86$, planes on the image. If we compare the microstructure in figure 3.1.3 to the microstructures of the powder, figure 3.1.1, we can see that there is a significant size difference, the domains in the cylindrical component are considerably smaller than the equiaxed grain structure that was seen in the powders. While you can appreciate the columnar microstructure of the copper in figure 3.1.3 you can't really see what exactly is going on in the structure so figure 3.1.4 shows a magnified section of this figure which illustrates irregular etching features or etch pits portraying the cellular-like structure. [10]

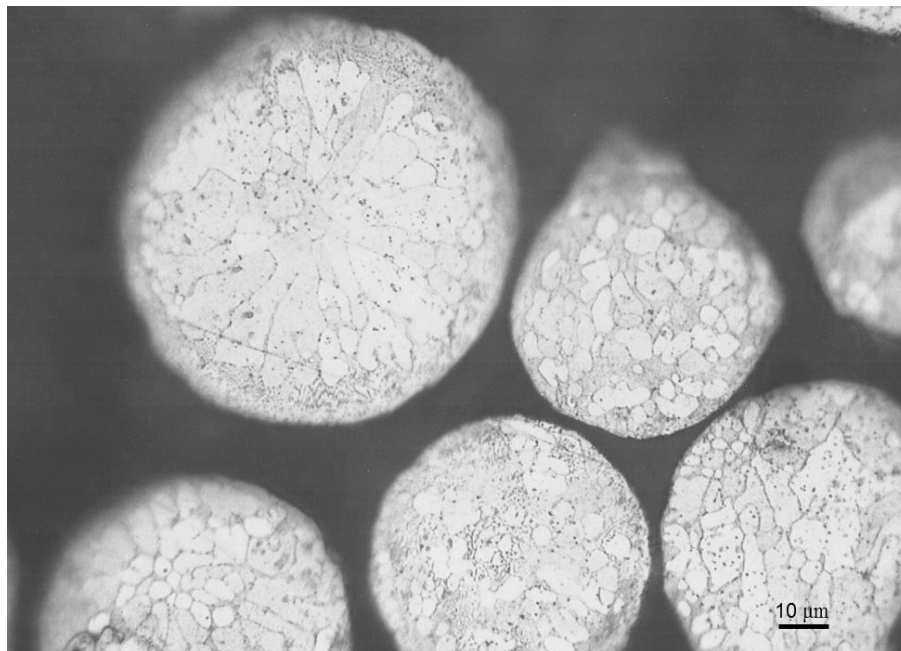


Figure 3.1.1 Cross section of copper etched powder showing equiaxed like grains

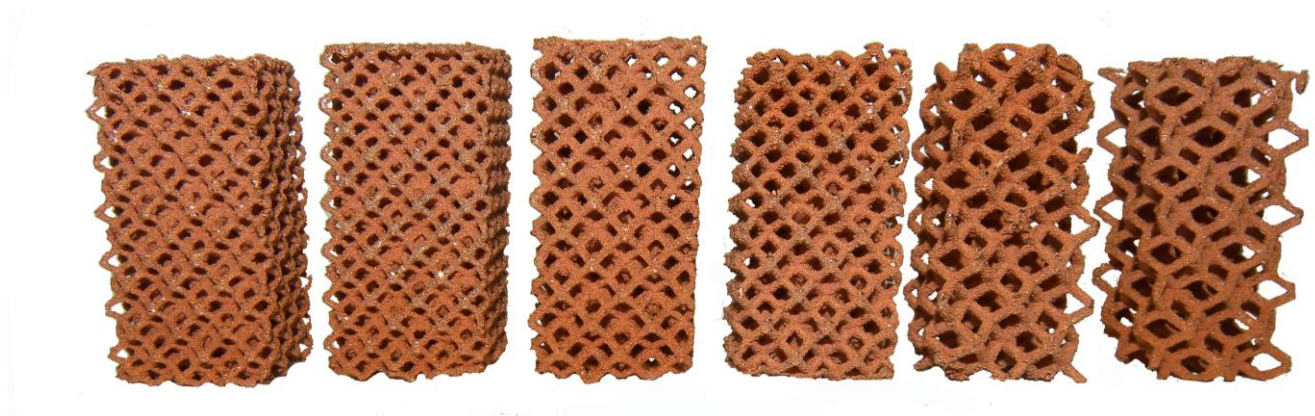


Figure 3.1.2 Example of some meshes manufactured with copper powder

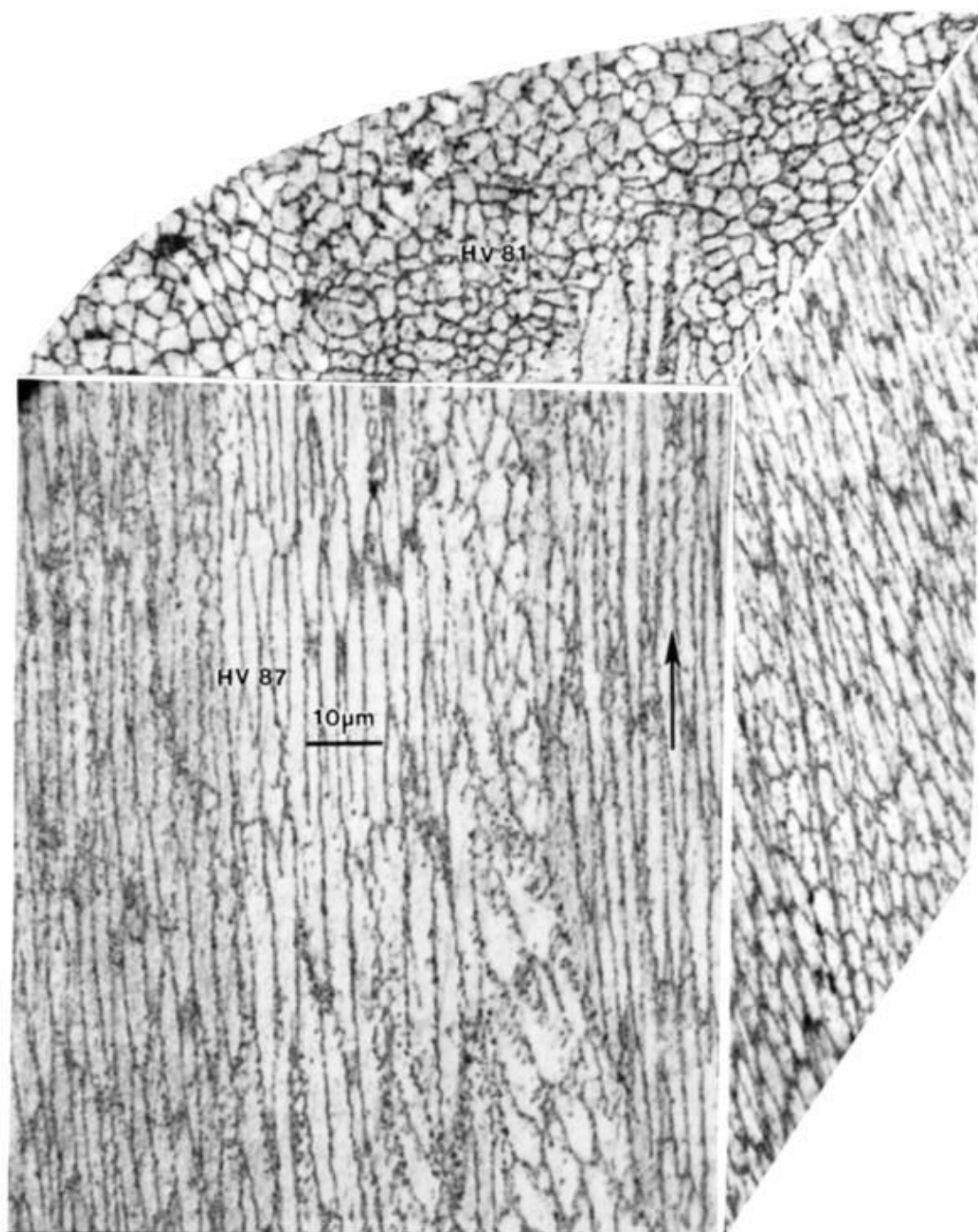


Figure 3.1.3 3D light optical micrograph showing columnar microstructures, arrow shows build direction

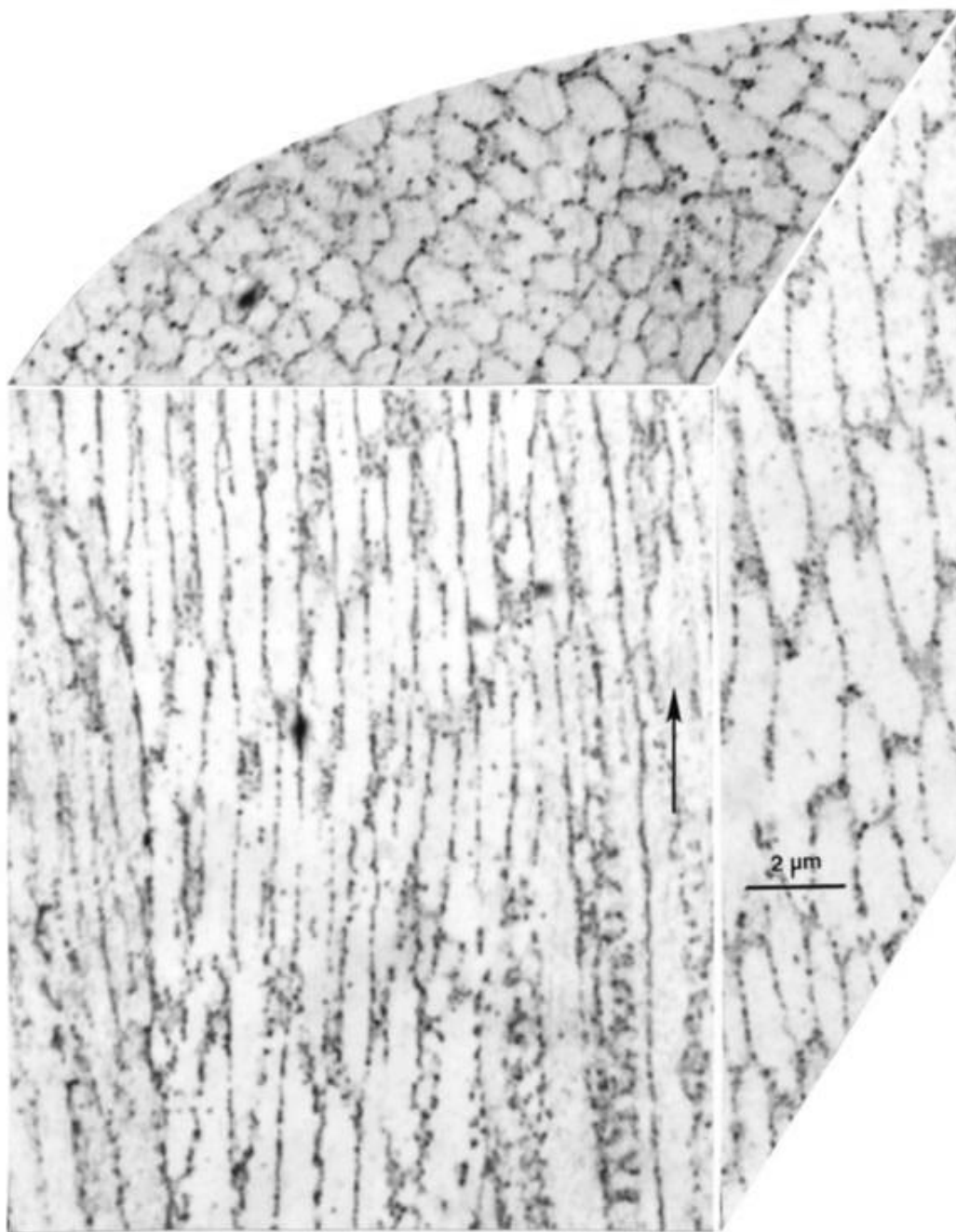


Figure 3.1.4 Magnified 3D LOM section of figure 3.1.3

3.2 SCANNING ELECTRON MICROSCOPY

Light optical microscopy showed us that the cellular-like structure was seen because of the etch pits that resulted from the etching process, the next step in understanding the microstructure of the copper was to place our etched samples into the SEM. The powders that were used for the manufacturing process were observed in the SEM where we saw that the particle size distribution consisted primarily of large particles which ranged from about 40 to 100 μm with an average particle size of 65 μm ; figure 3.2.1 shows that these larger particles also contain smaller particles attached to them. As mentioned in section 3.1 the cellular-like structure was resulted because of the etched pits which emulate the structure of the Cu_2O precipitates, the structure details occur because of a localized reaction that occurs with the etchant. The localized reaction that occurred with the etchant was also seen in the powders, this was not clear at first as seen in figure 3.2.2a but when the section was magnified the etch pits were clearly visible, figure 3.2.2b. The precipitates were shown to be cubic precipitates, the etchant that was used etched away the copper oxides and this can be seen more clearly by the SEM images in figures 3.2.3a and 3.2.3b. The Cu_2O precipitates are formed from oxygen that is absorbed during the copper atomization in purified argon as a consequence of the affinity for oxygen of the copper powder particles; even under the most stringent inert environments the copper particle will include some oxygen. The optical micrograph of the copper powder as seen in figure 3.1.3 shows that the precipitates are located in the grain boundaries and can either solutionize or reorganize in the melt pool structures which in turn create the columnar precipitate structure. When the copper powder had oxygen less than one weight percent the components that were manufactured contained directional Cu_2O precipitate columns which as mentioned earlier are similar to the ones seen in Co-Cr.

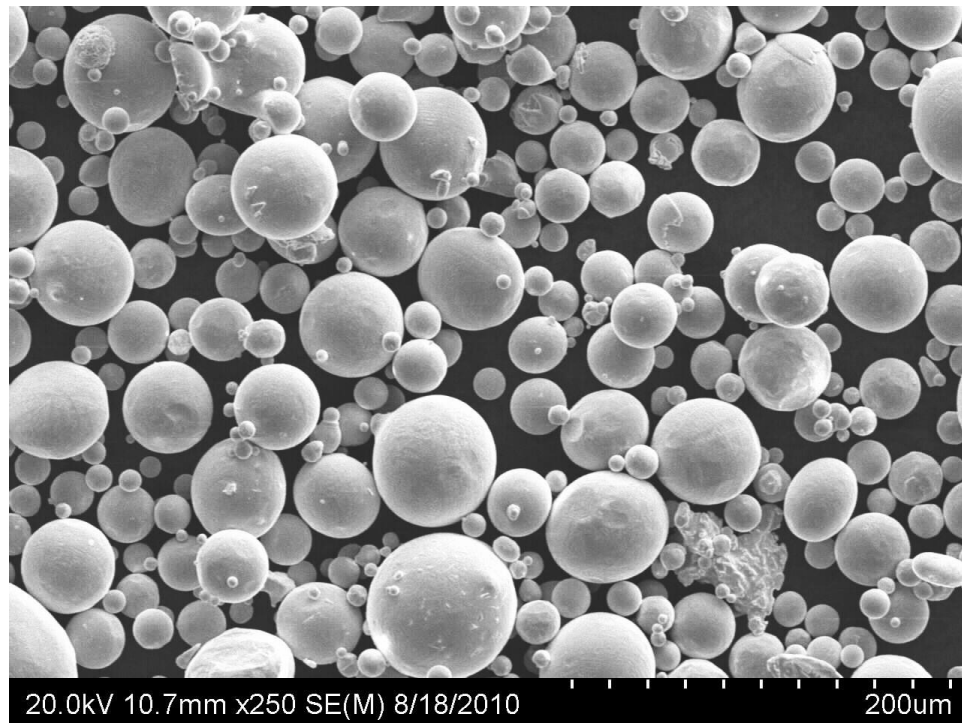
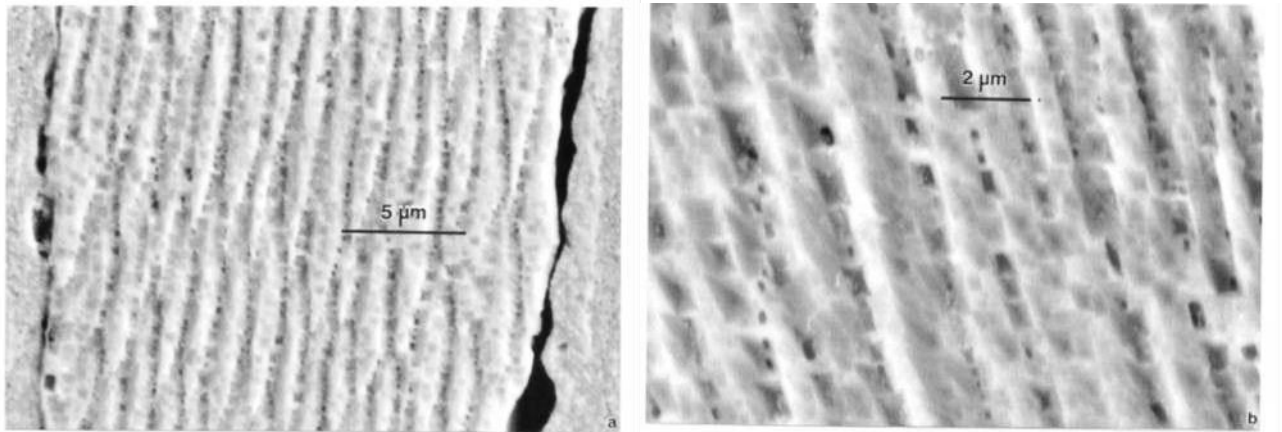
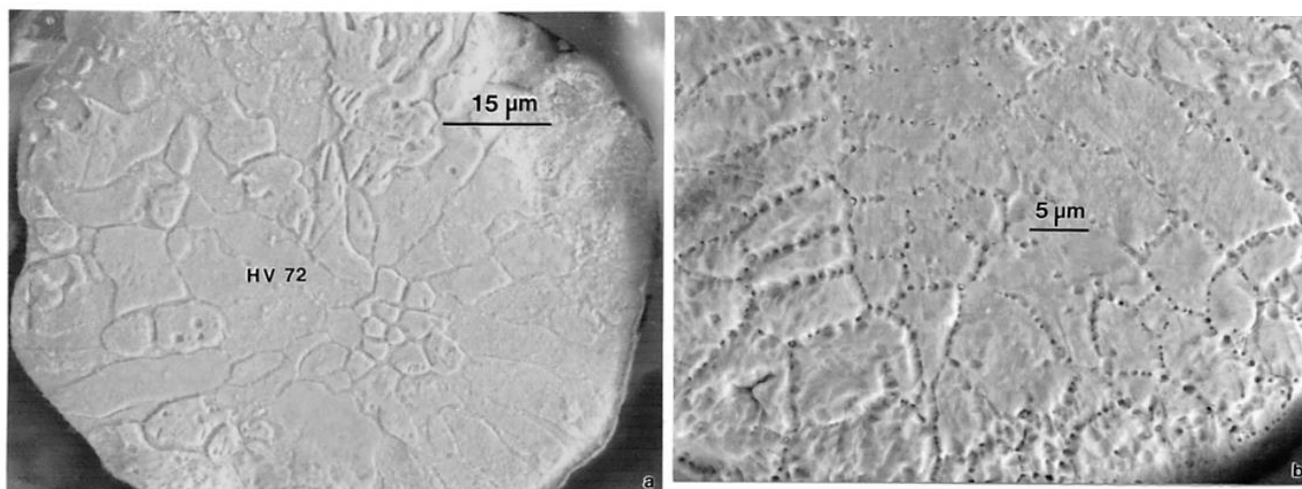


Figure 3.2.1 Copper powder distribution with an average size of 65 μm



Figures 3.2.2 a) Cellular-like structure resultant from etch pits b) Magnified view of a section from image a).



Figures 3.2.3 SEM images from copper powder a) shows the grains in the etched powder b) magnified image of a) showing the etched out precipitates in the grain boundaries

3.3 TRANSMISSION ELECTRON MICROSCOPY

Different samples were cut and thinned down to be prepared for viewing in the TEM, once the samples were down to the right thickness and made into 3 mm discs they were electro-polished using a solution which consisted of 825 mL water, 375 mL ethanol, 300 mL phosphoric acid, 75 mL propanol, and 2.5 g urea. The Tenupol-3 dual jet electro polishing unit was operated at 8 volts with the solution at 15°C. It is important to note that the H_2SO_4 used for the etching of the samples for optical microscopy viewing is more aggressive than the phosphoric acid etchant that was used for TEM analysis. The etch pit features that were seen by SEM in figures 3.2.2a and 3.2.2b were more prominent in the TEM as can be seen in figure 3.3.1. This figure is from a horizontal section of a sample and shows a unique precipitate/dislocation structure, with non-coherent Cu_2O precipitates attached to dislocations which form the spatial arrays which are selectively etched forming the etched pits seen in figures 3.2.2. Figure 3.3.2 shows a magnified section of figure 3.3.1 showing the precipitates tangled in dislocations as well as the vacancy dislocation loop which can be seen by the arrow in the image. Note that there are some selectively etched out precipitates, white areas, which exhibit cubic geometries seen in figures 3.2.2. The etching suggests that the precipitates have a common orientation; this is also suggested by examining the selected area electron diffraction pattern insert in figure 3.3.2 of the precipitate morphologies in the

(110) grain surface orientation. Figure 3.3.3 is from the vertical plane of the manufactured copper components, this figure illustrates the elongated cell-like precipitate-dislocation microstructural architecture; white parts also show etched out precipitates. Figure 3.3.4 is a 3D TEM image composition which shows how the precipitate-dislocations array on the horizontal and vertical planes look.

As seen in figures 3.3.1 and 3.3.2 the precipitates are tangled in dislocation arrays; the dislocations found in the samples could have formed due to the thermal stresses that take place during the precipitation process and the cooling in the melt pools. Figure 3.3.5 is a modified schematic of figure 2.1.5 in order to compensate for the formation of the dislocations; the melt pool dimensions during the fabrication of the copper were $\sim 2\text{-}3\text{ }\mu\text{m}$. The microstructural architecture seen in many of the figures appear to be a result of precipitation in the pre-heat and melt scans, the rearrangement of the precipitates during the melt scan or both. The spatial precipitate-dislocation arrays that were observed in the horizontal plane, figures 3.3.1 and 3.3.2, appear to be related to and controlled by the pre-heat and melt scan parameters. The melt scan geometry, as seen in figure 3.3.5 (x,y) directions, create thermo-kinetic zones whose spatial features are dependent on the scan dimensions or spacing of the EBM. [18]

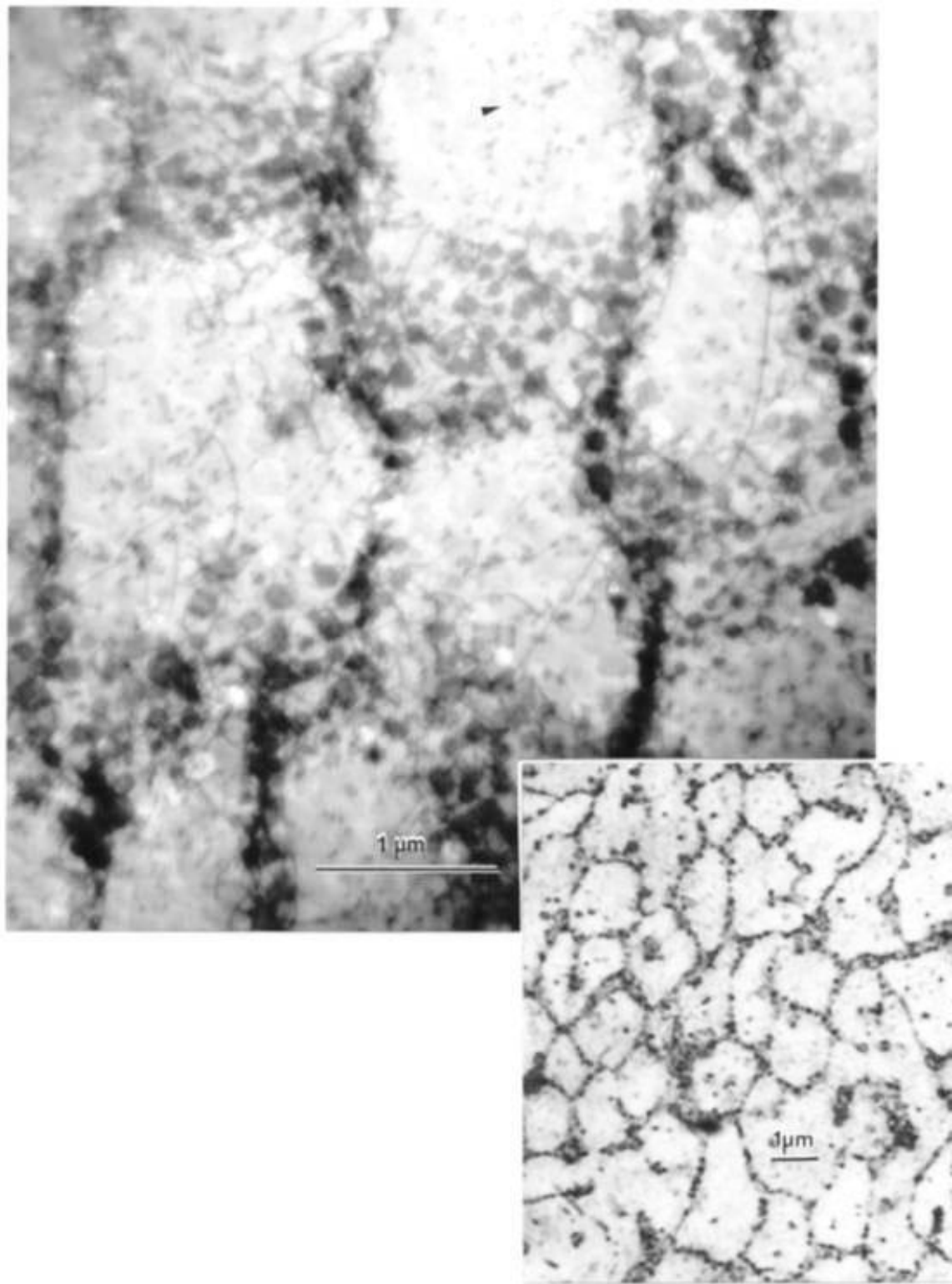


Figure 3.3.1 Horizontal plane bright field TEM image showing precipitate-dislocation arrays

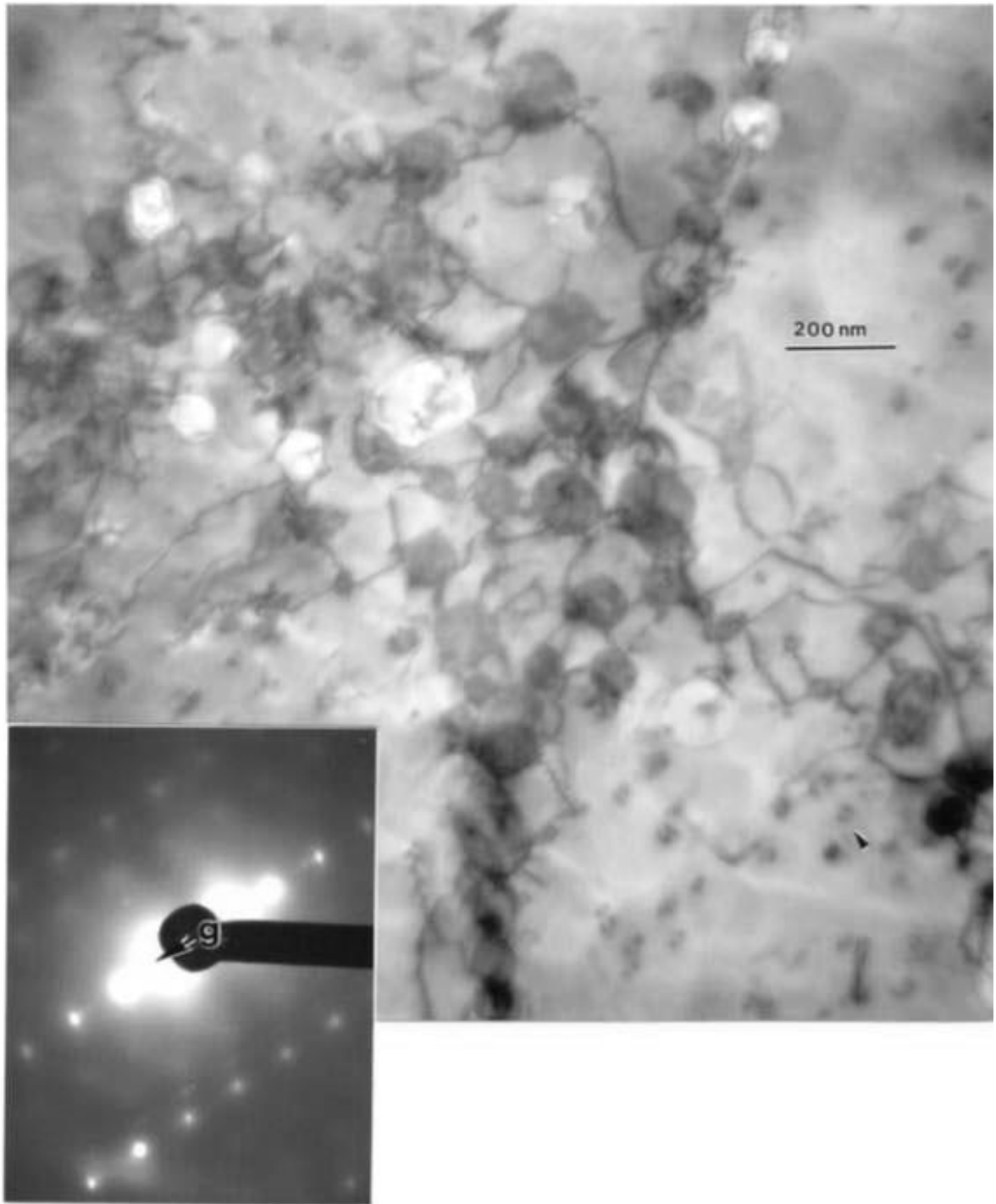


Figure 3.3.2 Magnified view for the horizontal plane showing precipitate-dislocation arrays with corresponding SAED insert [110]

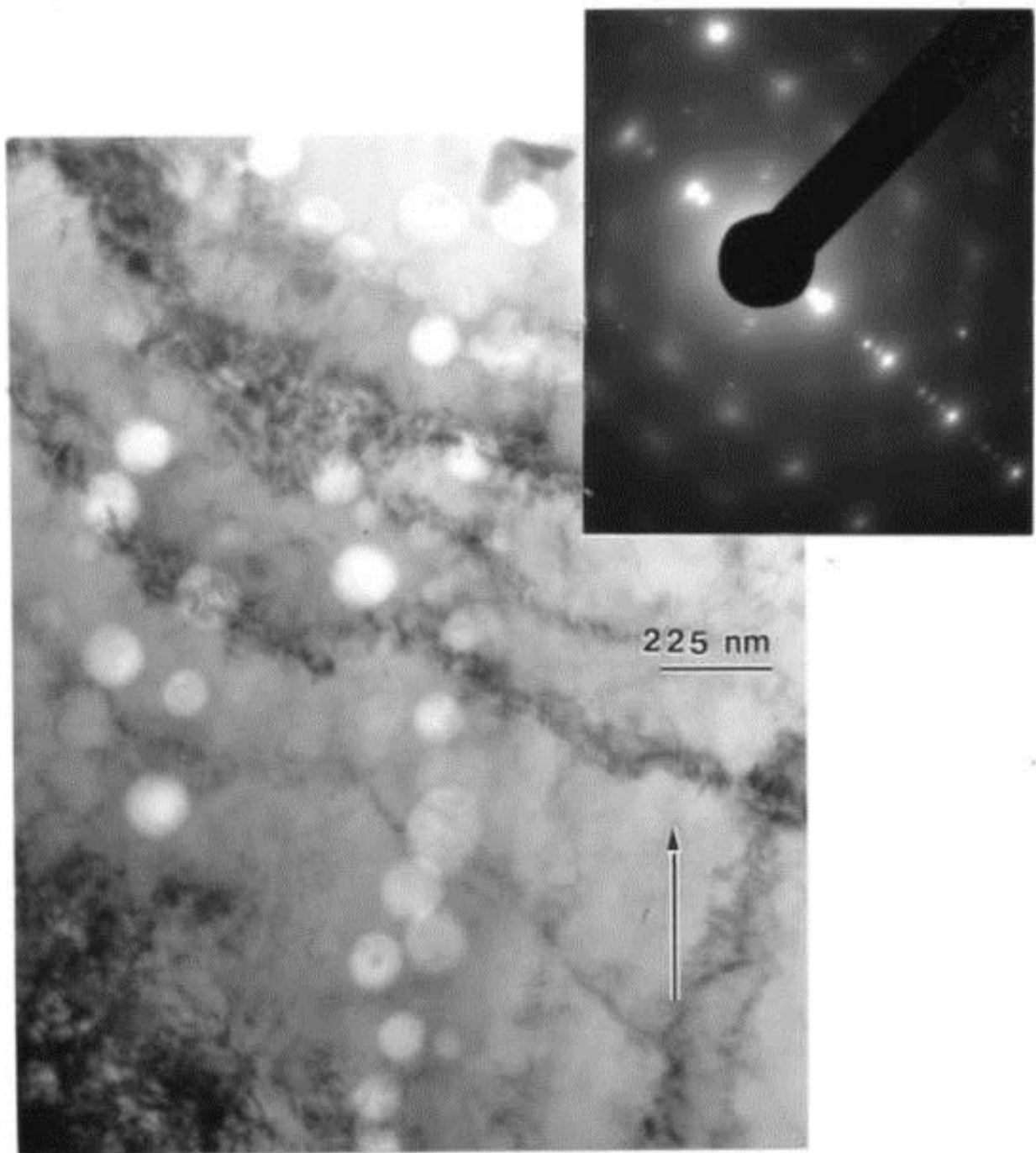


Figure 3.3.3 Vertical plane bright field TEM image showing precipitate-dislocations arrays with selective precipitate etching and corresponding SAED diffraction

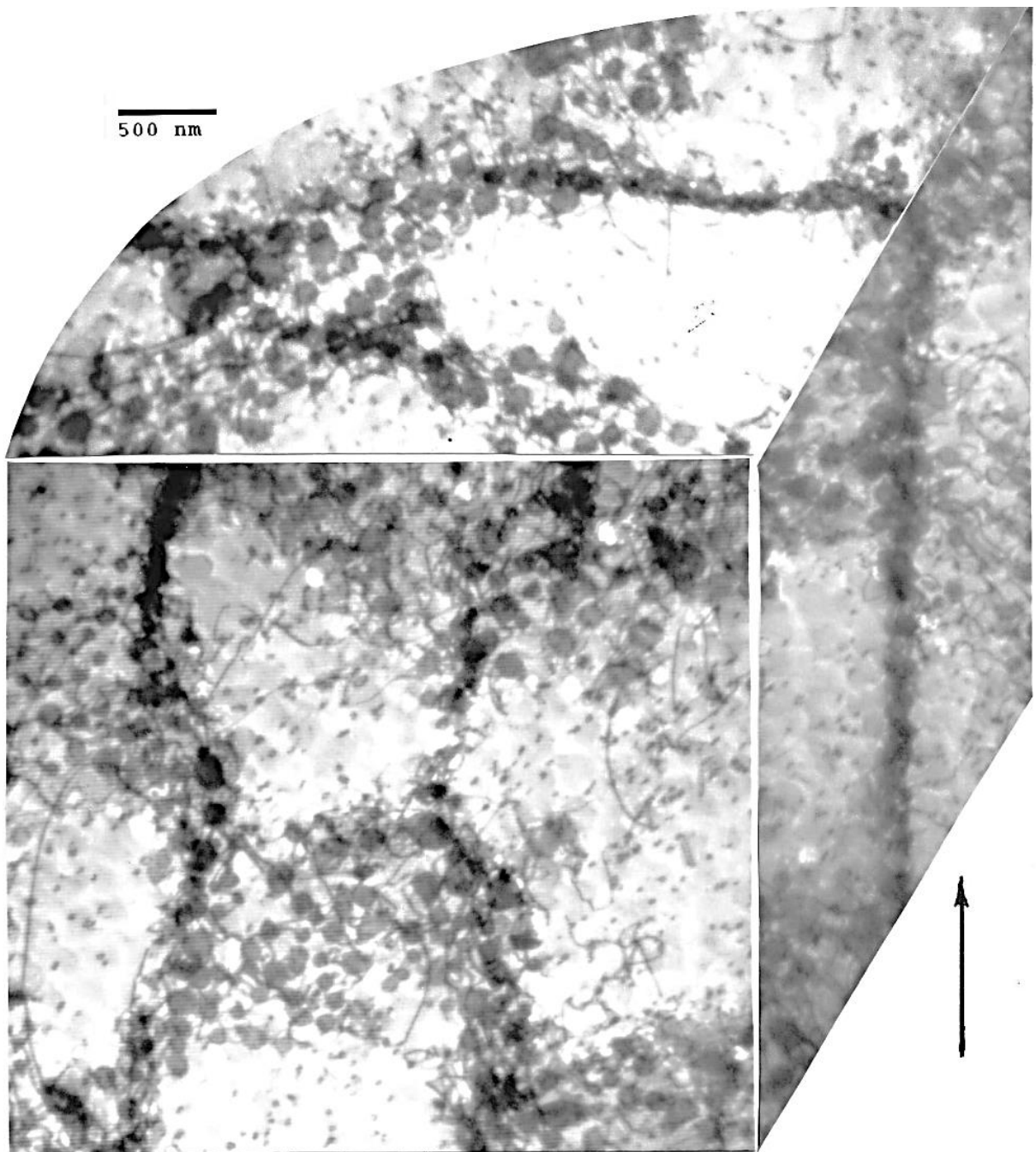


Figure 3.3.4 3D TEM image showing Cu₂O precipitate-dislocation arrays in both horizontal and vertical plane, arrow is build direction

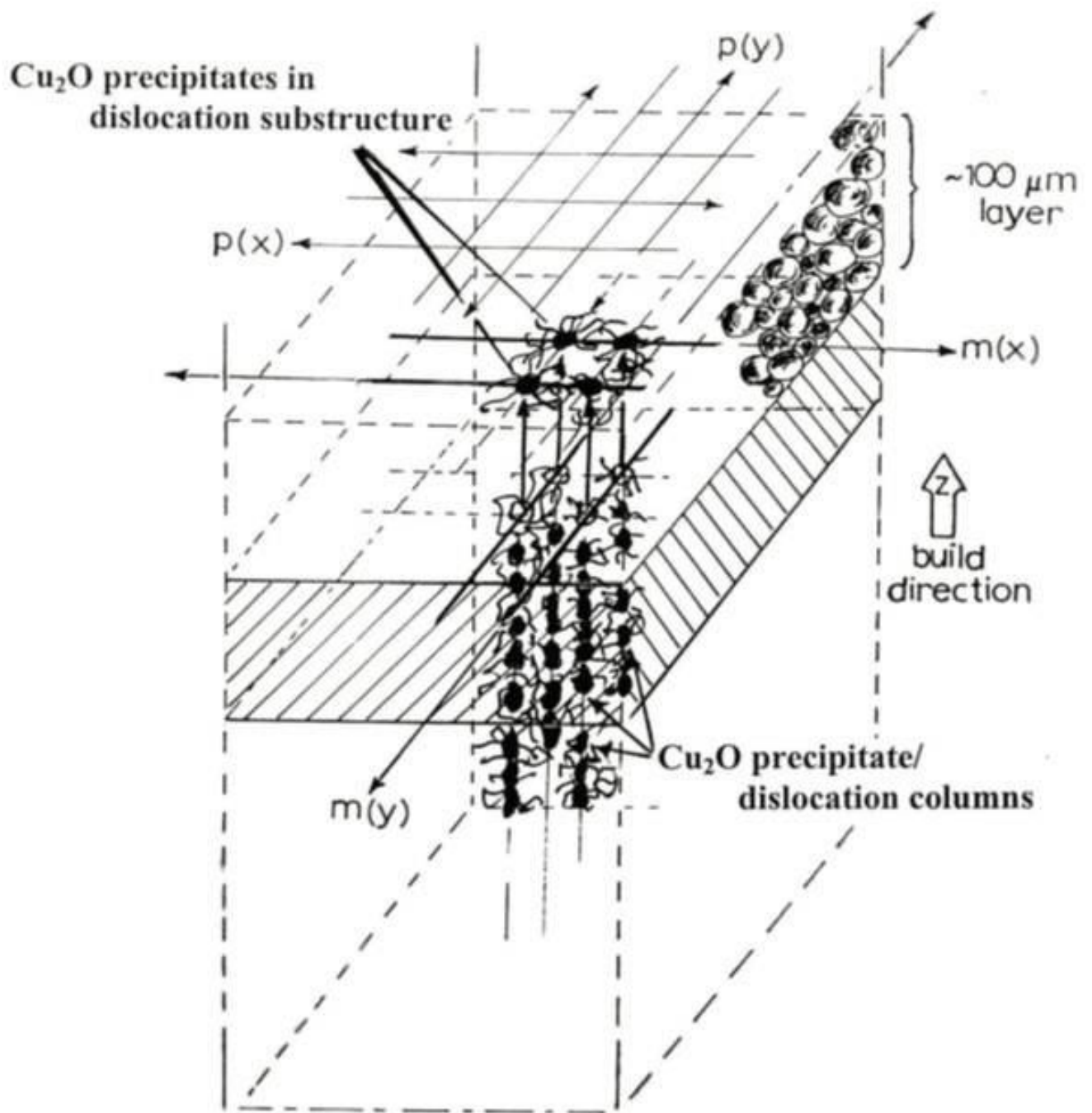


Figure 3.3.5 EBM geometry scan illustrating the formation of precipitate-dislocation arrays. Preheat scans, $p(x)$ $p(y)$ and melt scans $m(x)$ $m(y)$.

Chapter 4

Manufacturing of Inconel 625 by EBM and SLM

4.1 INCONEL 625 EBM OPTICAL MICROSCOPY

Inconel 625 was one of the first materials that we manufactured for us and analyzed using both an EBM and SLM, both systems showed similar microstructures with a few key differences. Figure 4.1.1 shows the Inconel 625, Ni-21Cr-9Mo-4Nb, powders which were analyzed using SEM; the figure shows the dendritic structure of the powder. The powder was also mounted, polished, and electro-etched using a solution of 70 mL phosphoric acid and 30 mL of water at 5 volts for 5 to 20 seconds. Figure 4.1.2 is a light microscopy image showing the Inconel powder after it was polished and etched and it shows the same dendritic structure that was seen using an SEM; the Inconel 625 precursor powder does not exhibit any precipitation features like the copper powder did. The first samples that were analyzed were manufactured using the EBM, figure 4.1.3 shows a 3D light microscopy image of a cylinder component which was etched using the same solution for the powder. The figure shows the columnar architecture which was seen in the Co-Cr components and in the copper components. In the case of the Inconel 625, we found that the components contained γ'' -Ni₃Nb precipitates which were coincident with the Ni-Cr fcc {111} planes. It is easier to see that the γ'' -Ni₃Nb precipitates are platelets in the vertical direction that it is to see them in the horizontal direction; this can be seen in figure 4.1.4 which is a high magnification light microscopy composition. The columnar grains which can be observed in figure 4.1.4 shows that the columnar grain length is $\geq 200\text{ }\mu\text{m}$ and that the equiaxed grain width can vary from a few microns to $>10\text{ }\mu\text{m}$. The columnar precipitate arrays are spaced ~ 2 to $3\text{ }\mu\text{m}$ or larger; these features, like mentioned earlier, are created by the EBM-beam scans.

Vickers microindentation hardness measurements were made on the powders and on the vertical and horizontal planes of the components. The powder showed an average value of HV 260 or 2.6 GPa, the horizontal plane showed an average value of HV 280 or 2.8 GPa, and the vertical plane showed an average measurement of HV 250 or 2.5 GPa. [11]

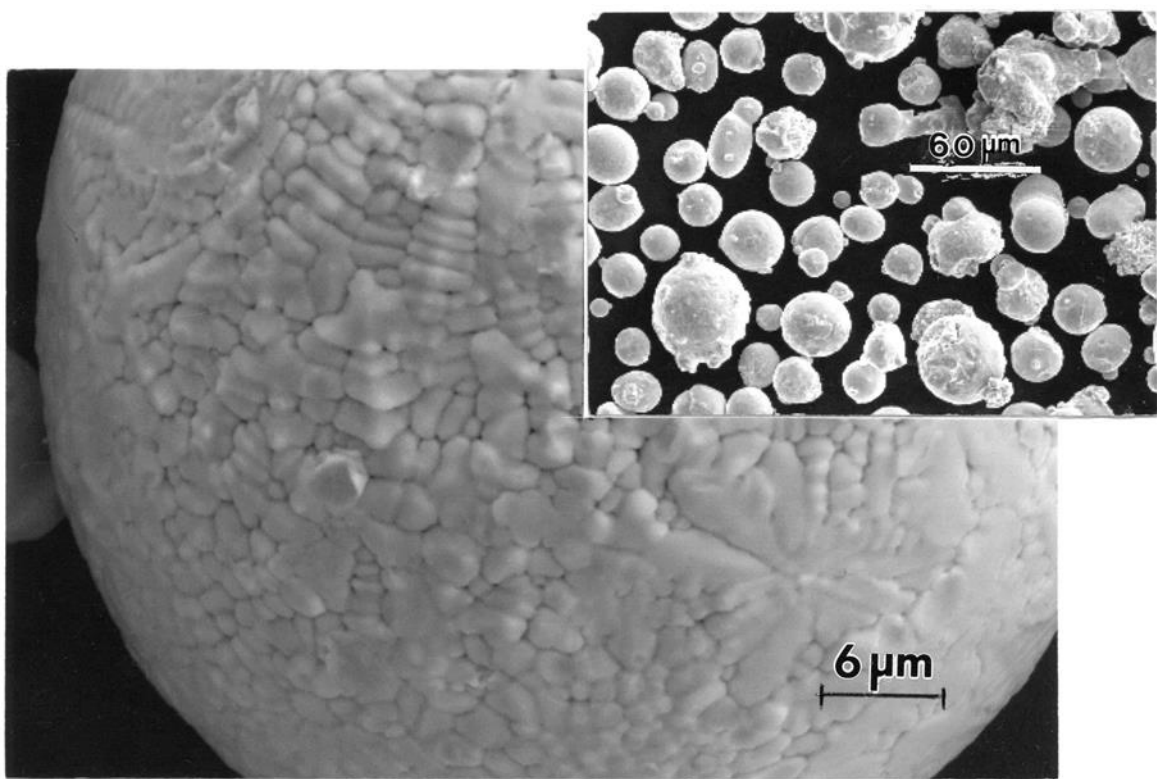


Figure 4.1.1 Inconel 625 powder as seen by SEM showing microdendritic structure

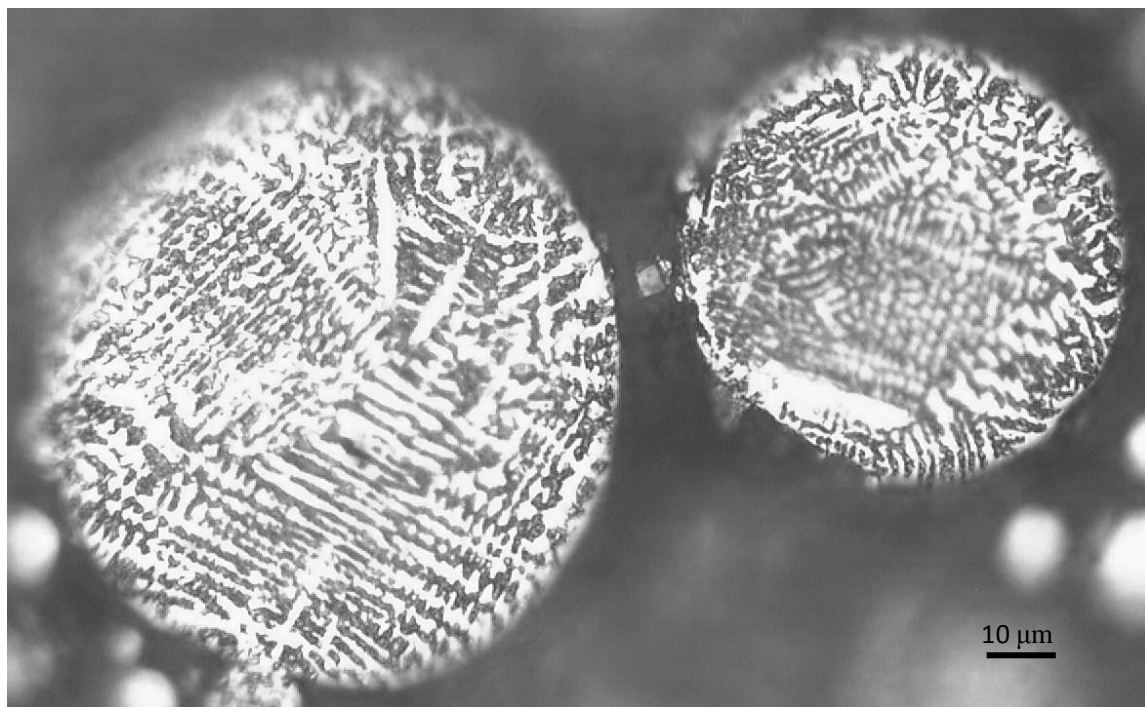


Figure 4.1.2 LOM cross section of etched Inconel 625 powders showing microdendritic structure

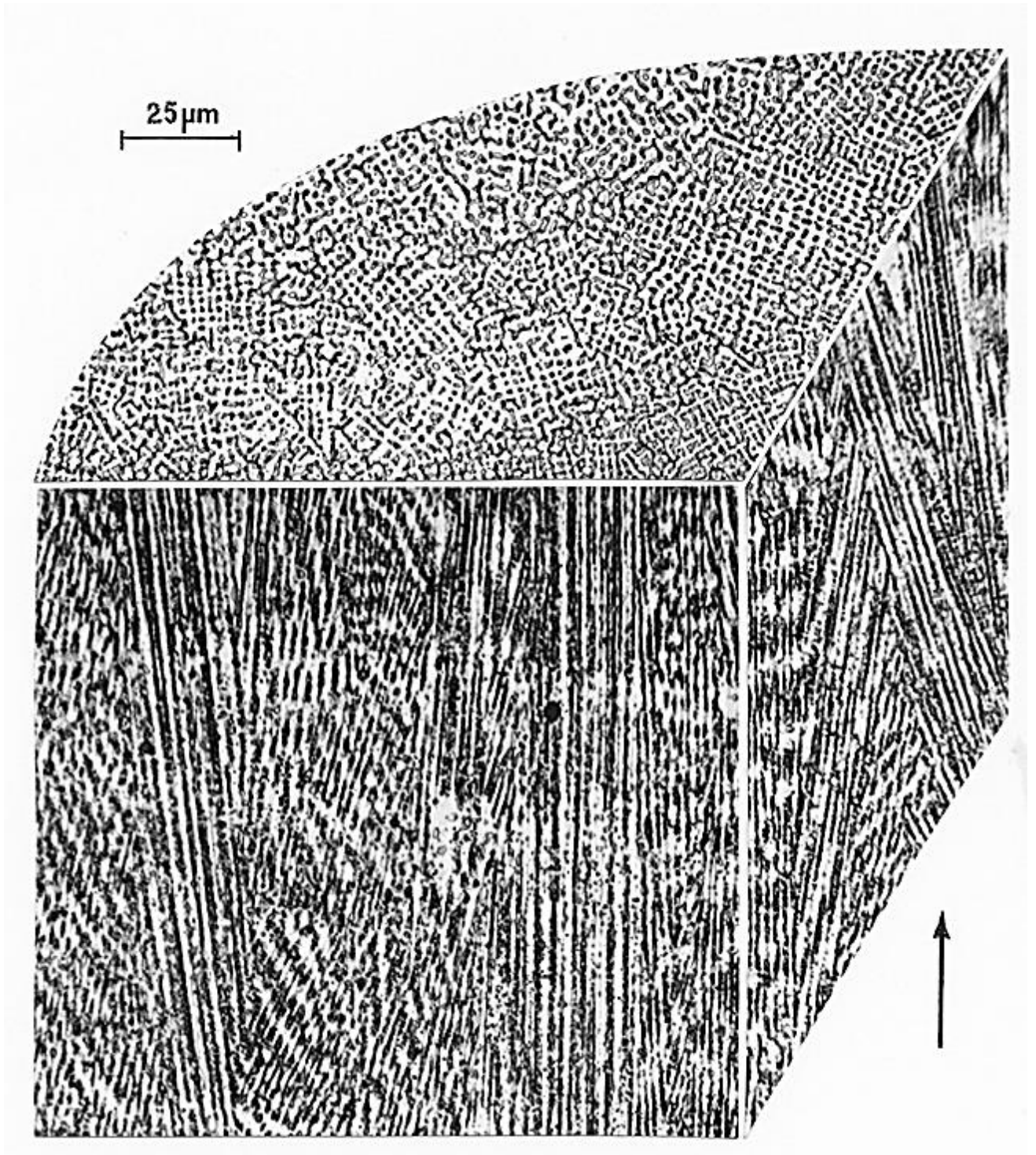


Figure 4.1.3 3D LOM image showing columnar microstructure, arrow shows build direction



Figure 4.1.4 LOM image composition showing columnar platelet precipitates

4.2 XRD AND TEM OF EBM MANUFACTURED COMPONENTS

X-ray spectroscopy (XRD) analysis was done for the powder as well as for the horizontal and vertical plane of the components manufactured by EBM. The powder showed a prominent (111) peak which is coincident with the solid-solution NiCr spectral indices, together these characterize the dendritic structure and the matrix; the XRD spectra for the powder can be observed in figure 4.2.1. XRD spectra for the sample seen in figure 4.1.4 can be observed in figure 4.2.2 which showed that the vertical plane is highly textured in [220] and is coincident with the [110] zone seen in figure 4.2.3; the horizontal plane for this sample was highly textured in [200]

TEM was also done to analyze the samples by electroetching them in a solution which consisted of 20% perchloric acid, 80% methanol at 13 volts with a temperature of $\sim 29^{\circ}\text{C}$. Figure 4.2.3 shows a 3D TEM image composition of the EBM fabricated Inconel 625, the trace directions shown in the image correspond to **a** $[1\bar{1}0]$, **b** $[1\bar{1}2]$, **c** $[1\bar{1}\bar{2}]$. The edge on views of the platelet precipitates indicates them to be lenticular, the greatest thickness is found at the center of the platelets. The platelet thickness was measured to be <50 nm in the thinnest section and up to ~ 100 nm in the thickest sections, the center of the platelets. Besides the platelets the image shows moderate densities of dislocations within the platelet precipitates. [11,17]

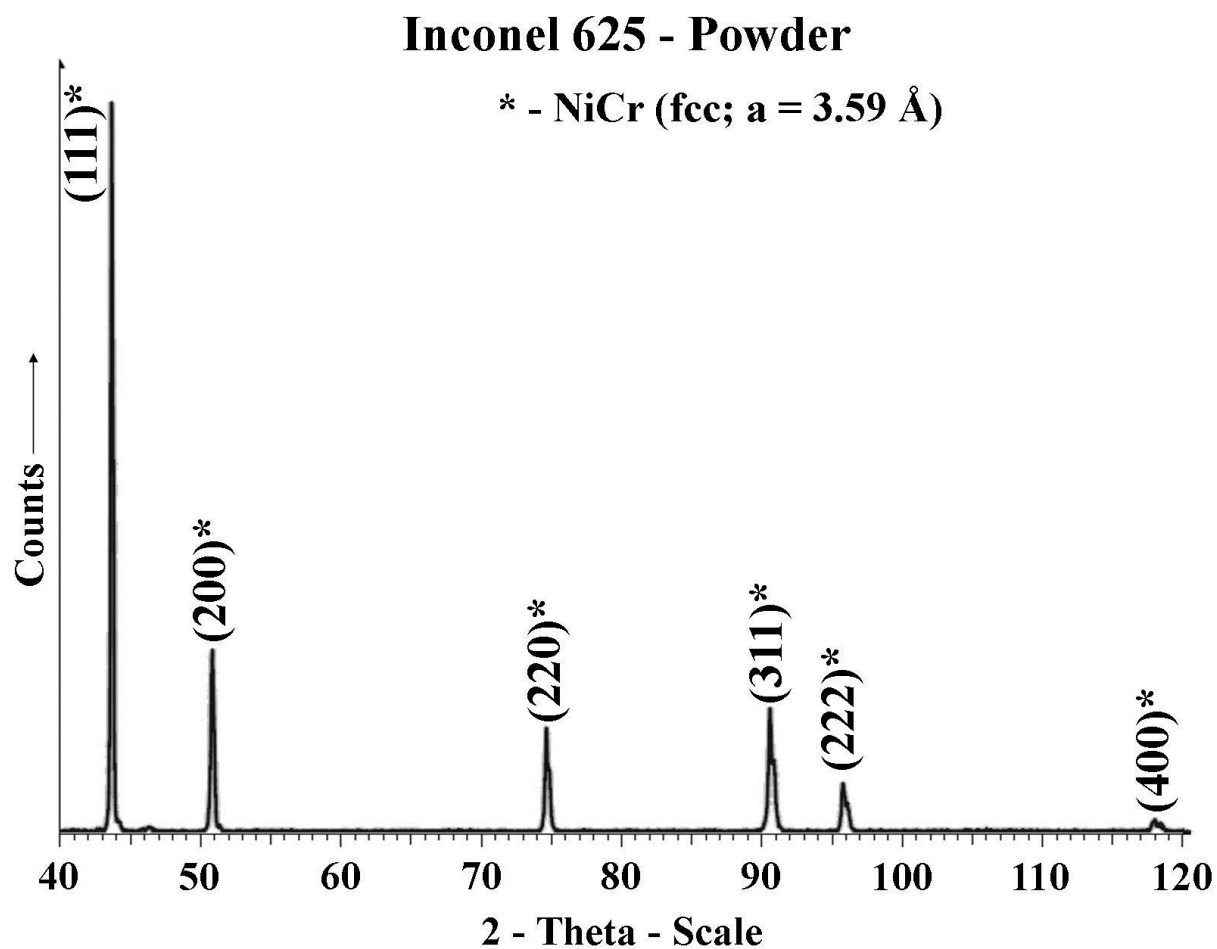
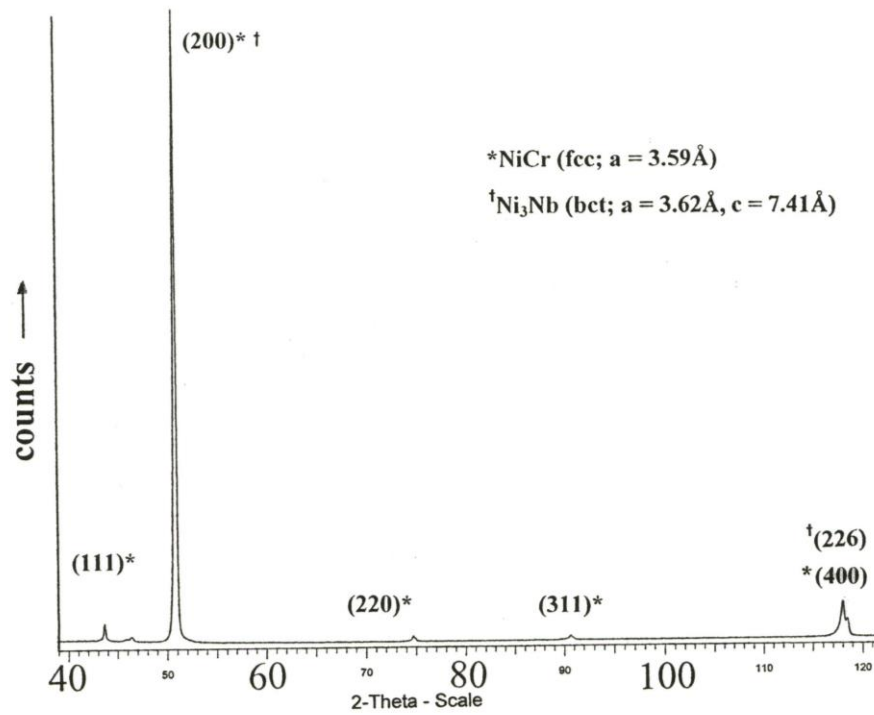


Figure 4.2.1 XRD spectra for Inconel 625 powders

HORIZONTAL SECTION



VERTICAL SECTION

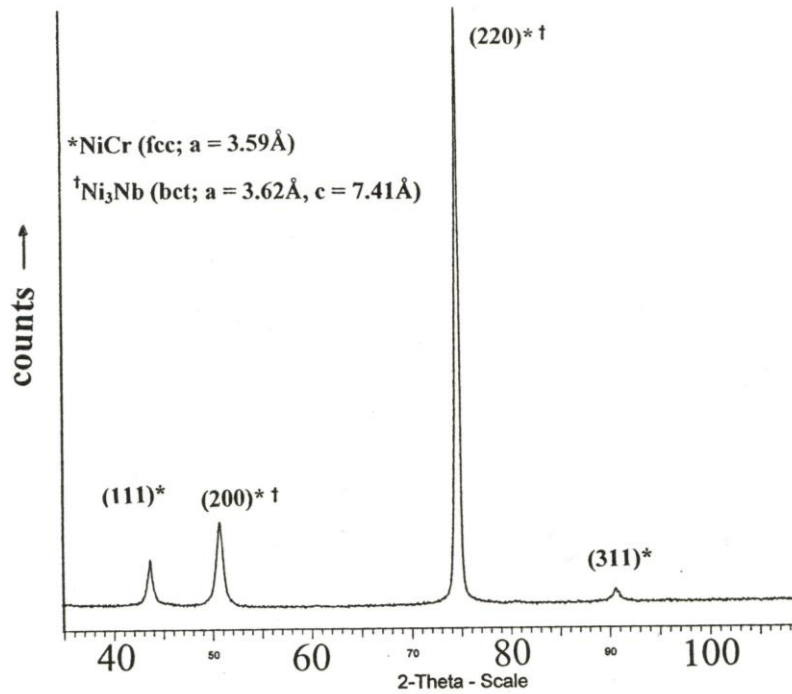


Figure 4.2.2 XRD spectra horizontal and vertical planes for sample from figure 4.1.4

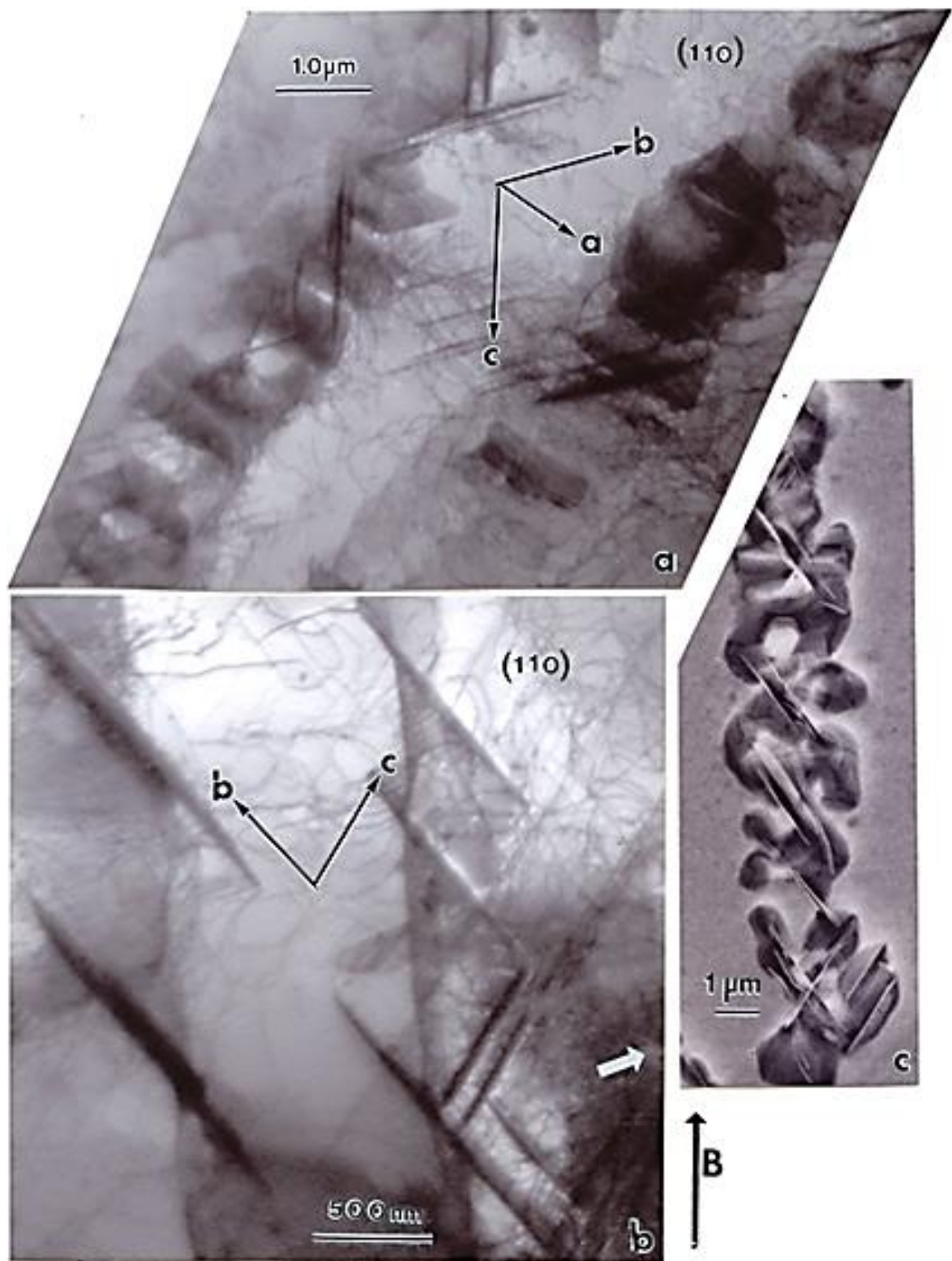


Figure 4.2.3 3D TEM image composition showing platelet precipitate arrays

4.3 INCONEL 625 MANUFACTURED BY SLM

The Inconel 625 components which were manufactured by SLM showed a similar columnar microstructure like the one seen in the components manufactured by EBM. Note the Inconel 625 were manufactured in z-axis orientation, parallel to the build direction, as well as in x or y axis, perpendicular to the build direction. These components were fabricated using the same pre-alloyed gas atomized powders that were used in the manufacturing of the components by EBM. The SLM components also contained the γ'' -Ni₃Nb precipitates as well as some melt pools that can be seen in figure 4.3.1 which is an image of a manufactured component in the z-axis. The melt pool contrast arises from enhanced precipitation of γ'' , also the columnar precipitate spacing is roughly half of what was seen in the EBM components. The spacing of the columnar microstructures in SLM was $\sim 2 \mu\text{m}$ which is slightly less than for the EBM spacing. Figure 4.3.2 is a magnified light optical microscopy image similar to the one seen in figure 4.3.1 but in this case the component was manufactured in the xy axis. The figure shows irregular columnar precipitate arrays as well as the melt pool features. The XRD spectra for the z-axis component, figure 4.3.1, showed a preferred orientation in [200] for both the horizontal and vertical reference planes this can be seen in figure 4.3.3. The XRD spectra for the xy axis component showed a preferred orientation in [200] for the horizontal plane and a preferred orientation in [111] for the vertical reference plane, figure 4.3.4, these orientations are different than what was observed in the EBM samples.

TEM was also done on the SLM components using the same electropolishing solution used for the EBM samples. Figure 4.3.5 is a 3D TEM image composition showing the columnar precipitation within dense dislocation arrays. The dense dislocation arrays are associated with the nano sized γ'' precipitate columnar arrays, the γ'' precipitates diameter was measured to range from 10 to 20 nm. Figure 4.3.6 compares LOM and SEM images for the vertical reference plane showing the columnar precipitation as well as the melt pools or melt bands. It can clearly be seen by the SEM image, figure 4.3.6b, that the γ'' make up the melt bands in the vertical reference plane of our samples, these precipitates are etched out as a result of the etchant solution which was used. [15]

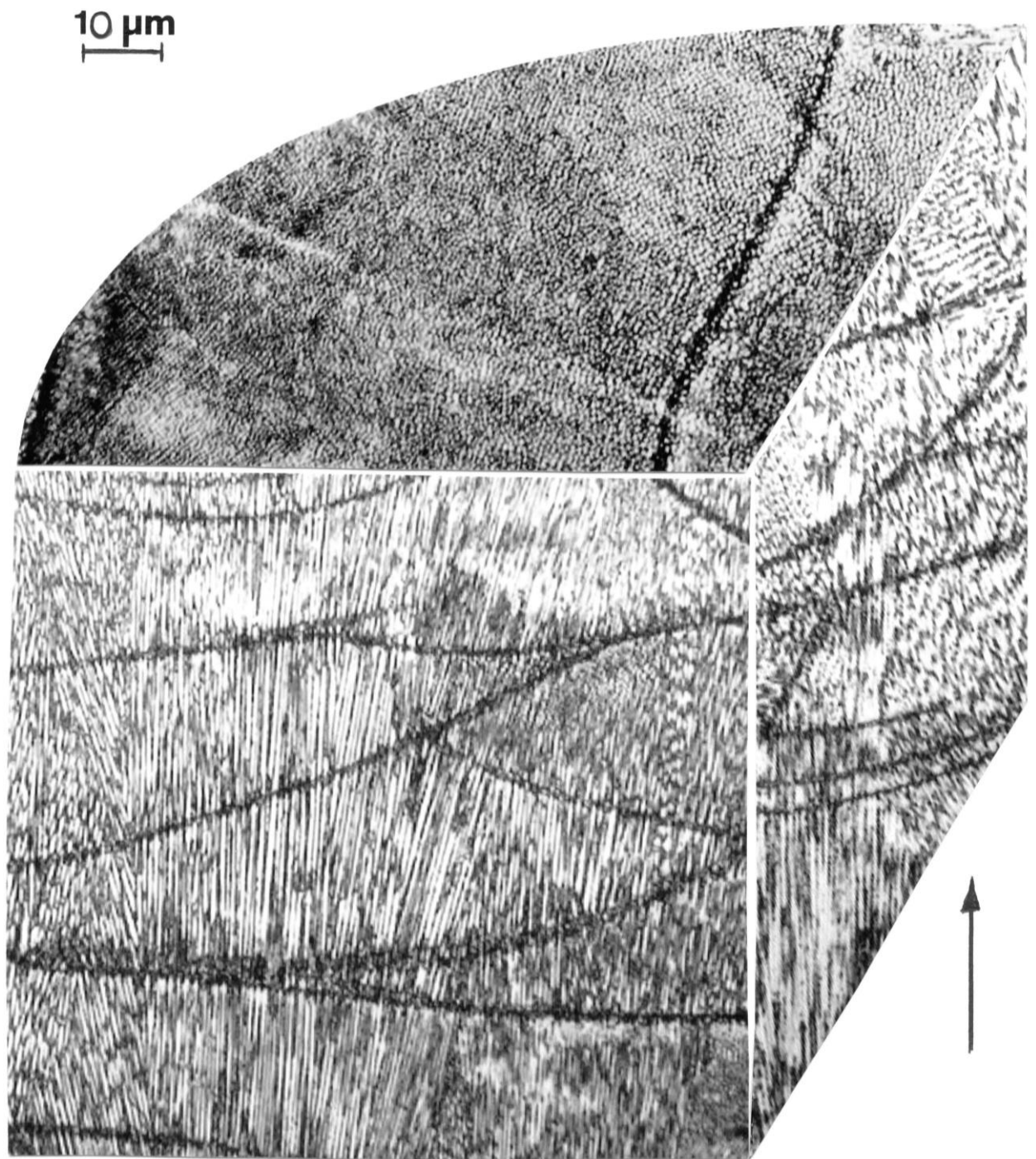


Figure 4.3.1 Inconel 625 manufactured by SLM in z-axis showing columnar microstructure and melt pools

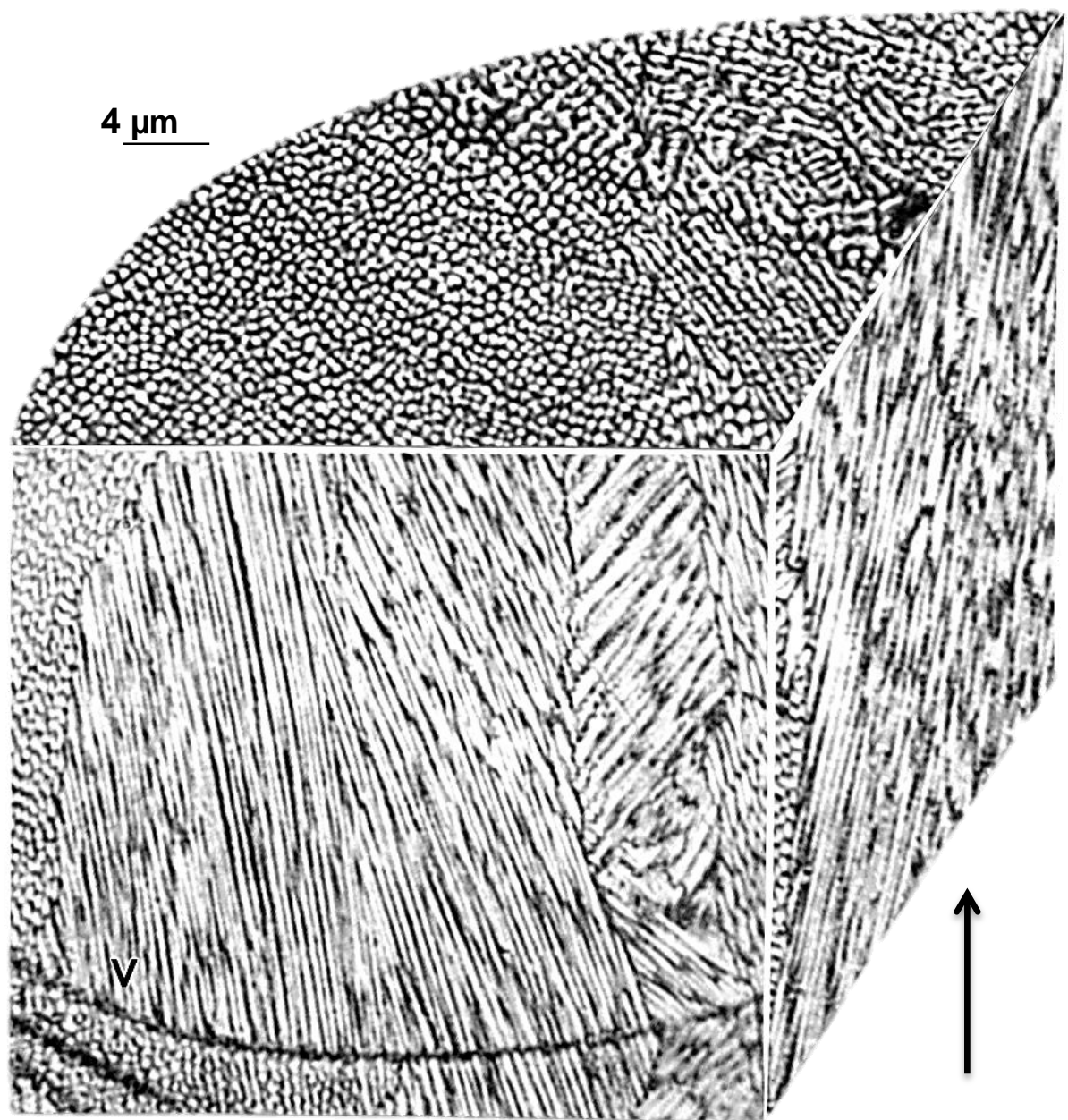


Figure 4.3.2 3D image composite of SLM component manufactured in xy axis

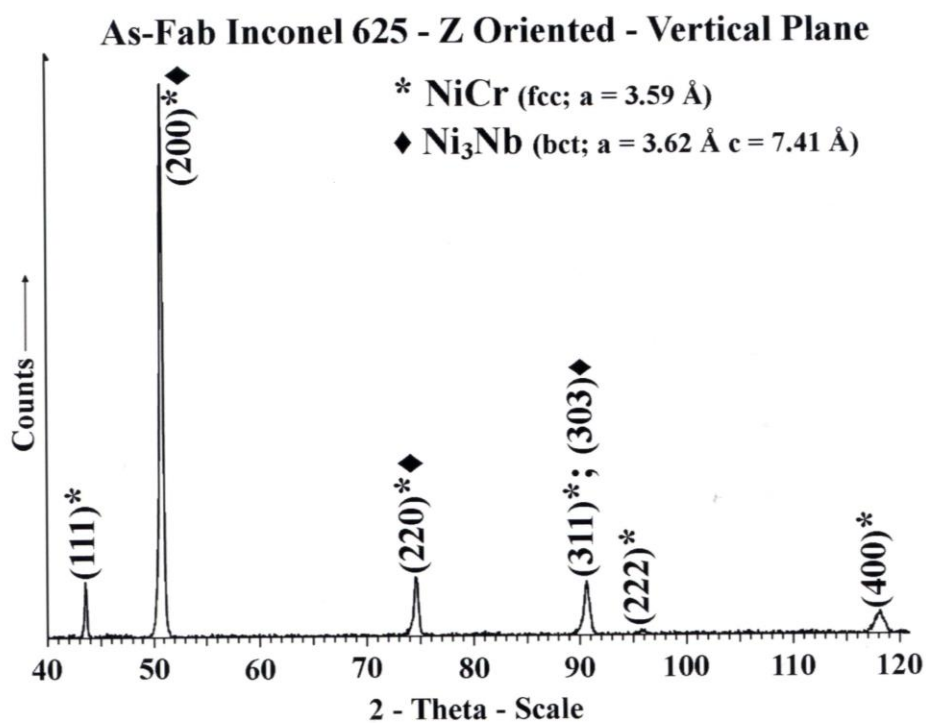
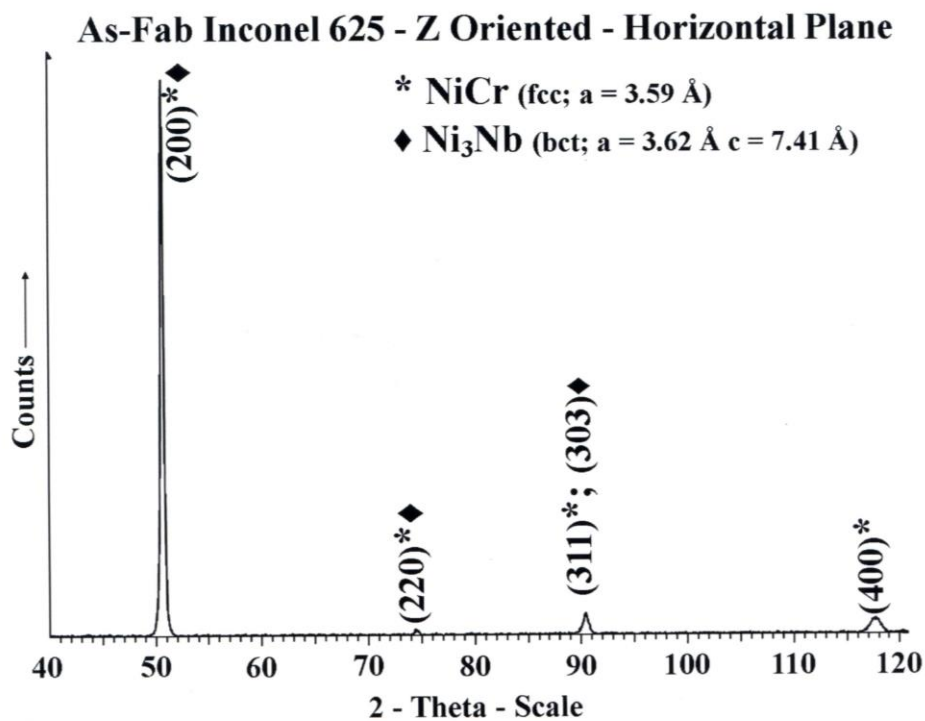


Figure 4.3.3 XRD Spectra for Z oriented component manufactured by SLM

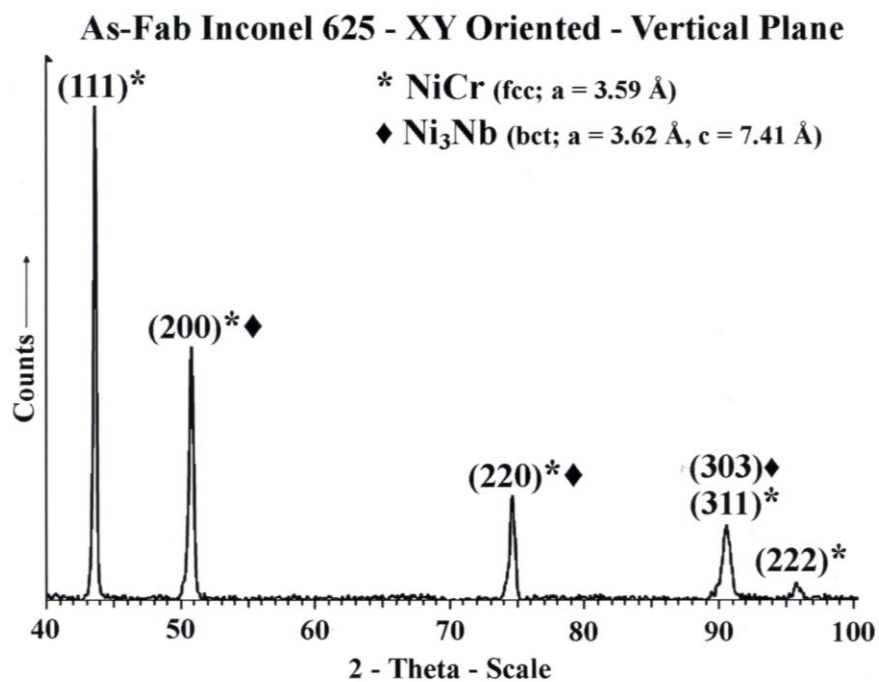
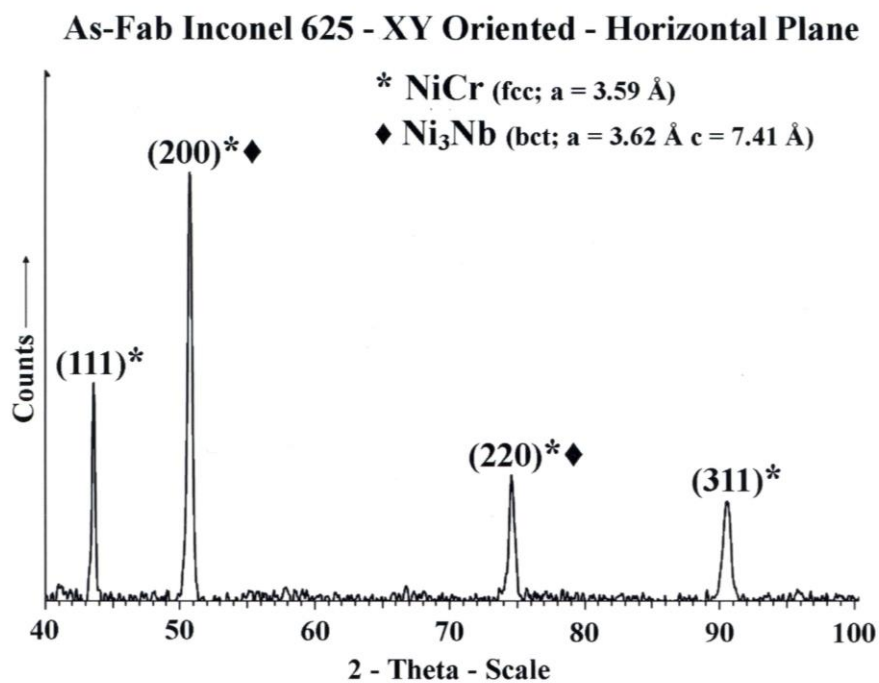


Figure 4.3.4 XRD Spectra for xy oriented component manufactured by SLM

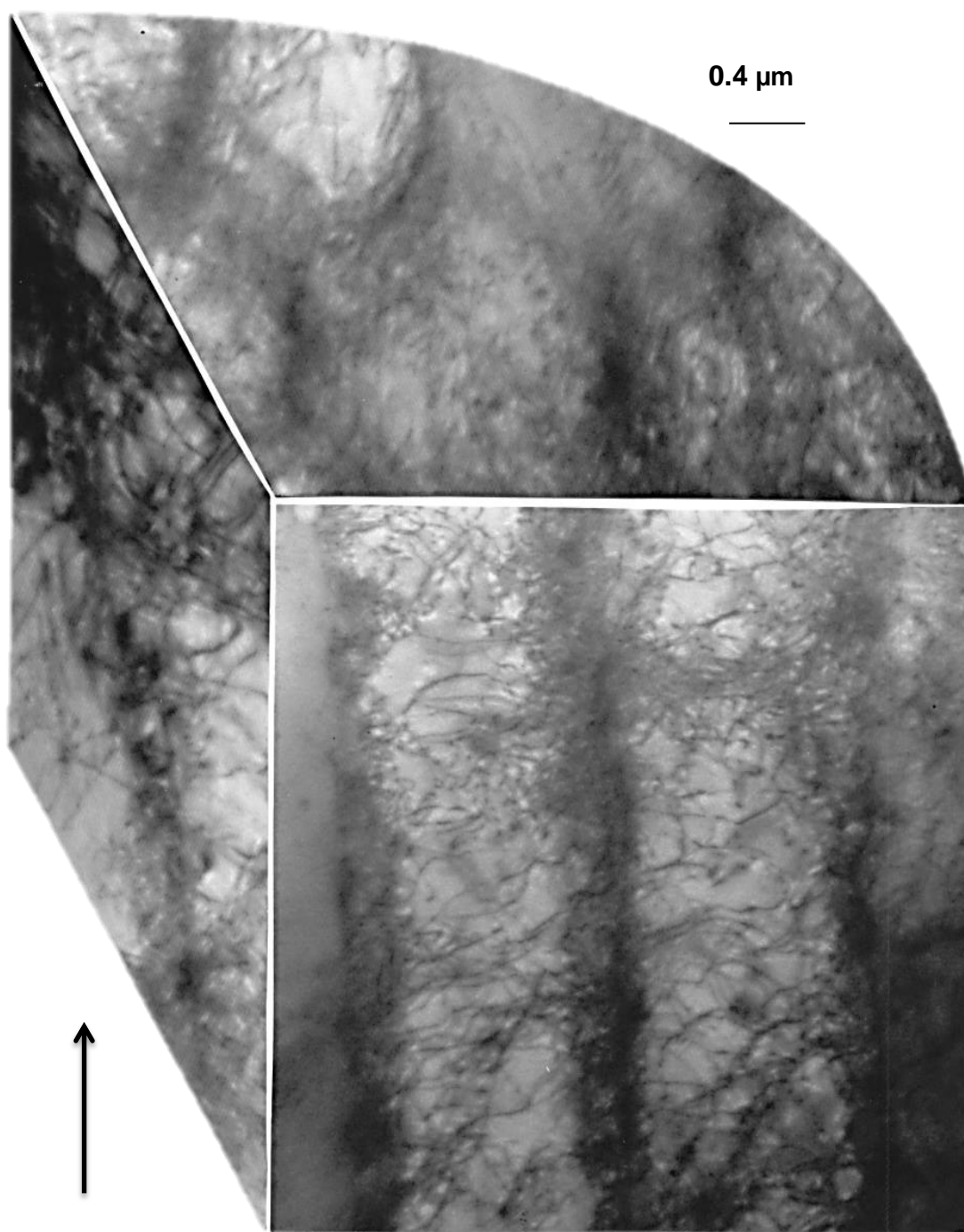


Figure 4.3.5 3D TEM image composition showing high dislocation density and columnar precipitates

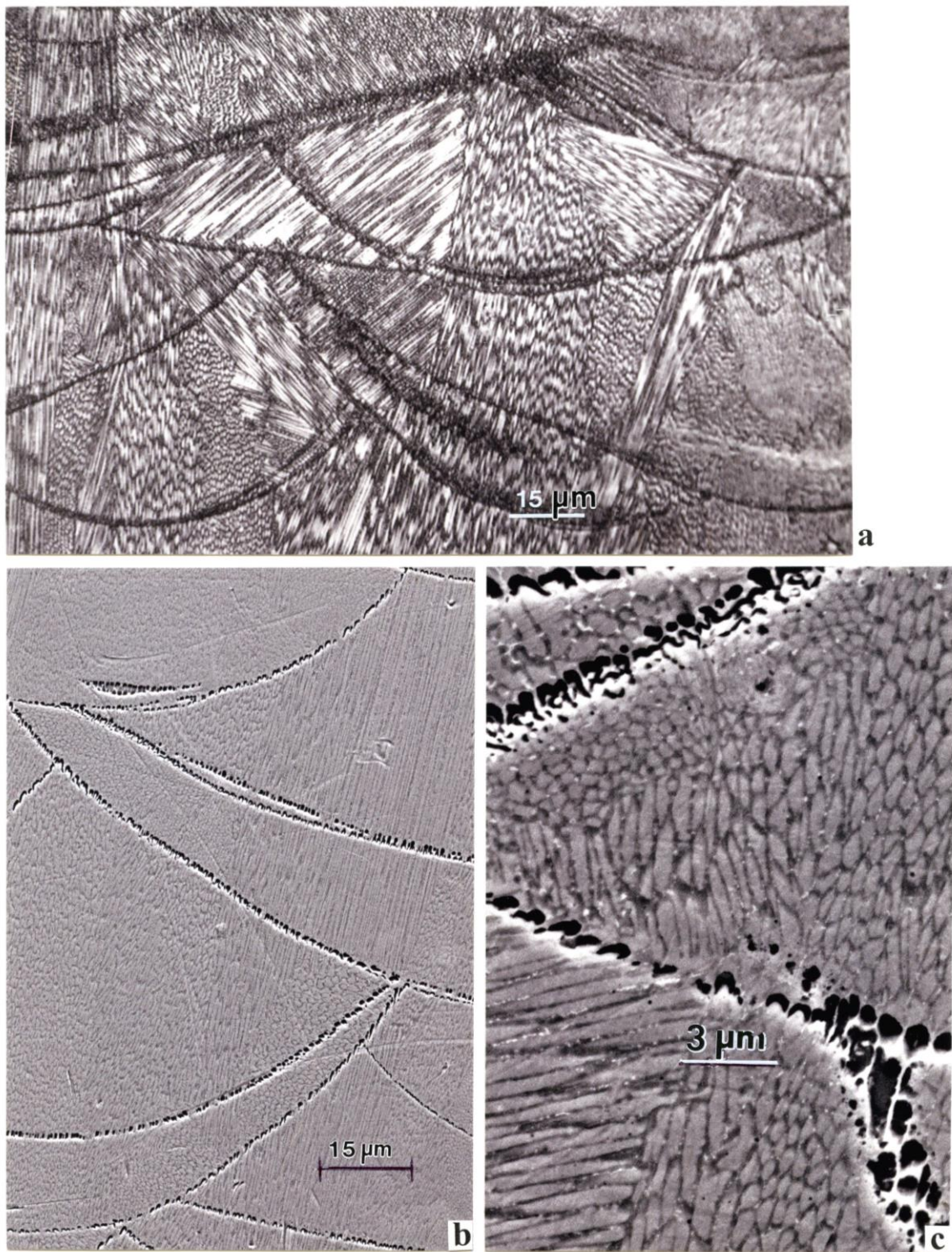


Figure 4.3.6 a) LOM vertical plane b) low magnification SEM showing γ formation at melt pool c) magnified SEM image showing precipitation

Chapter 5

17-4 PH Stainless Steel Microstructures from SLM

5.1 17-4 PH STAINLESS STEEL POWDERS

17-4 precipitate hardenable (PH) stainless steel (15-17.5Cr, 3-5Ni, 3-5Cu, <1Mn, Si, 0.15-0.45 Nb balance Fe in weight percent) was manufactured by SLM using argon gas as well as nitrogen gas. The powders used in the manufacturing process were 17-4PH nitrogen atomized powders as well as 17-4PH argon atomized powders. The powders were mounted, ground, polished and electroetched using a solution of 100 mL HCl, 100 mL ethanol, 5 g CuCl₂ for 10-20 seconds at room temperature. Figure 5.1.1 shows the similar microstructures of the argon atomized and nitrogen atomized powders images a) and b) respectively; the microstructures are equiaxed structures that have an average grain size of 4 μm . The average particle size for the argon (Ar) powder was measured to be 19 μm and the average particle size for the nitrogen (N₂) powders was measured to be 25 μm ; the powders are seen in figure 5.1.2 which shows the powder distributions as seen by SEM. Figure 5.1.3 shows the XRD spectra for the nitrogen and argon precursor powders which indicates that the argon atomized powder is α -Fe (ferrite/martensite) while the nitrogen atomized powder was primarily γ -austenite.

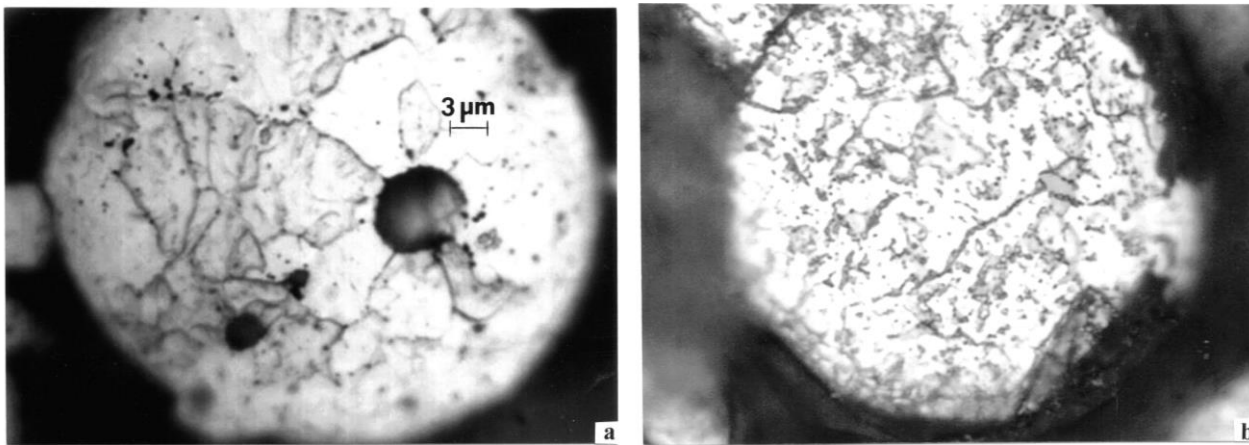


Figure 5.1.1 a) cross section of argon atomized powder b) cross section of nitrogen atomized powder

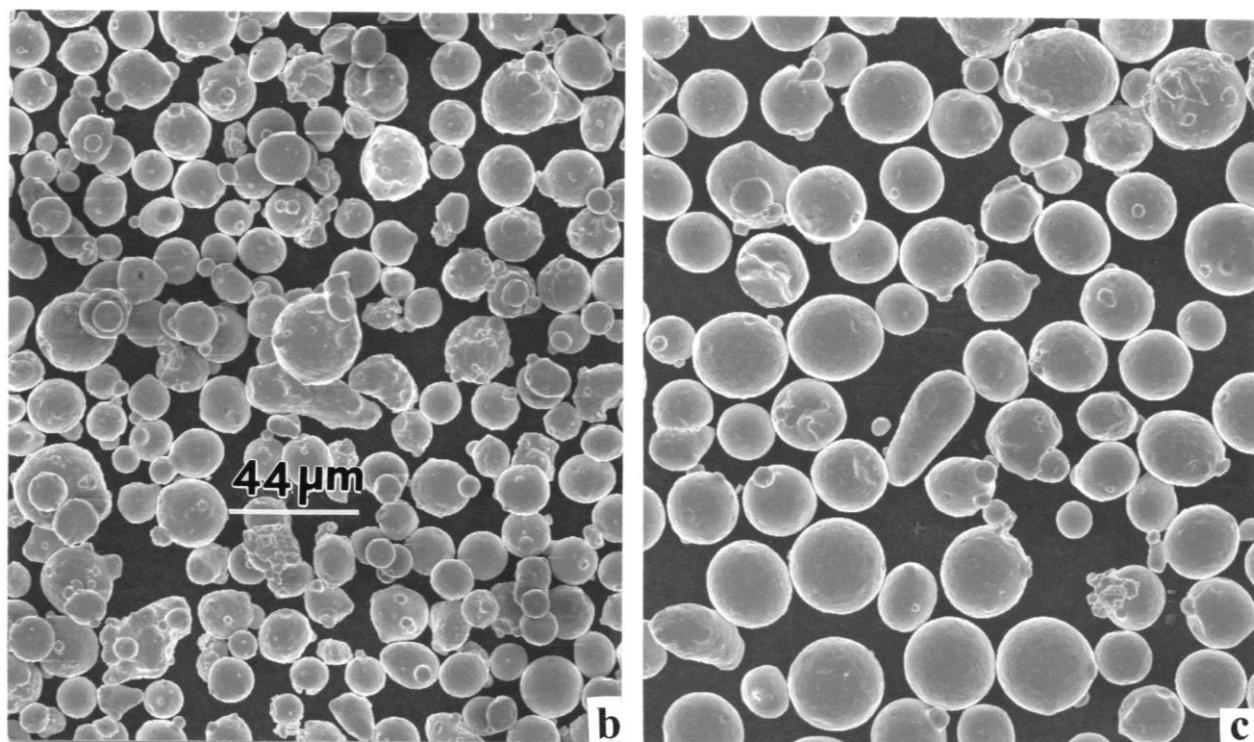


Figure 5.1.2 a) argon atomized powder b) nitrogen atomized powder

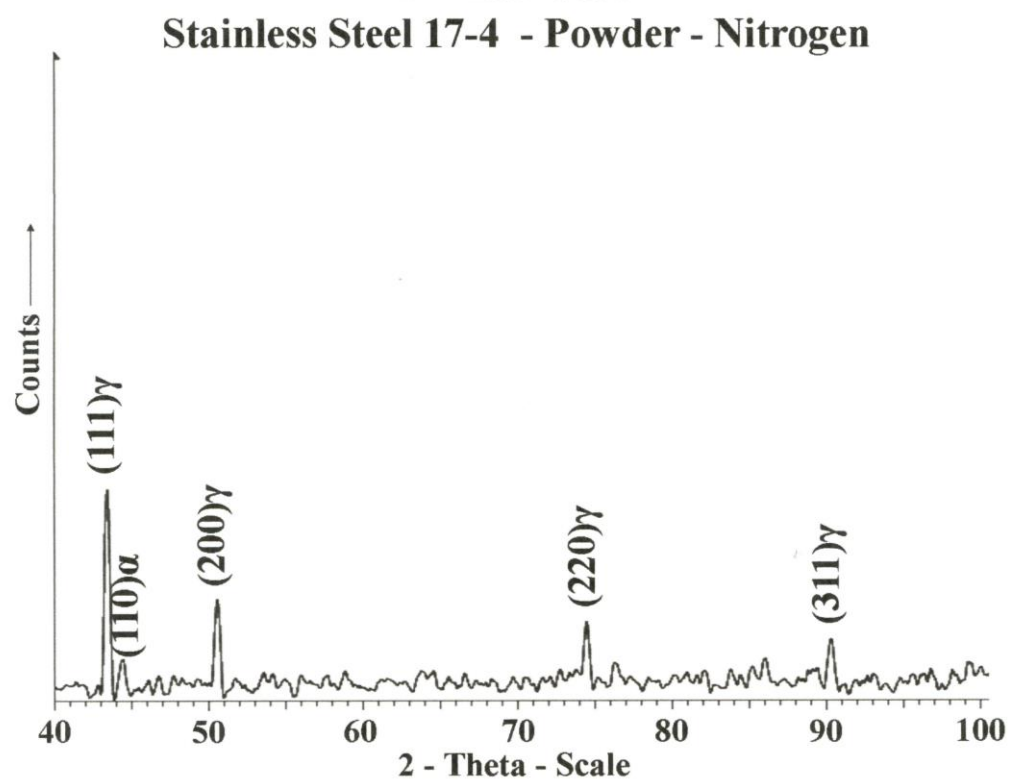
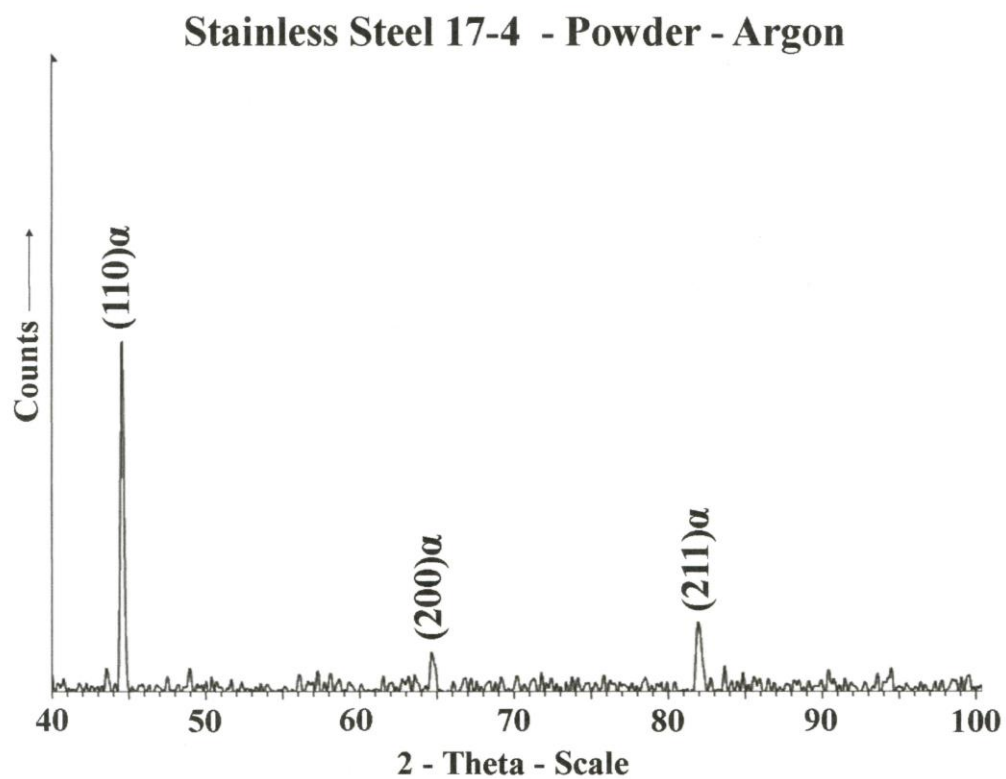


Figure 5.1.3 XRD Spectra for precursor powders

5.2 AR AND N₂ POWDER COMPONENTS MANUFACTURED IN ARGON

As mentioned earlier 17-4 PH stainless steel components were manufactured in both argon and nitrogen environments by SLM, some samples were also manufactured in argon-nitrogen alternating; all of these components exhibited interesting microstructures. Figure 5.2.1 shows a 3D light microscopy image, arrow shows the build direction, of a component that was manufactured using argon atomized powder in an argon environment. The figure shows columnar martensite (α -Fe ferrite:bcc) structures, with sizes from ~5 to 50 μm , which are parallel to the build direction. This figure also shows the melt pools which are caused by the laser during fabrication by SLM, these features are more prominent in the vertical direction. XRD for the argon/argon manufactured component can be observed in figure 5.2.2 the horizontal direction is (200) plane, perpendicular to the build direction and the vertical direction is characterized by the (110) plane, this is parallel to the build direction.

Like the components manufactured from argon powder in an argon gas environment, (argon/argon), the nitrogen/argon components showed a similar columnar martensitic structure; this is seen in figure 5.2.3. Although the microstructure for the N₂/Ar components was essentially the same textured martensite as the Ar/Ar components there were some differences seen in the XRD spectra, figure 5.2.4. In the case for the N₂/Ar components the horizontal plane texture contained some (110) oriented microstructures in addition to (200) but the vertical plane, like the Ar/Ar components, was strongly textured (110) α . Note that the powder atomized in argon was martensitic, (α -Fe), and that the manufactured components in argon environment were also martensitic and that the austenitic nitrogen atomized powder also produced a martensitic structure when components were manufactured in argon gas.

TEM analysis was also done on the as fabricated Ar-N₂, Ar-Ar, and N₂/N₂ components. The coupons were electropolished using a solution of 95 percent acetic acid and 5 percent perchloric acid at 10°C at a voltage of 30 V. The vertical reference plane analyzed by TEM for the Ar/Ar components, figure 5.2.1, can be seen in figure 5.2.5(a) which shows heavily dislocated lath martensite which are oriented in the build direction indicated by the white arrow in the image. The figure also contains a selective area electron diffraction (SAED) pattern showing a (110) α grain surface which corresponds to the (110) α textured seen in the XRD, figure 5.2.2. Figure 5.2.5(b) is a magnified TEM image which

shows the tangled dislocation substructure in the (110) α lath martensite grains having a density of $\sim 10^{11}$ cm^{-2} . [9,12]

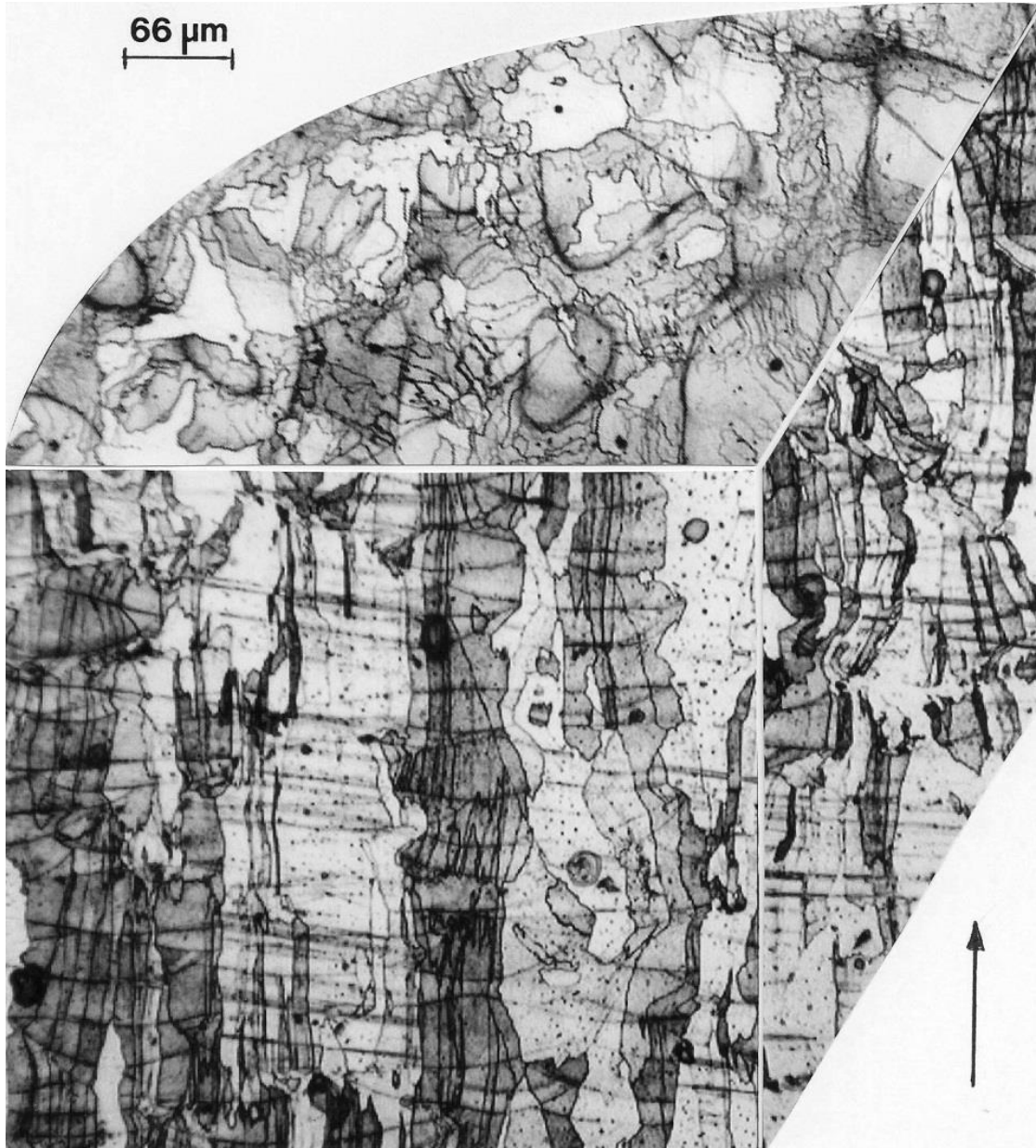


Figure 5.2.1 Argon powder as fab in argon gas

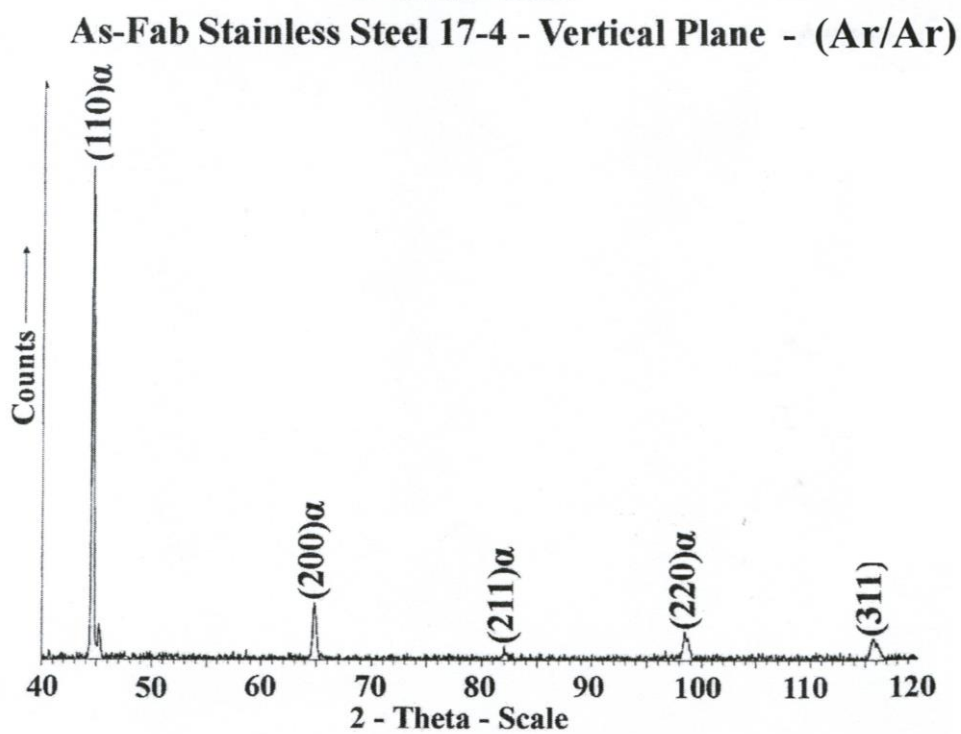
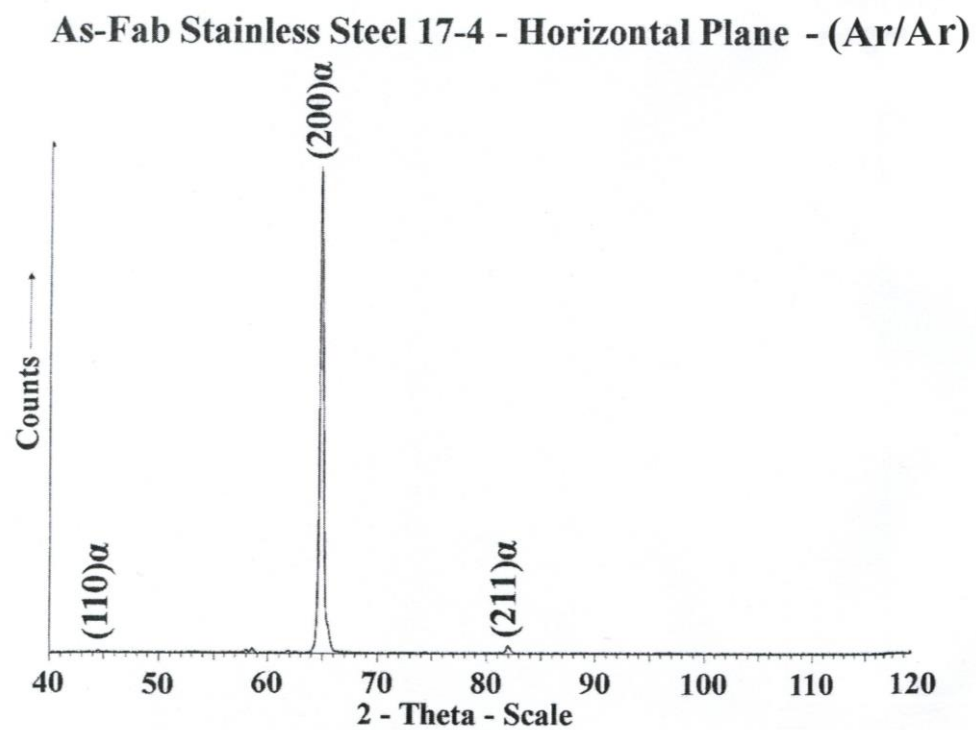


Figure 5.2.2 XRD spectra for Ar/Ar components

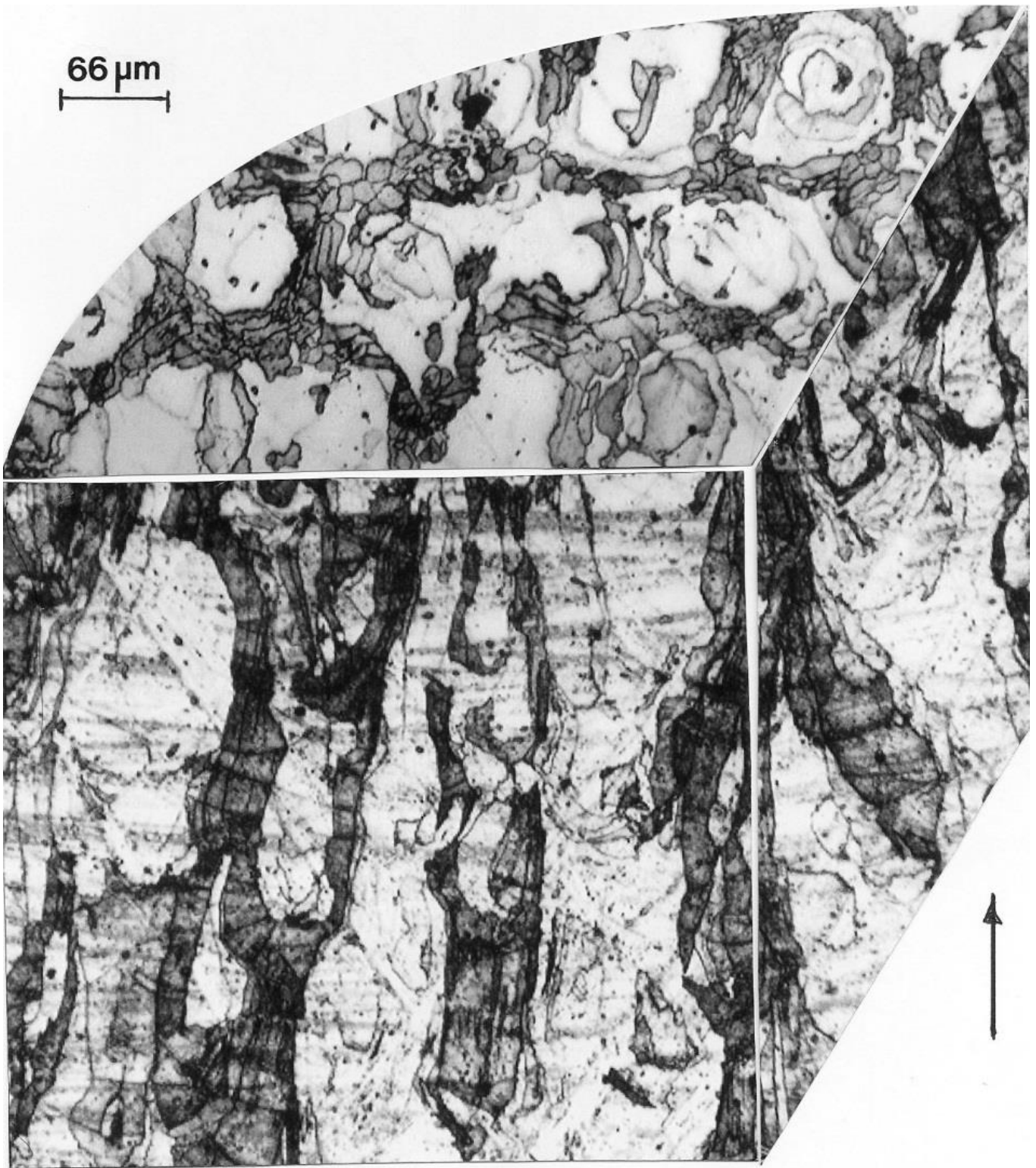
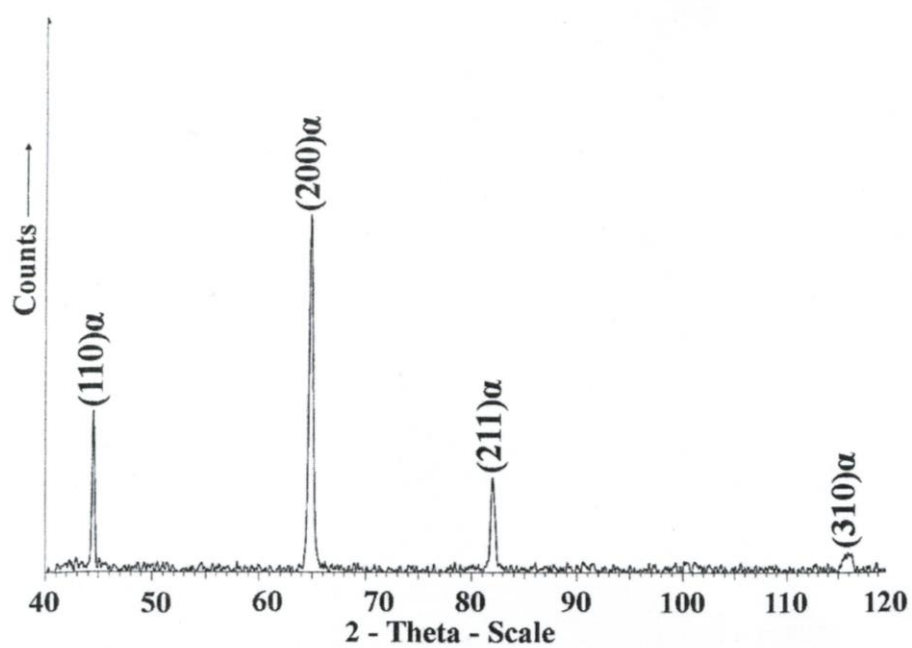


Figure 5.2.3 Nitrogen powder as fab in argon gas

As-Fab Stainless Steel 17-4 - Horizontal Plane - (N2/Ar)



As-Fab Stainless Steel 17-4 - Vertical Plane - (N2/Ar)

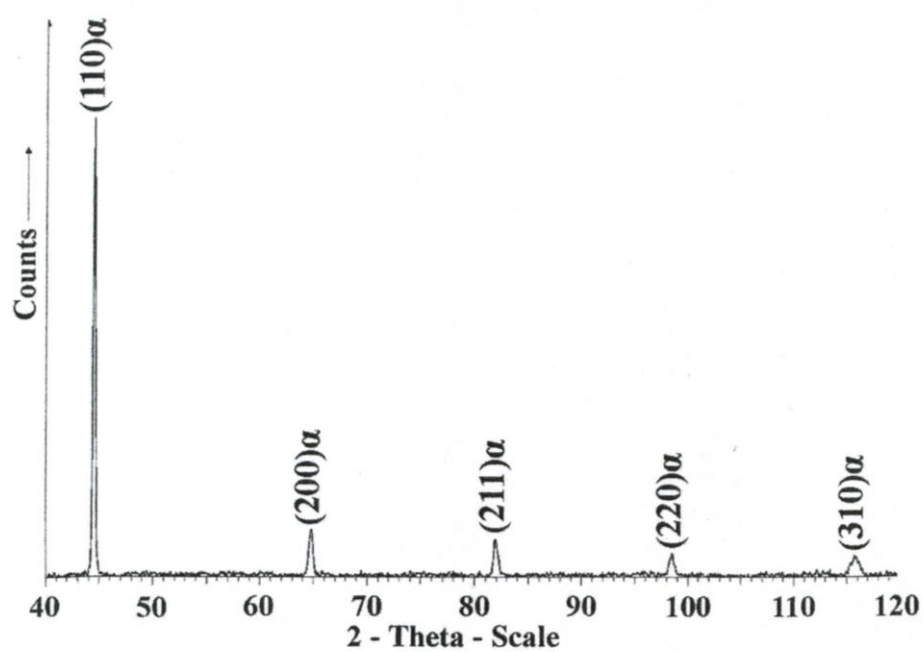


Figure 5.2.4 XRD spectra for N2/Ar components

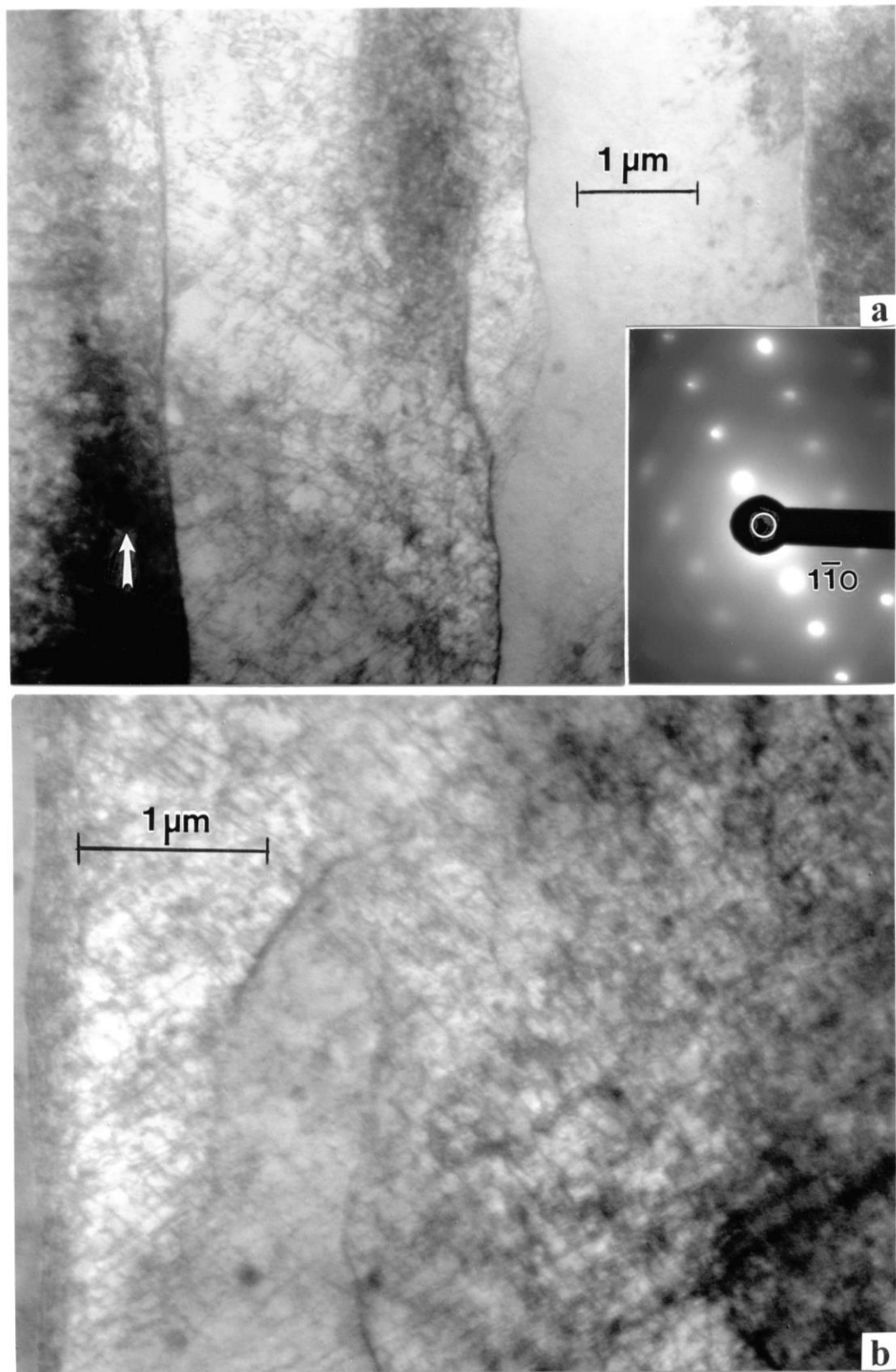


Figure 5.2.5 TEM image for vertical reference plane

5.3 N2/N2 MANUFACTURED COMPONENTS

Figure 5.3.2 shows the microstructure of components that were fabricated using nitrogen atomized powder in a nitrogen environment (N2/N2), this 3D light microscopy image shows a different microstructure to the 17-4 PH components mentioned earlier. The XRD spectrum, figure 5.3.2, shows that the N2/N2 component is primarily austenitic (γ (fcc)-Fe) with $[220]\gamma$ texturing in the horizontal direction and $[111]\gamma$ texturing in the vertical direction. The N2/N2 component also contains some α -Fe, martensite, peaks in both direction, although they are fairly weak. Note the Ar/Ar and N2/Ar components were magnetic while the N2/N2 was not magnetic.

Figure 5.3.3 shows a TEM bright field image of the N2/N2 component showing dislocations, stacking fault traces as well as deformation twin faults shown by the arrow in austenite grains mixed with martensite in the build, or vertical, direction. The stacking faults or twin fault segments are coincident with $[\bar{1}12]$ fcc. The diffraction pattern insert, SAED pattern, in figure 5.3.3 shows a mixture of bcc- α and fcc- γ reflections corresponding to a $[110]$ superimposed bcc and fcc ($[220]$) zone axis.

Alternating gas in build chamber

Besides manufacturing Ar/Ar, N2/Ar, and N2/N2 components we also manufactured some components with alternating argon and nitrogen throughout the build; the gas kept being changed every so often to see how the alternating gas would affect the structure. For this alternating gas component we analyzed the top and the bottom of a cylindrical component to see if the change in the gases affected the microstructure of the component with varying height. Figure 5.3.4 is from the top of the cylindrical component which shows some random acicular alpha martensite grains, the arrow in the figure shows the build direction. The XRD spectra for the top of the cylinder as seen in figure 5.3.5 indicates that it is mostly martensite (α -Fe:bcc) with strong texture in (110) for both the horizontal and the vertical reference planes. The bottom of the cylinder which is seen in figure 5.3.6 shows a microstructure which consists of 15% austenite as well as 85% martensite. The XRD spectra for the bottom portion of the cylindrical component, figure 5.3.7, also showed strong texture in (110) for both the horizontal and vertical reference planes as well as it being mostly martensite α -Fe. [8, 12]

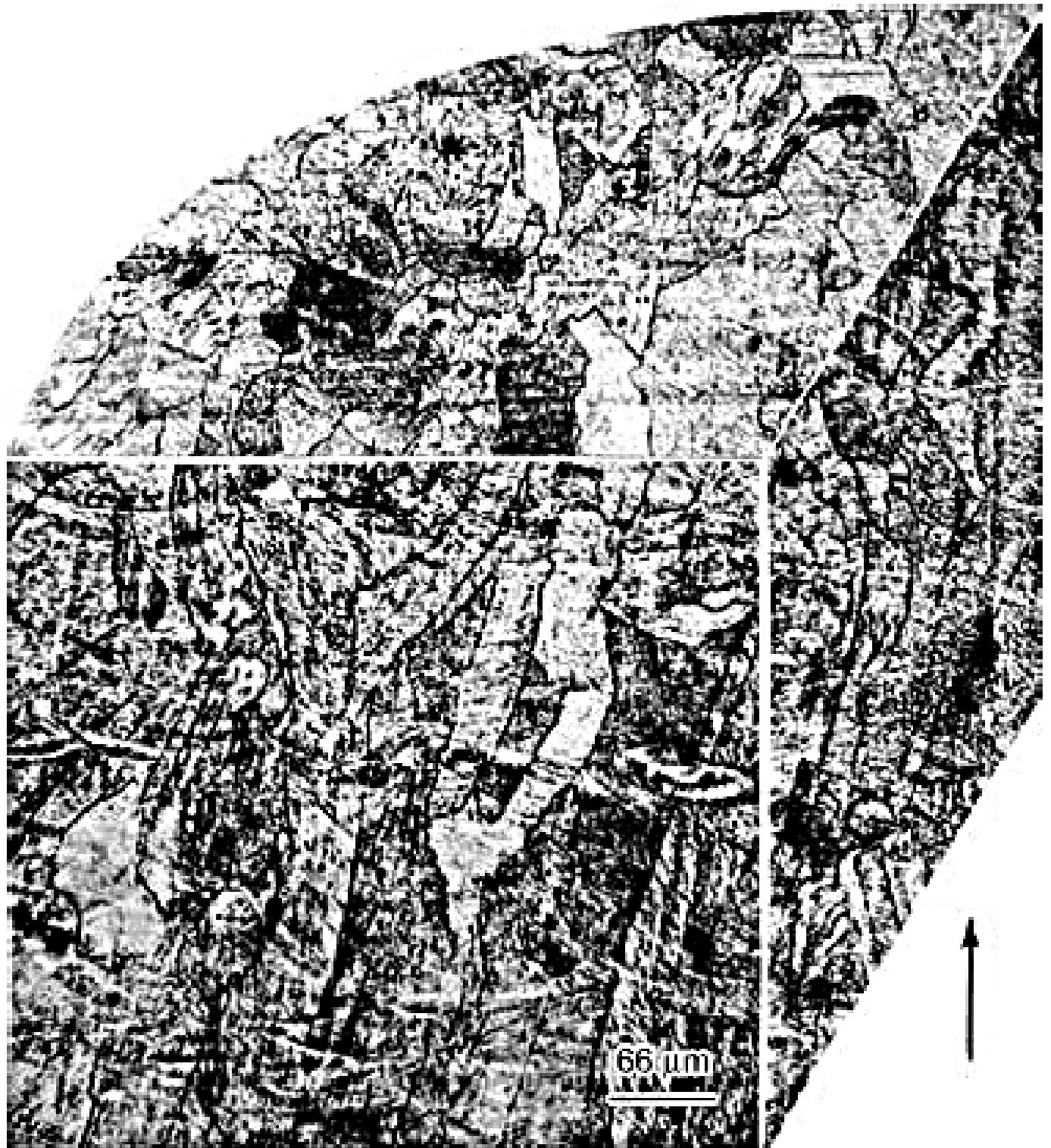


Figure 5.3.1 N2/N2 3D LOM showing austenitic microstructure

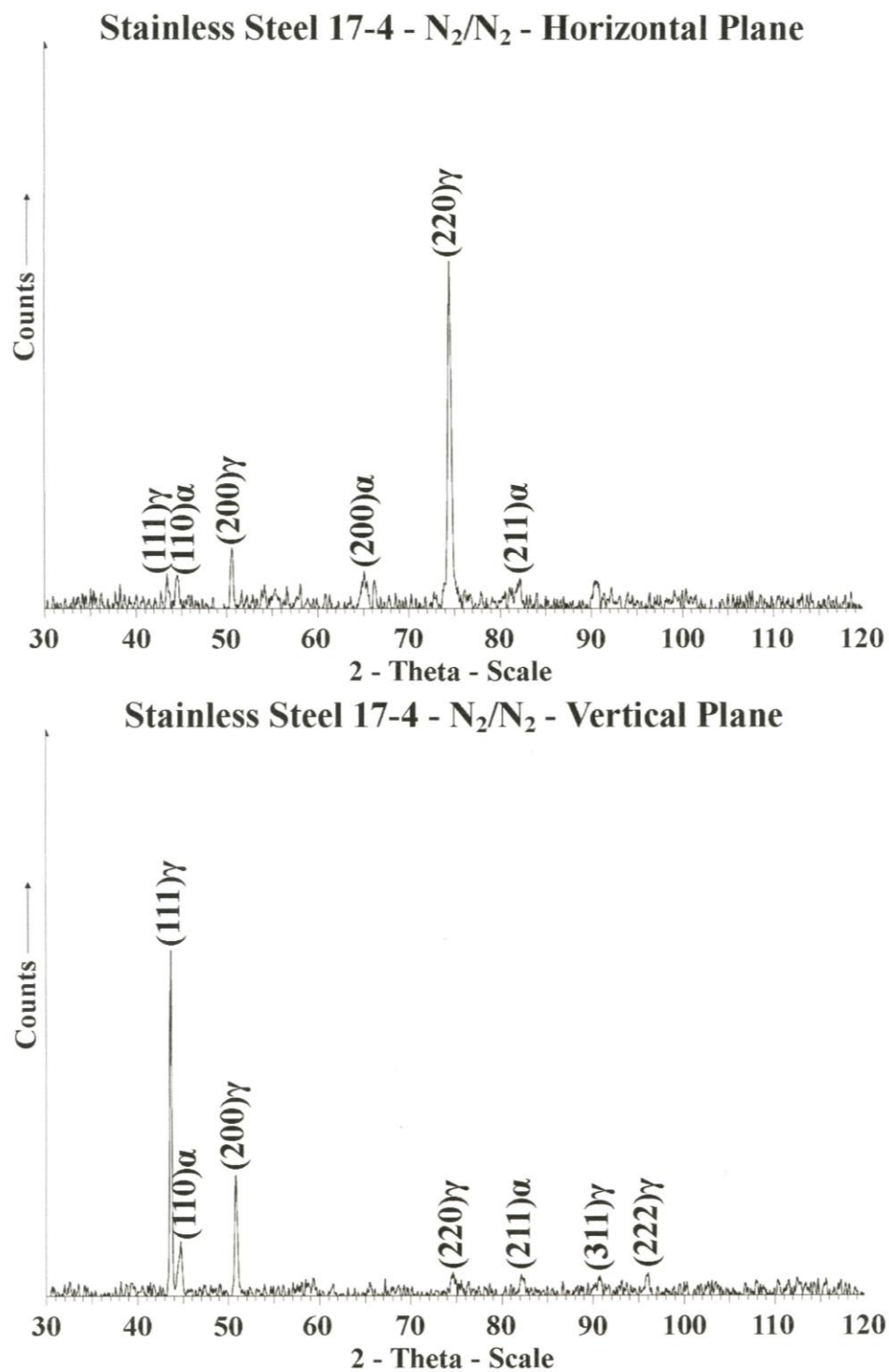


Figure 5.3.2 XRD spectra for N₂/N₂ manufactured component

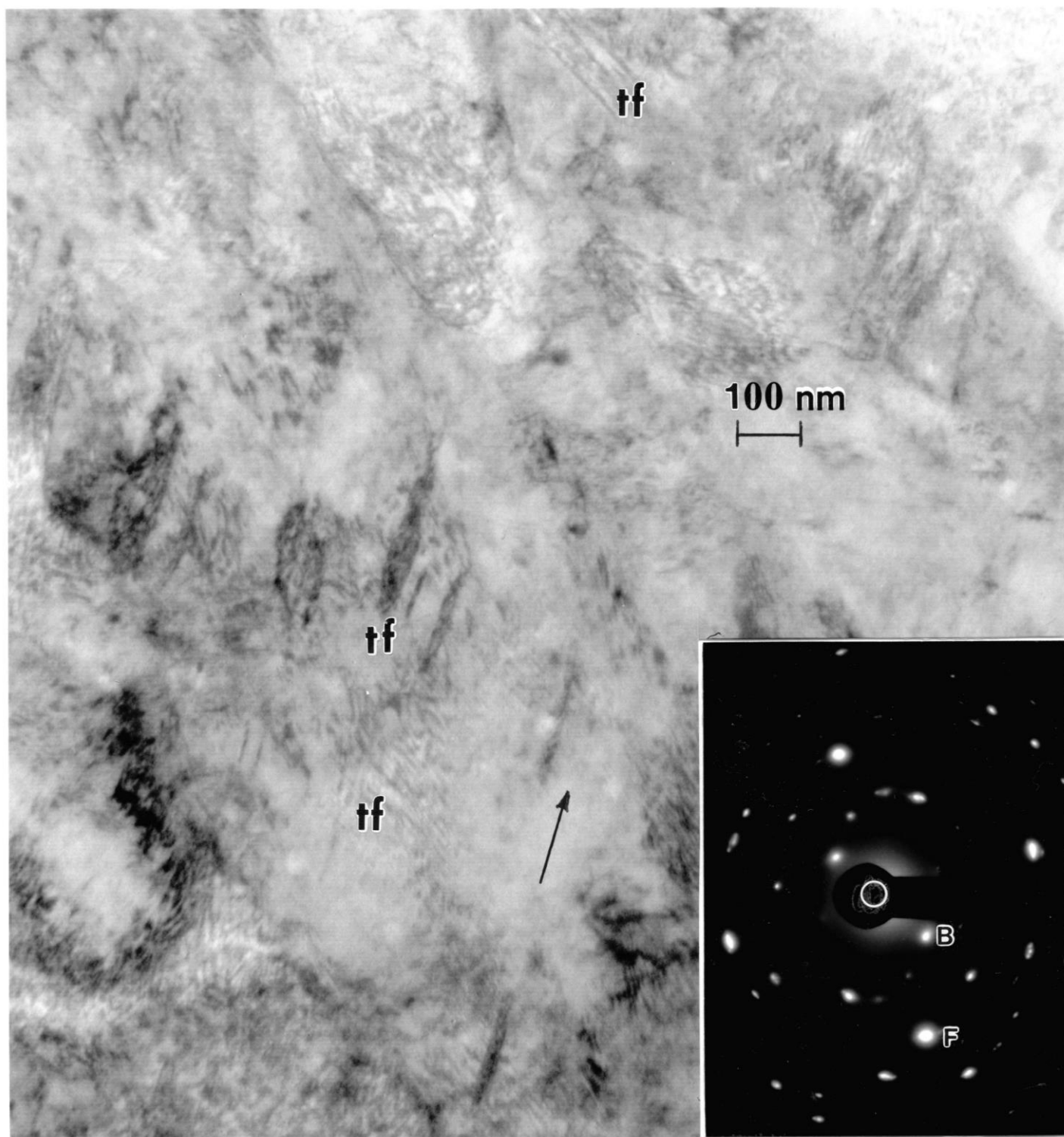


Figure 5.3.3 TEM bright field image for the vertical reference plane N2/N2 component

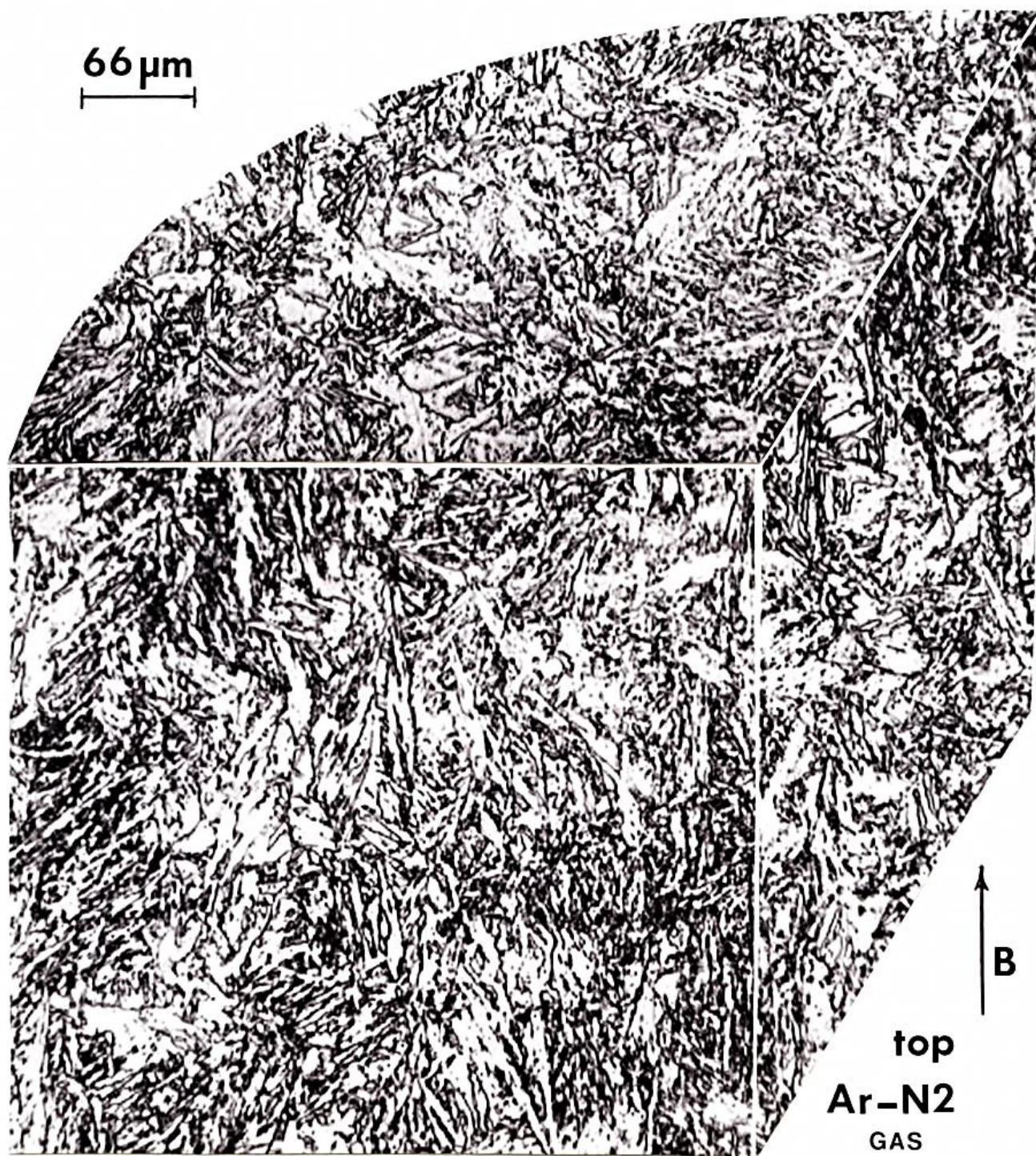


Figure 5.3.4 3D LOM of Ar-N2 alternating manufactured component

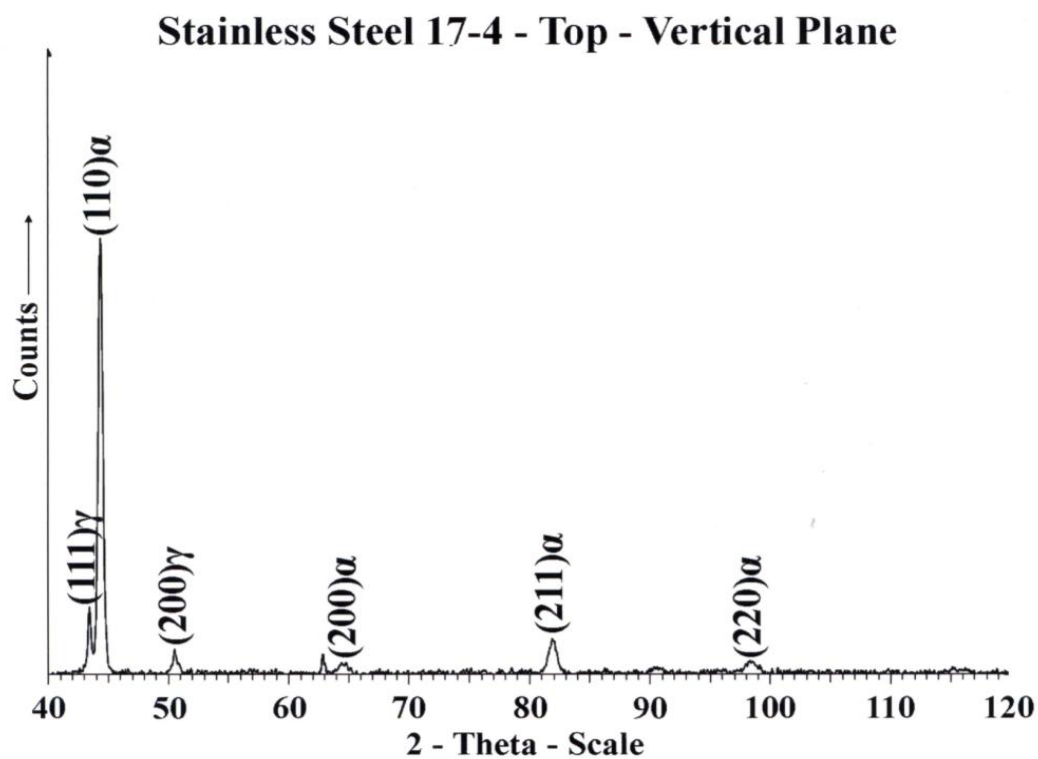
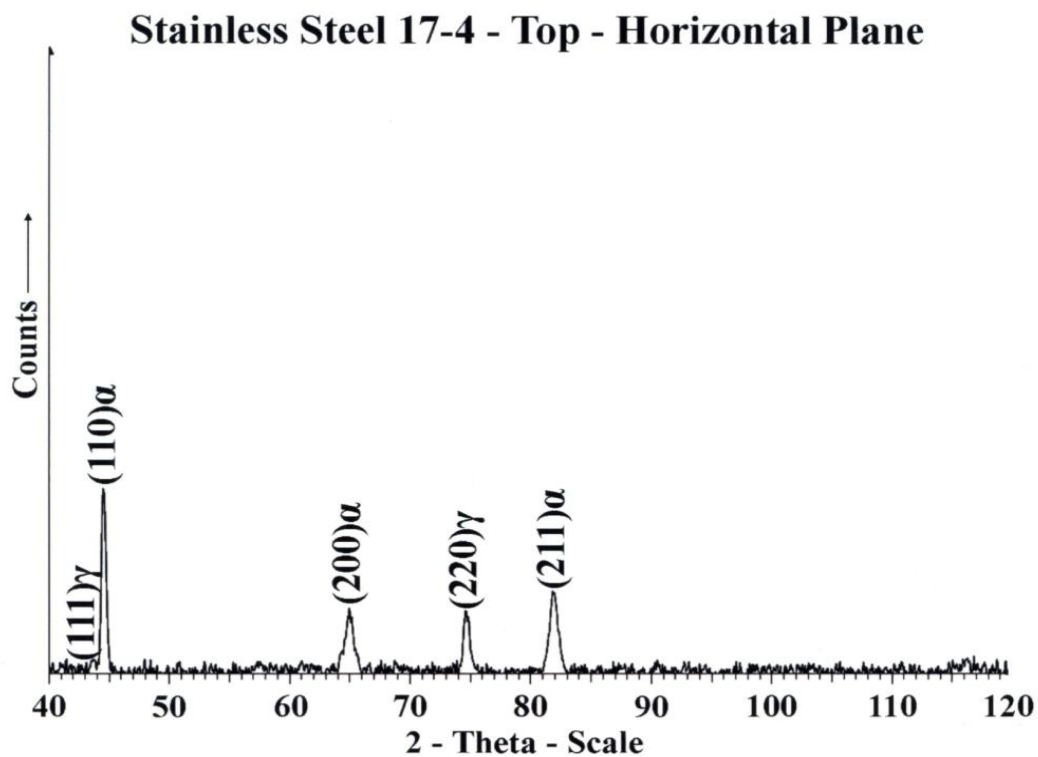


Figure 5.3.5 XRD spectra for top section of cylindrical component

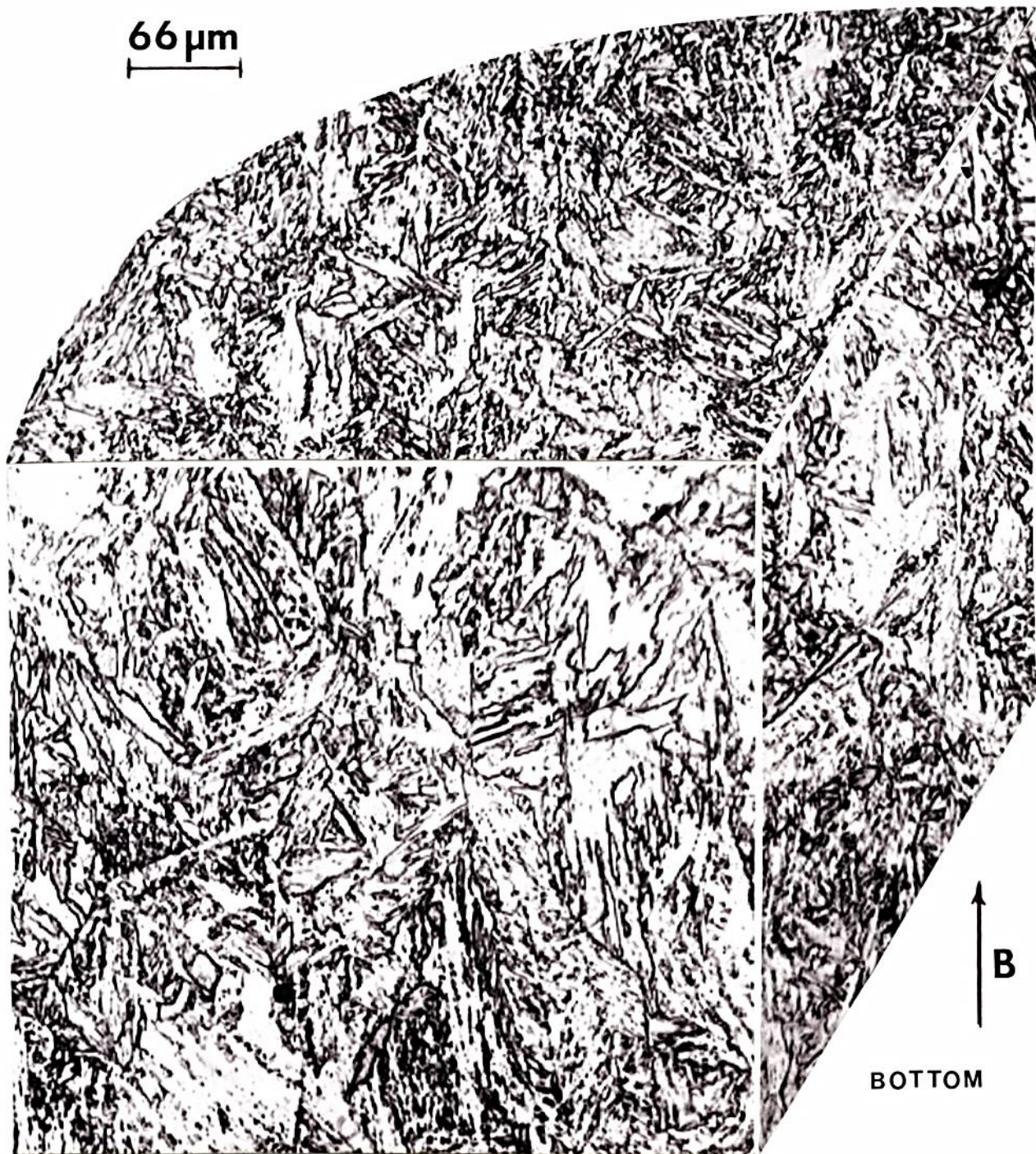


Figure 5.3.6 3D LOM of bottom of cylinder of alternating gas component

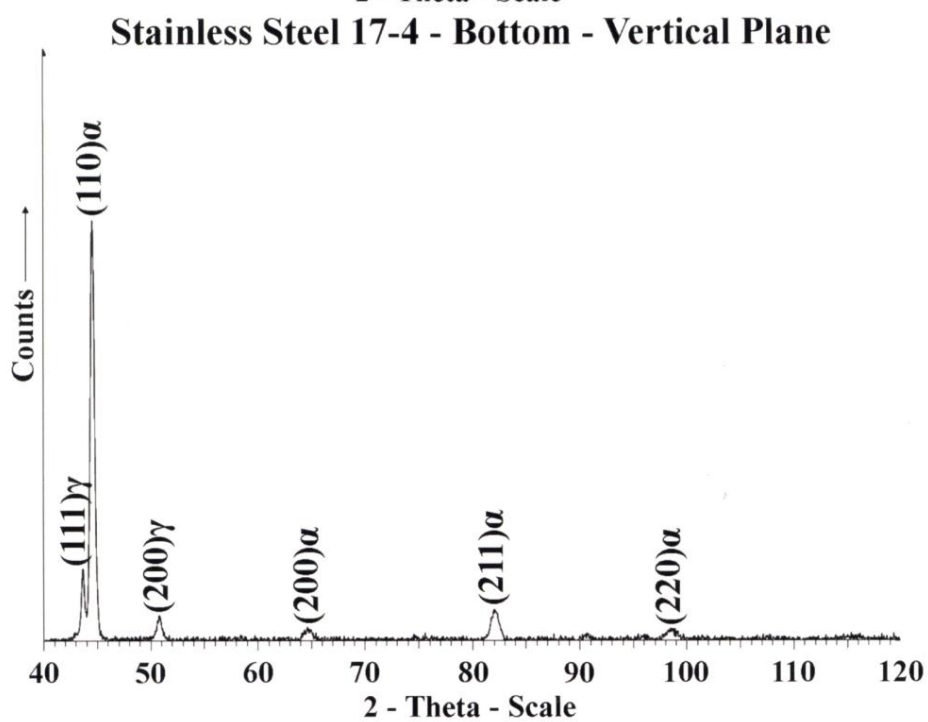
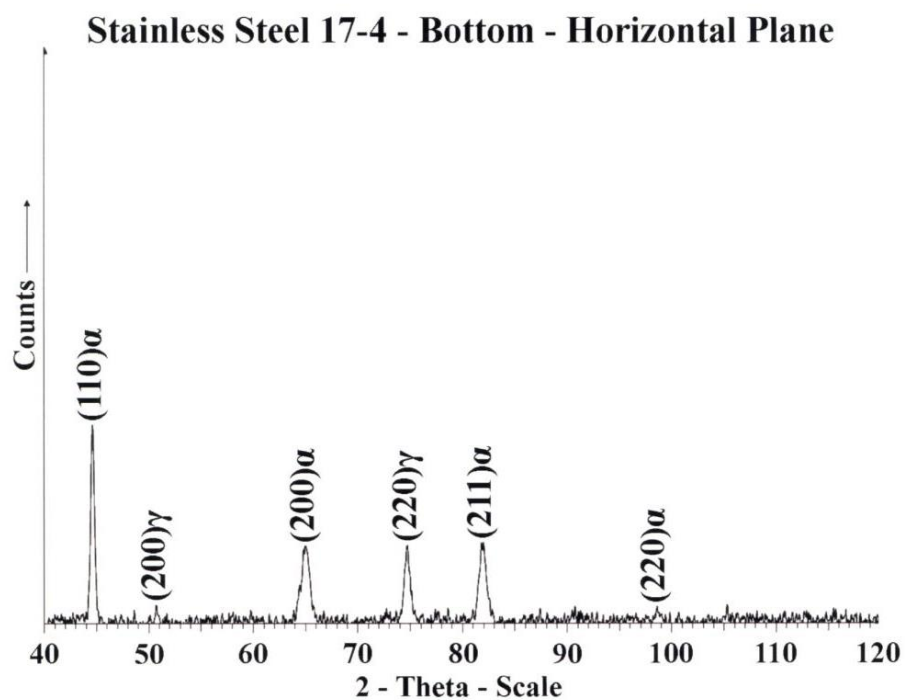


Figure 5.3.7 XRD spectra for bottom portion of cylindrical component

Chapter 6

Inconel 718 Manufactured by SLM

6.1 INCONEL 718 POWDERS AND FABRICATION

Nickel-base superalloys, with ranging alloy composition, have found a wide range of application in the industrial and aerospace fields. Inconel 718 has been used mostly in gas turbine blades, combustors, turbocharger rotors, and structural applications of up to $\sim 700^{\circ}\text{C}$. The Inconel 718 prealloyed, atomized powder had a composition of 53.5Ni-19Cr-18.3Fe-5Nb-3Mo-1Ti-0.43Al. The powder was analyzed by SEM to check the microstructure as well as the particle size, the average particle size was $17\text{ }\mu\text{m}$ and the powders had a microdendritic structure as seen in figure 6.1.1a. The powders were also mount, ground polished and electro etched using a solution of 70 mL phosphoric acid and 30 mL water at room temperature from 5 seconds to 120 seconds at 5 volts. The cross section of the etched powders can be observed in figure 6.1.1b which also shows a microdendritic structure. Cylindrical components having a diameter of 1.6 cm and a length of 8.75 were fabricated in both horizontal (x-axis) and vertical (z-axis) build orientation; the cylinder axis was either parallel or perpendicular to the beam direction. The build table in the SLM, figure 1.2.1, was preheated to 80°C and was maintained at that temperature throughout the building process and the $100\text{ }\mu\text{m}$ diameter laser beam was scanned at 800 or 1200 mm/s in either argon or nitrogen environments. The as-fabricated cylindrical components were annealed at 982°C for half an hour in vacuum and after the annealing process they were HIPed at 1163°C at 0.1 GPa for 4 hours in an argon environment.

Inconel 718 is a critical component that is used for turbine engine fabrication because of its high mechanical properties up to $\sim 700^{\circ}\text{C}$, the γ'' -phase is the principal strengthening agent for the material. Vickers (HV) and Rockwell C-scale (HRC) was done on the SLM-fabricated and HIPed cylinders as well as the fabricated and annealed cylinders from the argon and nitrogen build environments. The SLM argon fabricated x-axis cylinder components averaged $\sim 3.9\text{ GPa}$ for the horizontal and the vertical plane while the HIPed component averaged $\sim 5.9\text{ GPa}$, the SLM-fabricated and annealed component averaged at $\sim 4.6\text{ GPa}$. The HRC values for the SLM-fabricated components averaged at 32 HRC while the HIPed samples averaged at 40 HRC. [14]

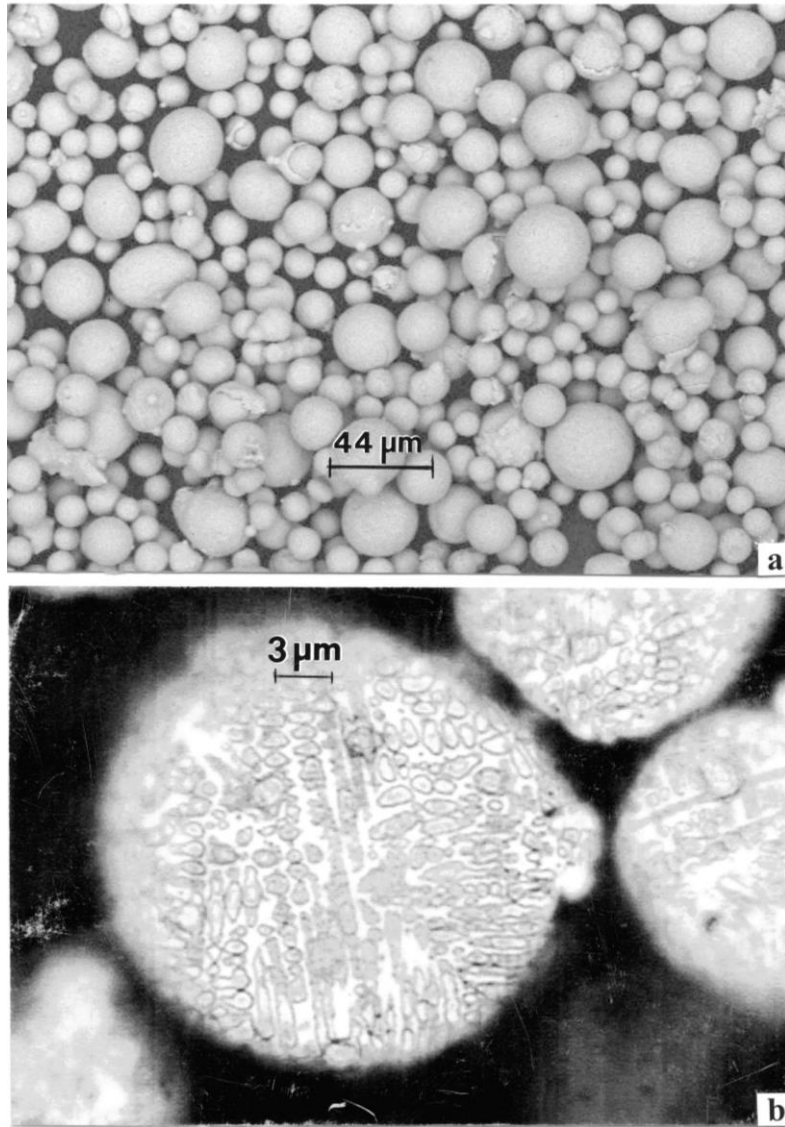


Figure 6.1.1 a) Inconel 718 powder as seen by SEM b) Cross section LOM of etched powder

6.2 MICROSTRUCTURES FOR SLM FABRICATED COMPONENTS BY LOM

Like the 17-4PH, the Inconel 718 microstructures showed the melt pools in the microstructure, figure 6.2.1a shows this structure. The melt pools appear because of the alternating (x-y) melt scans every other layer; this is seen for the vertical plane of the components which are parallel to the build direction; the melt pool width varies from $\sim 75\ \mu\text{m}$ to $100\ \mu\text{m}$ and the layer thickness is about $50\ \mu\text{m}$. It can also be seen in Figure 6.2.1b that the vertical plane has some columnar grains as noted by G, the

arrow with B shows the build direction for the component. Figure 6.2.2 shows a 3D light microscopy image of an etched Inconel 718, fabricated in an argon environment in the x-axis, sample showing a similar columnar microstructure to the one seen in the Co-Cr and in the Inconel 625 samples. Figure 6.2.3 is a cylindrical component manufactured in argon gas and HIPed at 1163°C for 4 hours in 0.1 GPa argon pressure, the component was manufactured in the x-axis; this figure shows a more regular columnar architecture which is spatially identical to the microstructure in figure 6.3.2. The z-axis manufactured component built in argon gas and HIPed, like figure 6.2.3, showed a similar columnar microstructure. Figure 6.2.4 is a vertical plane light microscopy image for a component which was built in a nitrogen gas direction and manufactured in the x-axis; this image shows some recrystallized areas as well as some areas with the columnar microstructure. Figure 6.2.5 is a 3D composite image for an as-fabricated, in nitrogen gas, and HIPed cylindrical component showing columnar microstructure similar to that seen in figure 6.2.3; the component was built in the x-axis. [9, 17]

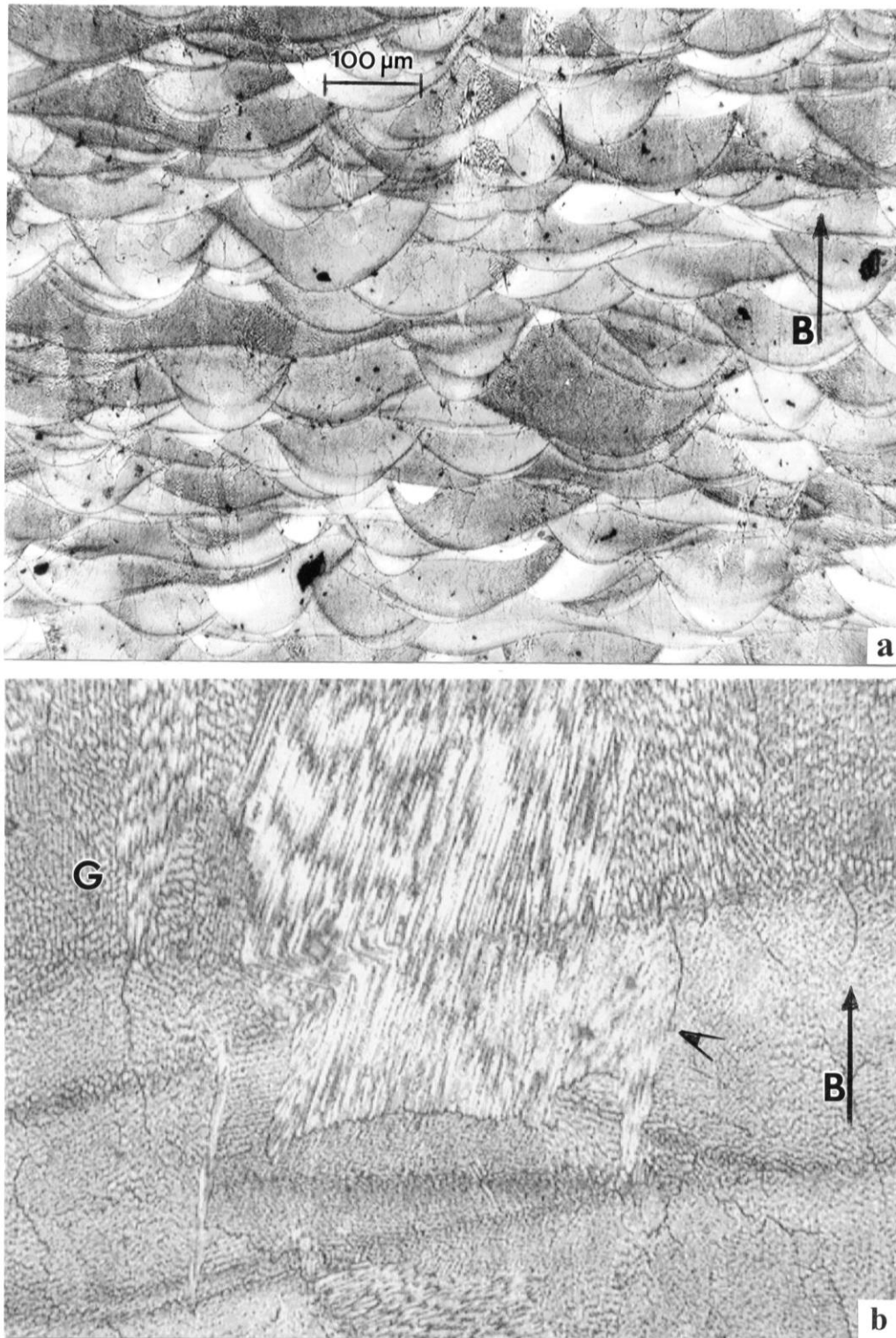


Figure 6.2.1 a) Melt pool feature seen in vertical plane b) columnar grains observed in vertical plane

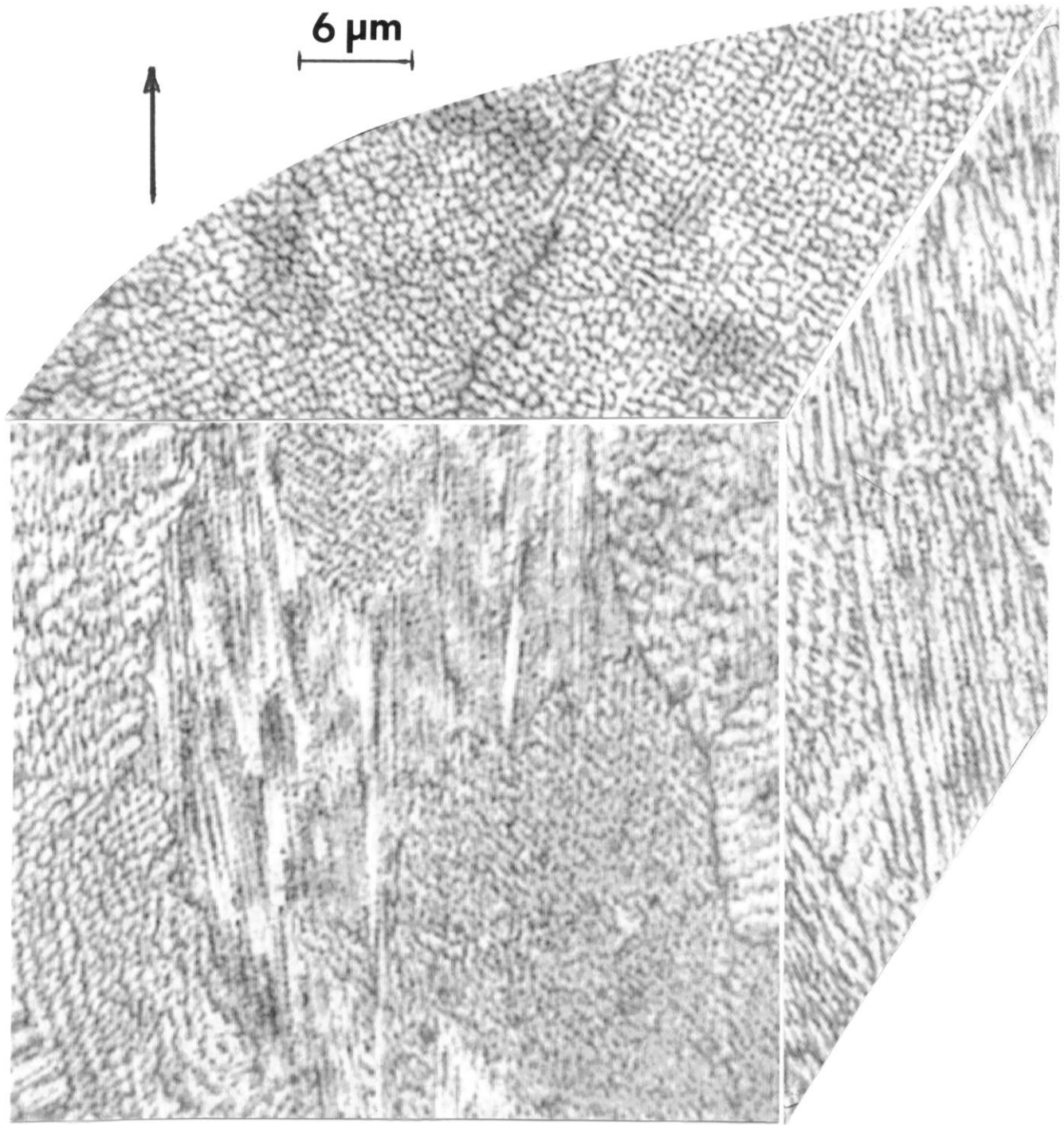


Figure 6.2.2 3D LOM for as-fabricated cylinder in argon (x-axis build)

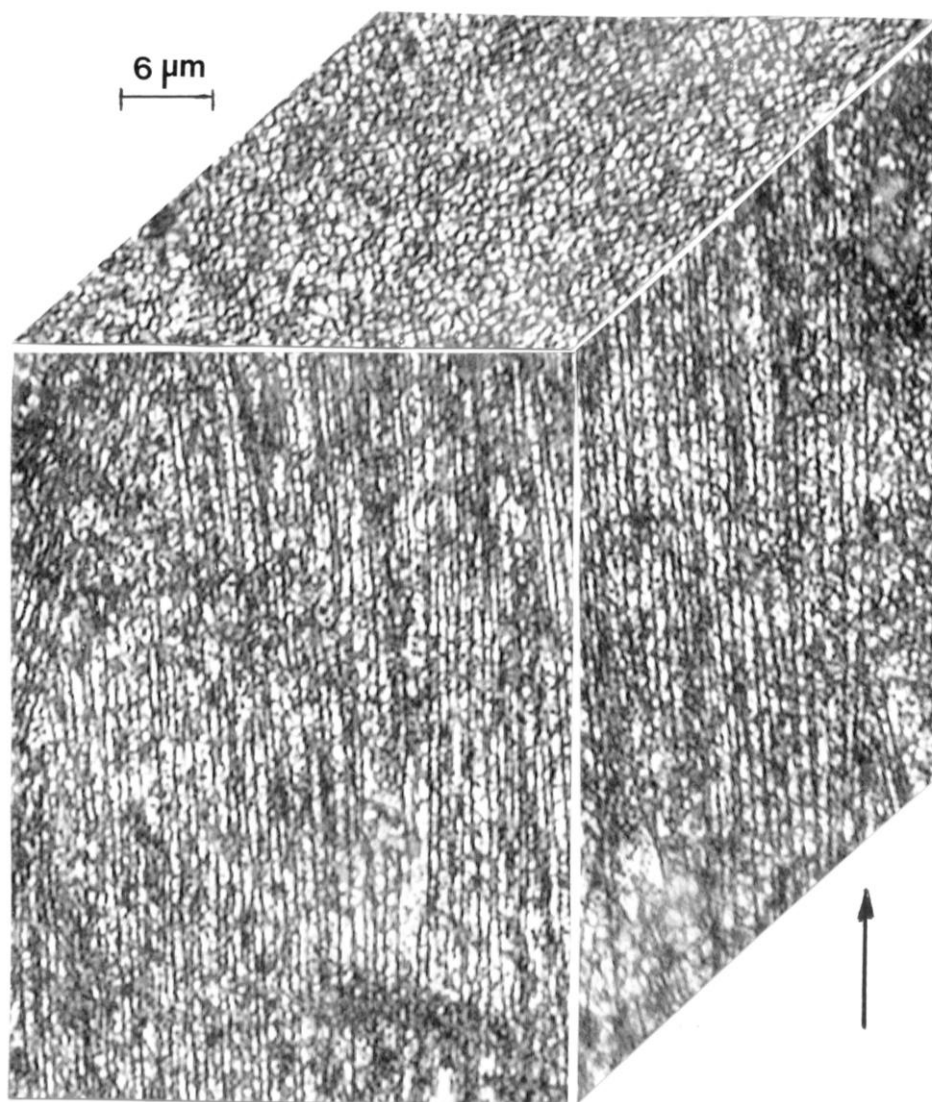


Figure 6.2.3 3D LOM for x-axis component manufactured in argon and HIPed in argon

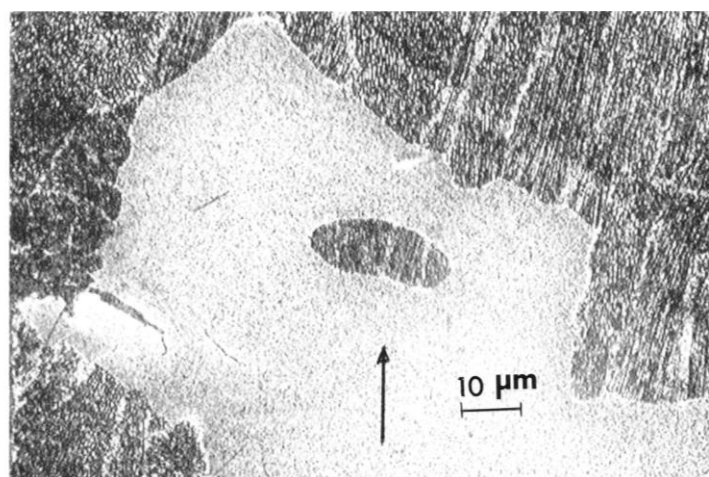


Figure 6.2.4 Vertical plane view for x-axis fabricated component in nitrogen

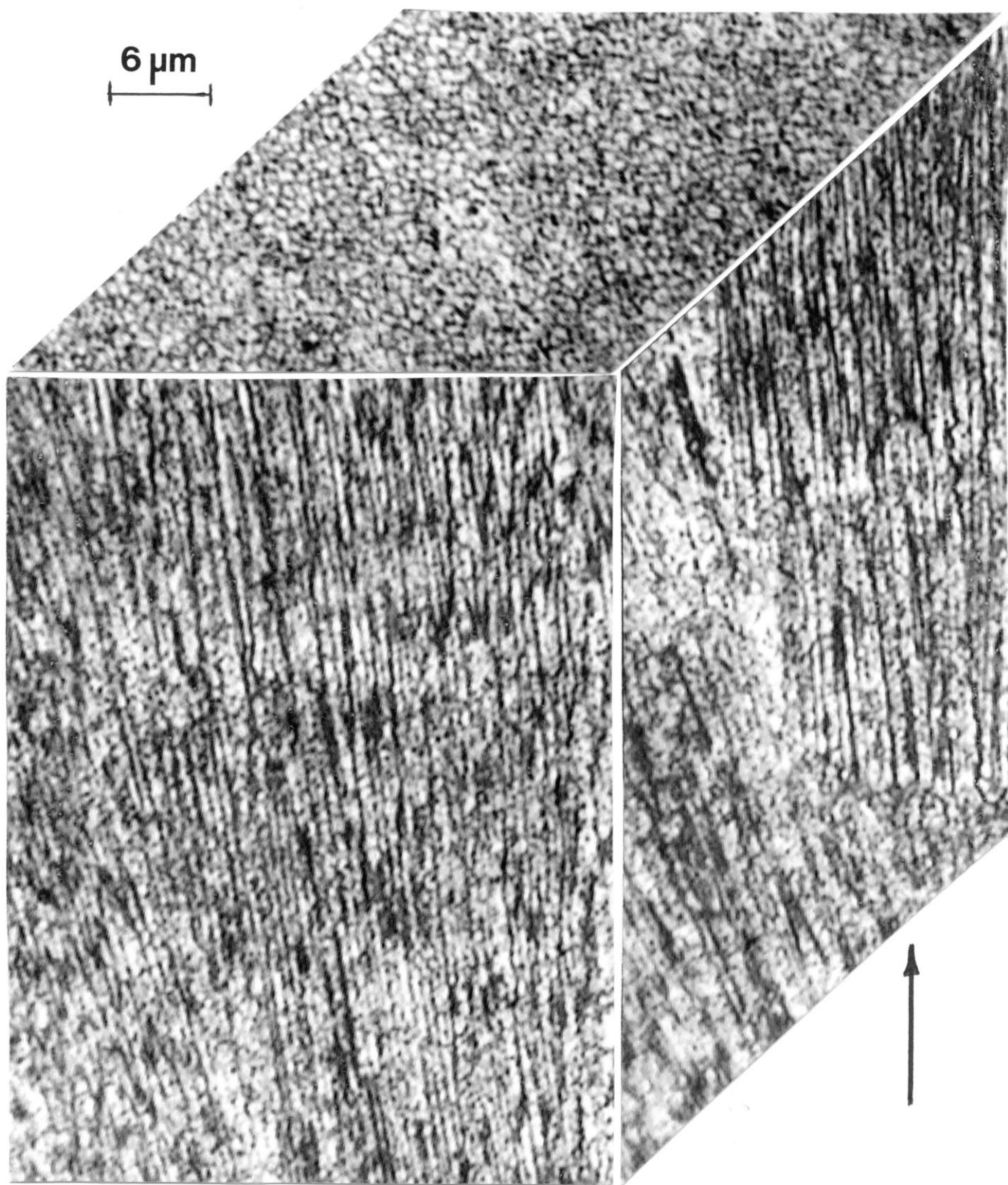


Figure 6.2.5 z-axis manufactured component in argon gas and HIPed

6.3 XRD AND TEM ANALYSIS

Figure 6.3.1 is a comparison of the XRD spectra for the Inconel 718 powder as well as the as-fabricated components for the horizontal and vertical reference planes. The XRD spectra for the powder are coincident with the solid solution γ -fcc NiCr and exhibit prominent (111) texture. On the other hand the XRD spectra for the the as fabricated components in both argon and nitrogen exhibited mixed (111) and (200) texture peaks in the horizontal and vertical reference planes, this was for both the components manufactured in the x-axis as well as in the z-axis.

Specimens for TEM were electropolished using a solution of 200 mL perchloric acid and 800 mL methanol at a temperature $\sim 30^{\circ}\text{C}$ at 13V. Figure 6.3.2 shows a TEM image for the sample that can be seen in figure 6.2.3, this TEM image illustrates the equiaxed grains with spatial dimensions of $0.7\ \mu\text{m}$ in the horizontal plane as well as a variety of dense precipitates within the columnar grains seen in the vertical plane; the diffraction pattern in the figure illustrates the [100] texture. The figure also shows a variety of dense precipitates within the [100] columnar arrays; this image shows particles which are oblate ellipsoidal or spheroidal which can be as large as 250 nm and are immersed in a dense field of γ'' -precipitates less than 10 nm in diameter. The vertical plane, parallel to the build direction, in the image shows arrays of elongated precipitates. Figure 6.3.3 is a magnified view of the vertical plane section of columnar precipitates which shows the precipitates stacked on top of each other and are coincident with the (100) planes, fcc (NiCr) matrix; the elongated precipitates appear to be oblate or spheroids. The SAED insert in the figure shows the γ'' (bct) diffraction spots and streaking of these spots in the [100] direction perpendicular to the major axis of the precipitates. The columnar stacks of the γ'' precipitates are $\sim 250\ \text{nm}$ with a precipitate thickness of $\sim 25\text{-}50\ \text{nm}$ spaced at the same distance. There are also dense and irregular arrangements of various geometries and very small regular sizes of precipitates throughout the NiCr matrix. [14]

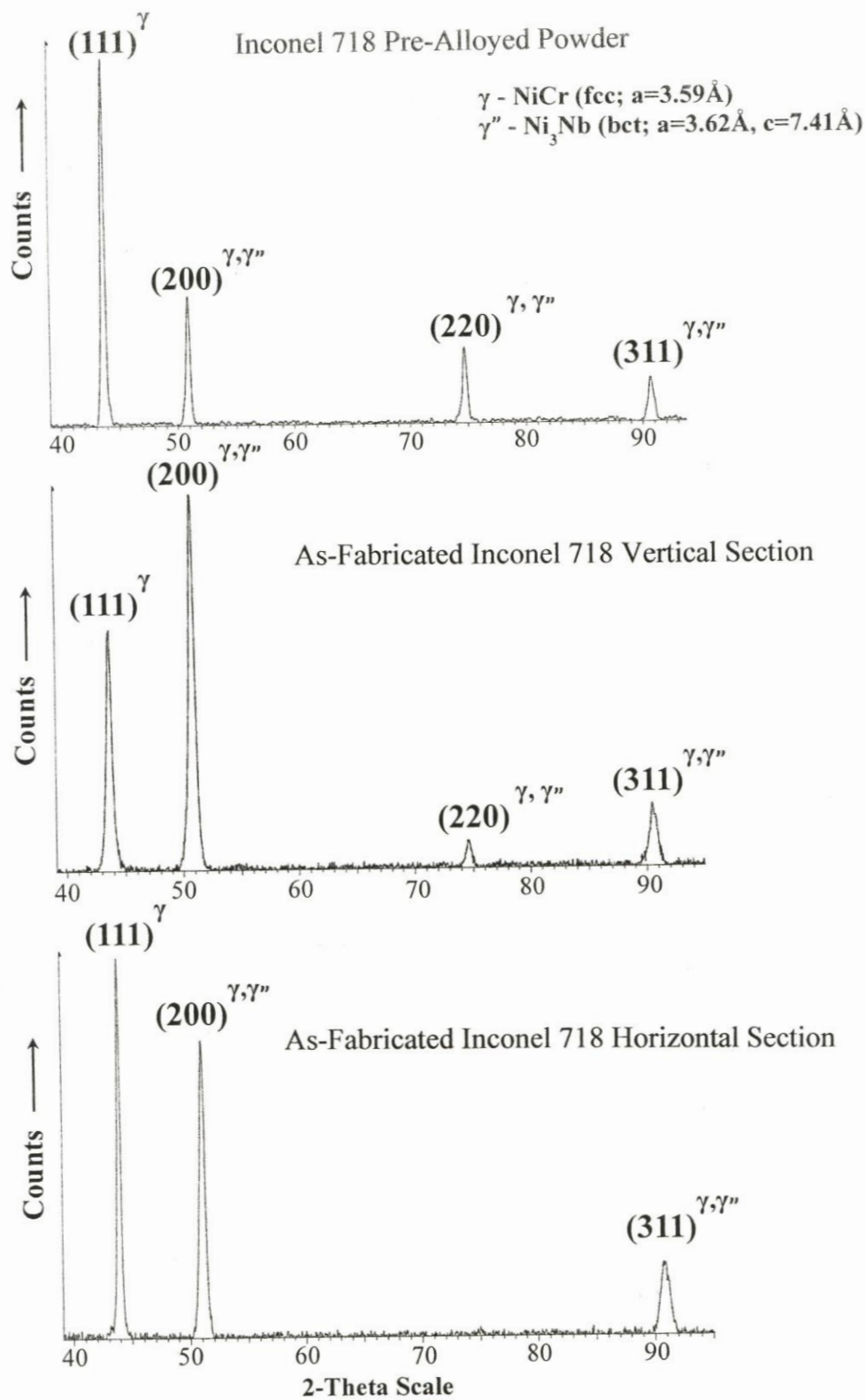


Figure 6.3.1 XRD spectra of powder and as-fab components

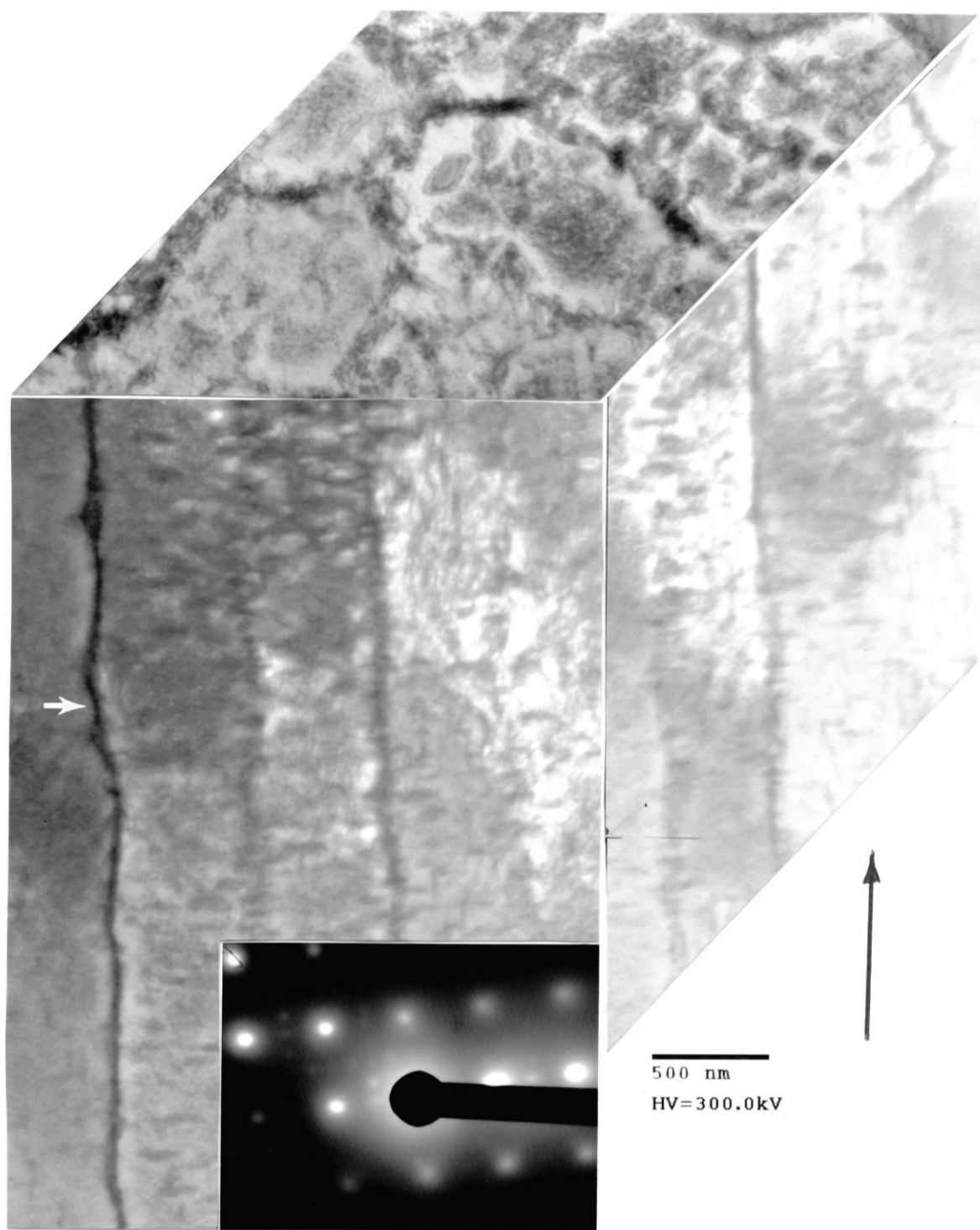


Figure 6.3.2 3D TEM image composite showing dense precipitates

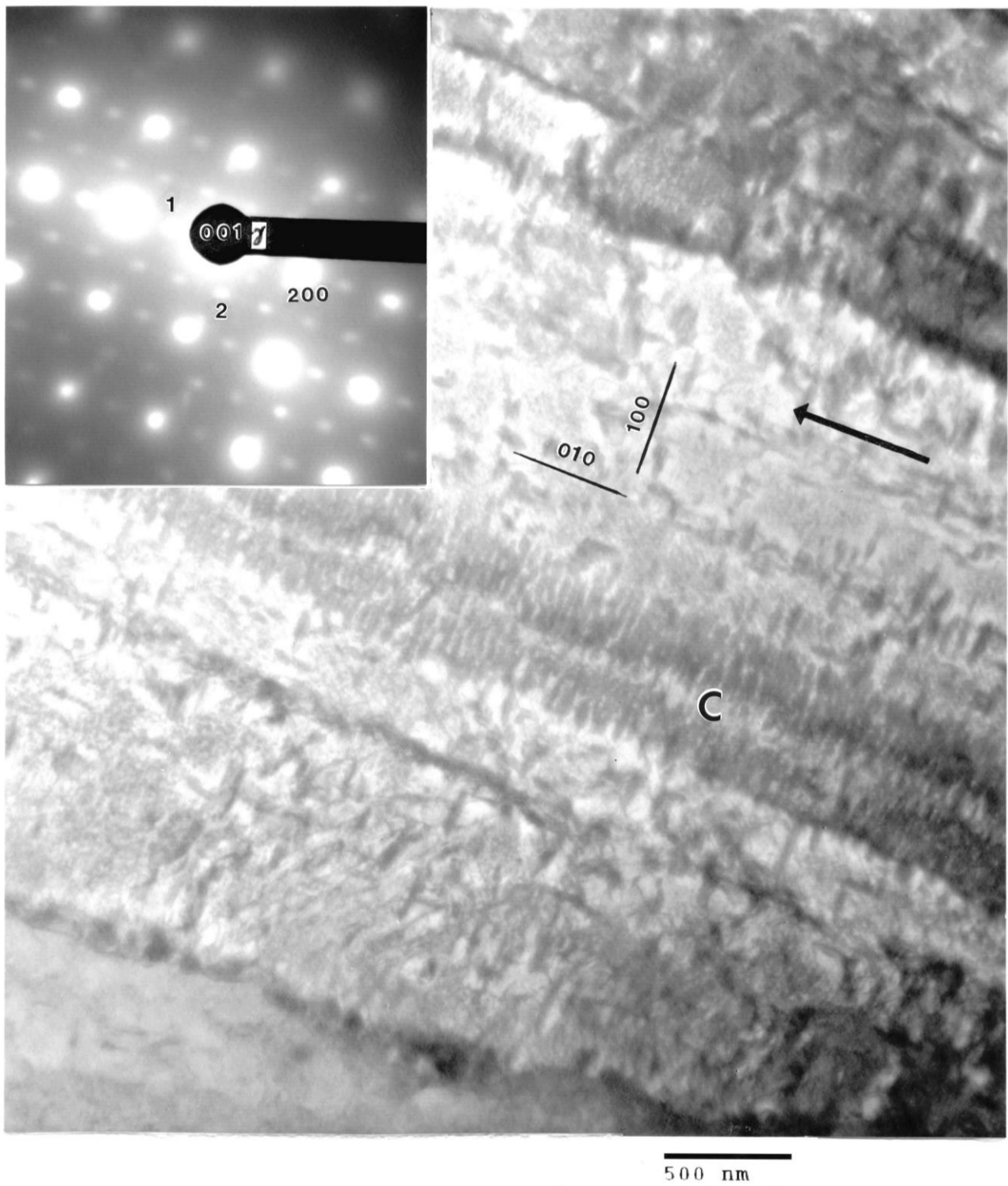


Figure 6.3.3 TEM image for vertical plane section of columnar precipitates

Chapter 7

Conclusion

Additive manufacturing has been a big breakthrough. Not only do we not lose much material but it is possible to create anything that one can dream of as long as one can build it in CAD. The ability to use pre-alloyed gas atomized powders to create metallic components is the next big step in the manufacturing business. Here we have talked about many materials which were manufactured by both EBM and SLM technologies and the columnar microstructure that are created during the manufacturing process. The ability to create and even control the microstructure of material can lead to some innovative technologies which will take full advantage of the columnar microstructures. It is very important for us to understand the microstructures of these materials not only in the macro and micro imaging but by nano imaging as well. Light optical microscopy provided us with an introduction to what to expect during our analysis of our samples; LOM proved to be essential in seen and understanding the similar yet different columnar microstructures. We are still at the infancy of additive manufacturing and many old fundamentals have helped us understand this technology. Many complex, multi-functional, monolithic products of contemporary and alloys are already being realized all over the world. All of the components that we analyzed are already used where high performance and durability are required. The ability to manufacture these alloys by EBM or SLM only opens the door to new applications for the alloys as well as the advantage of having controlled columnar microstructures. Additive manufacturing will indeed be the future of manufacturing.

References

- [1] Porter, David A. 2009 Phase Transformations in Metals and Alloys. 3rd ed. Taylor & Francis Group, LLC
- [2] L. E. Murr, E. Martinez, K. N. Amato, S. M. Gaytan, J. Hernandez, D. A. Ramirez, P. W. Shindo, F. Medina and R. B. Wicker “Fabrication of Metal and Alloy Components by Additive Manufacturing: Examples of 3D Materials Science”, (Review Article), Journal of Materials Research & Technology (Brazil), 2012, Vol. 1 (1), pp. 42-54
- [3] S. M. Gaytan, L. E. Murr, E. Martinez, J. L. Martinez, B. I. Machado, D. A. Ramirez, F. Medina, S. Collins, and R. B. Wicker “Comparison of Microstructures and Mechanical Properties for Solid & Mesh Cobalt-Base Alloy Prototypes Fabricated by Electron Beam Melting”, Metallurgical & Materials Transactions A (2010), Vol. 41A, pp. 3216-3227
- [4] S. M. Gaytan, L. E. Murr, D. A. Ramirez, B. I. Machado, E. Martinez, D. H. Hernandez, J. L. Martinez, F. Medina, R. B. Wicker “A TEM Study of Cobalt-Base Alloy Prototypes with Controlled Microstructural Architecture Fabricated by EBM”, Materials Sciences and Applications, (2011), vol. 2, pp. 355-363
- [5] L. E. Murr, K. N. Amato, S. J. Li, Y. X. Tian, X. Y. Cheng, S. M. Gaytan, E. Martinez, P. W. Shindo, F. Medina, and R. B. Wicker “Microstructure and Mechanical Properties of Open-Cellular Biomaterials Prototypes for Total Knee Replacement Implants Fabricated by Electron Beam Melting”, Journal of the Mechanical Behavior of Biomedical Materials (2011), vol. 4 pp. 1396-1411
- [6] L. E. Murr, Sara M. Gaytan, Edwin Martinez, Frank Medina, and Ryan B. Wicker “Next Generation Orthopedic Implants by Additive Manufacturing Using Electron Beam Melting”, International Journal of Biomaterials, (2012), Article ID245727, 14 pages
- [7] S. M. Gaytan, L. E. Murr, E. Martinez, D. H. Hernandez, J. L. Martinez, F. Medina, R. B. Wicker “A TEM Study of Cobalt-Base Alloy Prototypes with Controlled Microstructural Architecture Fabricated by EBM” Proc. 21st Solid Freeform Fabrication (SFF) Symposium, Austin TX, 2010, CD, p. 27
- [8] E. Martinez, S. M. Gaytan and D. A. Ramirez “Contributions of Light Microscopy to Contemporary Materials Characterization: The New Directional Solidification”, Metallography, Microstructure and Analysis, 2012, vol. 1, pp. 45-58

- [9] S. M. Gaytan, L. E. Murr, D. A. Ramirez, E. Martinez, J. L. Martinez, D. H. Hernandez, B. I. Machado, F. Medina, and R. B. Wicker “Microstructural Architecture Development in Metal and Alloys by Additive Manufacturing Using Electron Beam Melting” Proc. Solid Freeform Fabrication (SFF) conference, Austin, TX, 2010, CD, p. 28
- [10] D. A. Ramirez, L. E. Murr, E. Martinez, D. H. Hernandez, J. L. Martinez, B. I. Machado, F. Medina, R. B. Wicker, and P. Frigola “Novel Precipitate-Microstructural Architecture Developed in the Fabrication of Solid Copper Components by Additive Manufacturing Using Electron Beam Melting” Acta Materialia, (2011), Vol. 59, pp. 4088-4099
- [11] L. E. Murr, E. Martinez, S. M. Gaytan, D. A. Ramirez, B. I. Machado, P.W. Shindo, J. L. Martinez, F. Medina, J. Wooten, D. Ciscel, U. Ackelid, and R. B. Wicker “Microstructural Architecture Microstructures and Mechanical properties for a Nickel-Base Superalloy Fabricated by Electron Beam Melting”, , Metallurgical and Materials Transactions A, 2011, vol. 42A, pp. 3491-3508
- [12] L. E. Murr, E. Martinez, J. Hernandez, S. Collins, K. N. Amato, S. M. Gaytan, and P. W. Shindo “Microstructures and Properties of 17-4 PH Stainless Steel Fabricated by Selective Laser Melting”, Journal of Materials Research & Technology, 2012 vol. 13, pp. 167-177
- [13] E. Martinez, L. E. Murr, K. N. Amato, J. Hernandez, P. W. Shindo, S. M. Gaytan, D. A. Ramirez, F. Medina, R. B. Wicker “3D Microstructural Architecture for Metal and Alloy Components Fabricated by 3D Printing/Additive Manufacturing Technologies”, Proceedings of 1st Int. Conf. on 3D Materials Science 2012, accepted (Ed.) M. De Graff, H. Poulsen, A. Lewis, J. Simmons & G. Spanos, TMS. Warrendale, PA, CD, pp. 73-78
- [14] K. N. Amato, L. E. Murr, S. M. Gaytan, E. Martinez, P. W. Shindo, J. Hernandez, S. Collins and F. Medina “Microstructures and Mechanical Behavior for Inconel 718 Fabricated by Selective Laser Melting”, Acta Materialia, (2012), vol. 60, pp. 2229-2239
- [15] K. N. Amato, J. Hernandez, E. Martinez, L. E. Murr, S. M. Gaytan, P. W. Shindo, and S. Collins “Comparison of Microstructures and Properties for a Ni-Base Superalloy (Alloy 625) Fabricated by Electron and Laser Beam Melting”, Journal of Materials Science Research, (2012) Vol. 1 (2) (April), pp. 3-41
- [16] J. Hernandez, K. N. Amato, E. Martinez, P. W. Shindo, C. A. Terrazas, E. Rodriguez, F. Medina, R. B. Wicker, S. J. Li, and X. Y. Cheng “Microstructures and Properties for a Superalloy Powder Mixture Processed by Electron Beam Melting”, Journal of Materials Science Research, (2012), Vol. 1 (3), pp. 124-144
- [17] L. E. Murr, S. J. Li, Y. X. Tian, K. N. Amato, E. Martinez, and F. Medina “Open-Cellular Co-Base and Ni-Base Superalloys Fabricated by Electron Beam Melting”, Materials (2011), vol. 4, pp. 782-790

[18] D. A. Ramirez, L. E. Murr, S. J. Li, Y. Tian, E. Martinez, J. L. Martinez, B. I. Machado, S. M. Gaytan, F. Medina, R. B. Wicker “Open-Cellular Copper Structures Fabricated by Additive Manufacturing Using Electron Beam Melting”, Materials Science and Engineering A, (2011), vol. 528A, pp. 5379-5386

Appendix

E. Martinez, S. M. Gaytan and D. A. Ramirez “Contributions of Light Microscopy to Contemporary Materials Characterization: The New Directional Solidification”, Metallography, Microstructure and Analysis, 2012, vol. 1, pp. 45-58

K. N. Amato, J. Hernandez, E. Martinez, L. E. Murr, S. M. Gaytan, P. W. Shindo, and S. Collins “Comparison of Microstructures and Properties for a Ni-Base Superalloy (Alloy 625) Fabricated by Electron and Laser Beam Melting”, Journal of Materials Science Research, (2012) Vol. 1 (2) (April), pp. 3-41

S. M. Gaytan, L. E. Murr, D. A. Ramirez, B. I. Machado, E. Martinez, D. H. Hernandez, J. L. Martinez, F. Medina, R. B. Wicker “A TEM Study of Cobalt-Base Alloy Prototypes with Controlled Microstructural Architecture Fabricated by EBM”, Materials Sciences and Applications, (2011), vol. 2, pp. 355-363

L. E. Murr, E. Martinez, J. Hernandez, S. Collins, K. N. Amato, S. M. Gaytan, and P. W. Shindo “Microstructures and Properties of 17-4 PH Stainless Steel Fabricated by Selective Laser Melting”, Journal of Materials Research & Technology, 2012 vol. 13, pp. 167-177

D. A. Ramirez, L. E. Murr, E. Martinez, D. H. Hernandez, J. L. Martinez, B. I. Machado, F. Medina, R. B. Wicker, and P. Frigola “Novel Precipitate-Microstructural Architecture Developed in the Fabrication of Solid Copper Components by Additive Manufacturing Using Electron Beam Melting” Acta Materialia, (2011), Vol. 59, pp. 4088-4099

K. N. Amato, L. E. Murr, S. M. Gaytan, E. Martinez, P. W. Shindo, J. Hernandez, S. Collins and F. Medina “Microstructures and Mechanical Behavior for Inconel 718 Fabricated by Selective Laser Melting”, Acta Materialia, (2012), vol. 60, pp. 2229-2239

Publications

“Microstructures and Mechanical Properties of Electron Beam-Rapid Manufactured Ti-6Al-4V Biomedical Prototypes Compared to Wrought Ti-6Al-4V”, L. E. Murr, E. V. Esquivel, S. A. Quiñones, S. M. Gaytan, M. I. Lopez, E. Y. Martinez, F. Medina, D. H. Hernandez, E. Martinez, J. L. Martinez, S. W. Stafford, D. K. Brown, T. Hoppe, W. Meyers, R. B. Wicker, and U. Lindhe, Materials Characterization, 2009, vol. 60 oo. 96-105

“Microstructure and Mechanical Behavior of Ti-6Al-4V for Biomedical Applications Produced by Rapid-Layer Manufacturing”, L.E. Murr, S. A. Quiñones, S. M. Gaytan, M. I. Lopez, A. Rodela, E. Y. Martinez, D. H. Hernandez, E. Martinez, F. Medina, R. B. Wicker, Review article, Journal of the Mechanical Behavior of Biomedical Materials, 2009, vol. 2, pp. 20-32

“Properties and Microstructures of Electron Beam-Rapid Manufactured Ti-6Al-4V Biomedical Prototypes Compared to Wrought Ti-6Al-4V”, L. E. Murr, S. M. Gaytan, M. I. Lopez, E. Y. Martinez, D. H. Hernandez, E. Martinez, J. L. Martinez, Biomedical Engineering: Recent Developments, H. Nazeran, M. Goldman and R. Schoepfoerster (Eds.), Medical and Engineering Publishers, Inc., MD 2008, pp. 225-228

“Comparison of Microstructure and Mechanical Behavior of Ti-6Al-4V for Biomedical Applications Produced by Rapid-Layer-Based Manufacturing” E. Y. Martinez, L. E. Murr, S. M. Gaytan, M. I. Lopez, A. Rodela, D. H. Hernandez, and E. Martinez Biomedical Engineering: Recent Developments .), Medical and Engineering Publishers, Inc., MD 2008, pp. 229-232

“Microstructural and Mechanical Properties of Ti-6Al-4V for Biomedical and Related Applications Involving Rapid Layer Powder Manufacturing”, L. E. Murr, S. M. Gaytan, S. A. Quiñones, M. I. Lopez, A. Rodela, E. Y. Martinez, D. H. Hernandez, E. Martinez, D. A. Ramirez, F. Medina, R. B. Wicker, MS&T 2008 Ceramic Transactions: Advances in Biomedical and Biomimetic Materials: Ceramic Transactions, R. J. Narayan, P. N. Kumta and W. R. Wagner (eds) Amer. Ceram. Soc., Vol. 206 (july, 2009), pp. 71-83

“Structure-Property-Process Optimization in the Rapid-Layer Manufacturing of Ti-6Al-4V Components by Electron Beam Melting”, L. E. Murr, S. M. Gaytan, D. H. Hernandez, E. Martinez, S. A. Quiñones, F. Medina and R. B. Wicker, Collected Proceedings: Materials Issues in Additive Powder-Based Manufacturing, Supplemental Proceedings: Volume I: Fabrication, Materials, Processing and Properties, TMS-2009 (CD); pp. 363-369

“Microstructure Evolution Associated with Adiabatic Shear Bands and Shear Band Failure in Ballistic Plug Formation in Ti-6Al-4V Targets”, L. E. Murr, A. C. Ramirez, S. M. Gaytan, M. I. Lopez, E. Y. Martinez, D. H. Hernandez, E. Martinez, Materials Science and Engineering A, 2009, Vol. 516, pp. 205-216

“Additive Layered Manufacturing of Reticulated Ti-6Al-4V Biomedical Mesh Structures by Electron Beam Melting”, S. M. Gaytan, L. E. Murr, F. Medina, M. I. Lopez, E. Martinez, R. B. Wicker, A.

Mcgoran, C. Li and W-C. Lih (eds.) 25th Southern Biomedical Engineering Conf, International Federation of Medical and Biological Engineering Proceedings, 2009, 24 (CD), pp. 23-28

“Metallographic Characterization of Additive-Layer Manufactured Products by Electron Beam Melting of Ti-6Al-4V Powder”, L.E. Murr, S. M. Gaytan, M. I. Lopez, E. Martinez, F. Medina, R. B. Wicker, Practical Metallography, 2009, vol. XLVI (September), pp. 442-453

“Advanced Metal Powder-Based Manufacturing of Complex Components by Electron Beam Melting”, L. E. Murr, S. M. Gaytan, F. Medina, E. Martinez, M. I. Lopez, and R. B. Wicker, Materials Technology: Advanced Performance Materials, (2009) Vol. 24, No. 3, pp. 180-190

“Next Generation Biomedical Implants Using Additive Layered Manufacturing of Complex, Cellular and Functional Mesh Arrays”, L. E. Murr, S. M. Gaytan, F. Medina, H. Lopez, E. Martinez, D. H. Hernandez, J. L. Martinez, M. I. Lopez, R. B. Wicker and J. Bracke, Philosophical Transactions (Royal Society, London) A, 2010, vol. 368, pp. 1999-2032

“Effect of Build Parameters and Build Geometries on Residual Microstructures and Mechanical Properties of Ti-6Al-4V Components Built by Electron Beam Melting”, S. M. Gaytan, L. E. Murr, F. Medina, E. Martinez, D. H. Hernandez, M. I. Lopez, R. B. Wicker and S. Collins, Proc. Solid Free Form Conference, Austin, TX 2009, CD, pp. 347-397

“Characterization of Ti-6Al-4V Open Cellular Foams Fabricated by Additive Manufacturing Using Electron Beam Melting”, L. E. Murr, S. M. Gaytan, F. Medina, E. Martinez, J. L. Martinez, D. H. Hernandez, B. I. Machado, D. A. Ramirez, and R. B. Wicker, Materials Science and Engineering A, 2010, vol. A527, pp. 1861-1868

“Characterization of Titanium Aluminide Alloy Components Fabricated by Additive Manufacturing Using Electron Beam Melting”, L. E. Murr, S. M. Gaytan, A. Ceylan, E. Martinez, J. L. Martinez, D. H. Hernandez, B. I. Machado, D. A. Ramirez, F. Medina, S. Collins, and R. B. Wicker, Acta Materialia, 2010, vol. 58, pp. 1887-1894

“Fabrication and Characterization of Reticulated, Porous Mesh Arrays and Foams for Aerospace Applications by Additive Manufacturing using Electron Beam Melting”, L. E. Murr, S. M. Gaytan, F. Medina, E. Martinez, J. L. Martinez, and R. B. Wicker, Global Innovations in Manufacturing of Aerospace Materials, Proceedings of 11th MPMD (TMS) Global Innovations Symposium, Supplemental Proceedings: Volume 1: Materials Processing and Properties, TMS (The Minerals, Metals and Materials Society), 2010 pp. 283-290

“Additive Manufacturing of Complex Mesh and Foam Arrays for Next Generation Biomedical Implants”, L. E. Murr, S. M. Gaytan, F. Medina, E. Martinez, B. I. Machado, D. H. Hernandez, J. L. Martinez, M. I. Lopez, and R. B. Wicker, Proceedings of American Chemical Society (ACS) Southwest/Mexico-Japan-US Materials Consortium (2010)

“Comparison of Microstructures and Mechanical Properties for Solid & Mesh Cobalt-Base Alloy Prototypes Fabricated by Electron Beam Melting” S. M. Gaytan, L. E. Murr, E. Martinez, J. L.

Martinez, B. I. Machado, D. A. Ramirez, F. Medina, S. Collins, and R. B. Wicker, Metallurgical & Materials Transactions A (2010), Vol. 41A, pp. 3216-3227

“A TEM Study of Cobalt-Base Alloy Prototypes with Controlled Microstructural Architecture Fabricated by EBM” S. M. Gaytan, L. E. Murr, D. A. Ramirez, B. I. Machado, E. Martinez, D. H. Hernandez, J. L. Martinez, F. Medina, R. B. Wicker, Materials Sciences and Applications, (2011), vol. 2, pp. 355-363

“Novel Precipitate-Microstructural Architecture Developed in the Fabrication of Solid Copper Components by Additive Manufacturing Using Electron Beam Melting” D. A. Ramirez, L. E. Murr, E. Martinez, D. H. Hernandez, J. L. Martinez, B. I. Machado, F. Medina, R. B. Wicker, and P. Frigola; Acta Materialia, (2011), Vol. 59, pp. 4088-4099

“Microstructural Architecture Development in Metal and Alloys by Additive Manufacturing Using Electron Beam Melting”, S. M. Gaytan, L. E. Murr, D. A. Ramirez, E. Martinez, J. L. Martinez, D. H. Hernandez, B. I. Machado, F. Medina, and R. B. Wicker, Proc. Solid Freeform Fabrication (SFF) conference, Austin, TX, 2010, CD, p. 28

“A TEM Study of Cobalt-Base Alloy Prototypes with Controlled Microstructural Architecture Fabricated by EBM” S. M. Gaytan, L. E. Murr, E. Martinez, D. H. Hernandez, J. L. Martinez, F. Medina, R. B. Wicker, Proc. 21st Solid Freeform Fabrication (SFF) Symposium, Austin TX, 2010, CD, p. 27

“Optimization of Shear Strengths of Ultrasonically Consolidated Ti/Al 3003 Dual-Material Structures”, with John Obielodan, Brent Stucker, E. Martinez, J. L. Martinez, D. H. Hernandez, D. A. Ramirez, L. E. Murr, Journal of Materials Processing Technology, (2011) vol. 211, pp. 988-995

“Open-Cellular Copper Structures Fabricated by Additive Manufacturing Using Electron Beam Melting” D. A. Ramirez, L. E. Murr, S. J. Li, Y. Tian, E. Martinez, J. L. Martinez, B. I. Machado, S. M. Gaytan, F. Medina, R. B. Wicker, Materials Science and Engineering A, (2011), vol. 528A, pp. 5379-5386

“Microstructural Architecture Microstructures and Mechanical properties for a Nickel-Base Superalloy Fabricated by Electron Beam Melting”, L. E. Murr, E. Martinez, S. M. Gaytan, D. A. Ramirez, B. I. Machado, P.W. Shindo, J. L. Martinez, F. Medina, J. Wooten, D. Ciscel, U. Ackelid, and R. B. Wicker, Metallurgical and Materials Transactions A, 2011, vol. 42A, pp. 3491-3508

“Next Generation Orthopedic Implants by Additive Manufacturing Using Electron Beam Melting”, L. E. Murr, Sara M. Gaytan, Edwin Martinez, Frank Medina, and Ryan B. Wicker, International Journal of Biomaterials, (2012), Article ID245727, 14 pages

“Microstructure and Mechanical Properties of Open-Cellular Biomaterials Prototypes for Total Knee Replacement Implants Fabricated by Electron Beam Melting”, L. E. Murr, K. N. Amato, S. J. Li, Y. X. Tian, X. Y. Cheng, S. M. Gaytan, E. Martinez, P. W. Shindo, F. Medina, and R. B. Wicker, Journal of the Mechanical Behavior of Biomedical Materials (2011), vol. 4 pp. 1396-1411

“Open-Cellular Co-Base and Ni-Base Superalloys Fabricated by Electron Beam Melting”, L. E. Murr, S. J. Li, Y. X. Tian, K. N. Amato, E. Martinez, and F. Medina, Materials (2011), vol. 4, pp. 782-790

“Contributions of Light Microscopy to Contemporary Materials Characterization: The New Directional Solidification”, E. Martinez, S. M. Gaytan and D. A. Ramirez, Metallography, Microstructure and Analysis, 2012, vol. 1, pp. 45-58

“Materials Characterization of Railgun Erosion Phenomena”, B. I. Machado, L. E. Murr, E. Martinez, S. A. Gaytan and S. Sataphathy, Materials Science & Engineering A (2011), vol. 528 (25-26), pp. 7552-7559

“Evaluation of Titanium Alloy Dental Prototypes Fabricated Using Rapid Prototyping Technologies Electron Beam Melting & Laser Beam Melting”, M. Koike, P. Green, K. Owen, L. Guo, S. M. Gaytan, E. Martinez, L. E. Murr, and T. Okabe,

“Evaluation of Titanium Alloy Dental Prototypes Fabricated Using Rapid Prototyping Technologies Electron Beam Melting & Laser Beam Melting”, M. Koike, P. Green, K. Owen, L. Guo, S. M. Gaytan, E. Martinez, L. E. Murr, and T. Okabe, Materials, 2011, Vol. 4, pp. 1776-1792

“Microstructures and Mechanical Behavior for Inconel 718 Fabricated by Selective Laser Melting”, K. N. Amato, L. E. Murr, S. M. Gaytan, E. Martinez, P. W. Shindo, J. Hernandez, S. Collins and F. Medina, Acta Materialia, (2012), vol. 60, pp. 2229-2239

“Microstructures for Two-Phase Gamma Titanium Aluminide Fabricated by Electron Beam Melting”, J. Hernandez, L. E. Murr, S. M. Gaytan, E. Martinez, F. Medina, and R.B. Wicker, Metallography, Microstructure and Analysis, (2012) vol. 1, pp. 14-27

“Metal Fabrication by Additive Manufacturing Using Laser and Electron Beam Melting Technologies”, L. E. Murr, S. M. Gaytan, D. A. Ramirez, E. Martinez, J. Hernandez, K. N. Amato, P. W. Shindo, F. Median, R. B. Wicker, (Invited Review): Journal of Materials Science & Technology, (2012) Vol. 28 (1), pp. 1-14

Microstructures and Properties of 17-4 PH Stainless Steel Fabricated by Selective Laser Melting”, L. E. Murr, E. Martinez, J. Hernandez, S. Collins, K. N. Amato, S. M. Gaytan, and P. W. Shindo, Journal of Materials Research & Technology, 2012 vol. 13, pp. 167-177

“Fabricating Functional Ti-Alloy Biomedical Implants by Additive Manufacturing Using Electron Beam Melting”, L. E. Murr, S. M. Gaytan, E. Martinez, F. Medina, and R. B. Wicker, Review; Journal of Biotechnology & Biomaterials, 2012, Vol. 2 (3), 11 pages

“3D Microstructural Architecture for Metal and Alloy Components Fabricated by 3D Printing/Additive Manufacturing Technologies”, E. Martinez, L. E. Murr, K. N. Amato, J. Hernandez, P. W. Shindo, S. M. Gaytan, D. A. Ramirez, F. Medina, R. B. Wicker, Proceedings of 1st Int. Conf. on 3D Materials Science 2012, accepted (Ed.) M. De Graff, H. Poulsen, A. Lewis, J. Simmons & G. Spanos, TMS. Warrendale, PA, CD, pp. 73-78

- “Effect of Melt Scan Rate on Microstructure and Macrostructure for Electron Beam Melting of Ti-6Al-4V”, K. Puebla, S. M. Gaytan, E. Martinez, L. E. Murr, F. Medina, R. B. Wicker, Materials Sciences and Applications, 2012, Vol. 3, pp. 259-264
- “Comparison of Microstructures and Properties for a Ni-Base Superalloy (Alloy 625) Fabricated by Electron and Laser Beam Melting”, K. N. Amato, J. Hernandez, E. Martinez, L. E. Murr, S. M. Gaytan, P. W. Shindo, and S. Collins, Journal of Materials Science Research, (2012) Vol. 1 (2) (April), pp. 3-41
- “Fabrication of Metal and Alloy Components by Additive Manufacturing: Examples of 3D Materials Science”, (Review Article) L. E. Murr, E. Martinez, K. N. Amato, S. M. Gaytan, J. Hernandez, D. A. Ramirez, P. W. Shindo, F. Medina and R. B. Wicker, Journal of Materials Research & Technology (Brazil), 2012, Vol. 1 (1), pp. 42-54
- “Microstructures and Properties for a Superalloy Powder Mixture Processed by Electron Beam Melting”, J. Hernandez, K. N. Amato, E. Martinez, P. W. Shindo, C. A. Terrazas, E. Rodriguez, F. Medina, R. B. Wicker, S. J. Li, and X. Y. Cheng, Journal of Materials Science Research, (2012), Vol. 1 (3), pp. 124-144

Presentations

Paper presented at 24th Southern Biomedical Engineering Conference, April, 19, 20, 2008, University of Texas at El Paso: “Comparison of Microstructure and Mechanical Behavior of Ti-6Al-4V for Biomedical Applications Produced by Rapid-Layer Based Manufacturing”, E. Martinez, L. E. Murr, S. Gaytan, M. I. Lopez, A. Rodela, D. Hernandez

Poster presentation at 19th Solid Freeform Fabrication Symposium University of Texas at Austin, TX, August 4-6, 2008: “Microstructural and Detect Analysis and Control of Ti-6Al-4V Components Manufactured by Electron Beam Melting”, Sara Gaytan, Lawrence Murr, Edwin Martinez, Daniel Hernandez, Stella Quiñones, Francisco Medina, Ryan Wicker.

Invited Paper “Microstructure and Mechanical Behavior of Ti-6Al-4V for Biomedical Applications Produced by Rapid-Layer-Based Manufacturing”, L. E. Murr, S. A. Quiñones, S. M. Gaytan, M. I. Lopez, A. Rodela, E. Y. Martinez, D. H. Hernandez, E. Martinez, D.A. Ramirez, F. Medina, and R. B. Wicker, Materials Science & Technology 2008 Conference & Exhibit (MS&T 2008): Symposium on Materials & Systems; Advances in Biomedical and Biomimetic Materials, Pittsburgh, PA, Oct 6-8, 2008

Papers presented at 138th Annual TMS (The Minerals, Metals & Materials Society) Conference & Exhibition, February 15-18, 2009, San Francisco, CA

- a.) “Structure-Property-Process Optimization in the Rapid-Layer Manufacturing of Ti-6Al-4V Components by Electron Beam Melting”, S. M. Gaytan, L.E. Murr, D.H. Hernandez, E. Martinez, S.A Quiñones, F. Medina, and R.B. Wicker
- b.) “Characterization of Deformation Bands, Adiabatic Shear Bands, and Crack Formation and Propagation in Ti-6Al-4V Ballistic Plug Targets” (Invited) L.E. Murr, A. C. Ramirez, S. M. Gaytan, M.I. Lopez, E. Y. Martinez, D. H. Hernandez, E. Martinez

Paper presented at 25th Southern Biomedical Conference, May 15-17, 2009, Florida International University, Miami, FL. L.E. Murr, S.M. Gaytan, F. Medina, M.I. Lopez, E. Martinez, R.B. Wicker, “Additive Layered Manufacturing of Reticulated Ti-6Al-4V Biomedical Mesh Structures by Electron Beam Melting”

Paper presented at 20th Annual Advanced Aerospace Materials and Processes Conference & Exhibition (AeroMat 2009), June 7-11, 2009, Dayton OH: “Advanced Powder Based Aerospace Manufacturing Concepts: Building Specialized, Complex Component Geometries Utilizing Electron Beam Melting of Ti-6Al-4V”, S.M. Gaytan, L.E. Murr, M.I. Lopez, E. Martinez, F. Medina, R.B. Wicker

Papers presented at Materials Science and Technology 2009 Conference & Exhibition (MS&T 09), October 25-29, Pittsburgh, PA: “Next Generation Biomedical Implants Using Additive Manufacturing of Complex, Functional Mesh Arrays” (Invited), L.E. Murr, S.M. Gaytan, F. Medina, H. Lopez, E. Martinez, D.H. Hernandez, L. Martinez, M.I. Lopez, R.B. Wicker

Paper presented at 65th Southwest Regional Meeting- American Chemical Society: USA-Mexico-Japan Materials Consortium Symposium. Nov. 8-10, 2009, El Paso, TX: “Next Generation Biomedical

Implants Using Additive Manufacturing of Complex, Cellular and Functional Mesh Arrays” L.E. Murr (Invited) S. M. Gaytan, F. Medina, H. Lopez, E. Martinez, B.I. Machado, D.H. Hernandez, L. Martinez, M.I. Lopez, R.B. Wicker, J. Bracke

Paper presented at 139th Annual TMS (The Minerals, Metals & Materials Society) Conference and Exhibition, February 14-18, 2010, Seattle WA

- a.) “Fabrication & Characterization of Reticulated, Porous Mesh Arrays and Foams for Aerospace Applications by Additive Manufacturing using Electron Beam Melting”, S.M. Gaytan, L.E. Murr, F. Medina, E. Martinez, L. Martinez, and R.B. Wicker
- b.) “Fabrication of Ti-6Al-4V Open cellular foams by Additive Manufacturing Using Electron Beam Melting”, L.E. Murr, S.M. Gaytan, F. Medina, E. Martinez, L. Martinez, R.B. Wicker

Papers presented at 21st International Solid Freeform Fabrication Symposium, August 8-11, 2010 Austin, TX

- a.) “Comparison of Microstructures and Mechanical Properties for Solid and Mesh Cobalt Base Alloy components and Biomedical Implant Prototypes Fabricated by Electron Beam Melting”, S.M. Gaytan, L.E. Murr, E. Martinez, J.L. Martinez, B.I. Machado, D.A. Ramirez, F. Medina, S. Collins, R.B. Wicker
- b.) “A TEM Study of Cobalt base Alloy Prototypes with Controlled Microstructural Architecture Fabricated by EBM” (Poster) S.M. Gaytan, L.E. Murr, E. Martinez, J. Martinez, D. H. Hernandez, F. Medina, R. Wicker
- c.) “Comparison of Microstructures and Mechanical Properties for Solid and mesh Cobalt-Base Alloy Prototypes Fabricated by Electron Beam Melting” (Poster) E. Martinez, S.M. Gaytan, B.I. Machado, L.E. Murr, J.L. Martinez, D.A. Ramirez, F. Medina, R.B. Wicker, S. Collins
- d.) “Copper Monoliths and Low Density Mesh and Foam Components Fabricated by Additive Manufacturing Using Electron Beam Melting” (Poster) D.A. Ramirez, L.E. Murr, F. Medina, E. Martinez, J.L. Martinez, D.H. Hernandez, R.B. Wicker, P. Frigola

Papers presented at Materials Science and Technology 2010 Conference & Exhibition (MS&T 2010), October 17-21, 2010 Houston, TX

- a.) “Characterization of Copper Open Cellular Structures Fabricated by Electron Beam Melting” D.A. Ramirez, L.E. Murr, S.J. Li, E. Martinez, D.H. Hernandez, J.L. Martinez, F. Medina, P. Frigola, R. B. Wicker
- b.) “Comparison of Microstructures and Mechanical Properties for Solid and Mesh Cobalt-Base Alloy Prototypes Fabricated by Electron Beam Melting” (Poster) E. Martinez, S.M. Gaytan, B.I. Machado, L.E. Murr, J.L. Martinez, D.A. Ramirez, F. Medina, R.B. Wicker, S. Collins
- c.) “Comparison of Microstructures and Mechanical Properties for Solid and Mesh Cobalt-Base Alloy Components and Biomedical Implant Prototypes Fabricated by Electron Beam Melting”, S. M. Gaytan, L.E. Murr, E. Martinez, J. Martinez, B.I. Machado, D.A. Ramirez, F. Medina, S. Collins, R.B. Wicker

- d.) “A TEM Study of Cobalt-Base Alloy Prototypes with Controlled Microstructural Architecture Fabricated by EBM” (poster) S. M. Gaytan, L.E. Murr, E. Martinez, J.L. Martinez, D. H. Hernandez, F. Medina, R.B. Wicker
- e.) “Microstructural Architecture Development in a Cobalt-Base Alloy by Additive Manufacturing Using Electron Beam Melting”, L.E. Murr, S.M. Gaytan, E. Martinez, J.L. Martinez, B.I. Machado, D.A. Ramirez, F. Medina, R.B. Wicker

Papers presented at 140th Annual TMS (The Minerals, Metals and Materials Society) Conference and Exhibition, February 28- March 3, 2011, San Diego CA

- a.) “Materials Characterization of Railgun Erosion Phenomena”, B.I. Machado, L.E. Murr, E. Martinez, S.M. Gaytan, S. Satapathy
- b.) “Characterization of Copper Open Cellular Structures Fabricated by Electron Beam Melting” D.A. Ramirez, L.E. Murr, S.J. Li, E. Martinez, D.H. Hernandez, J.L. Martinez, F. Medina, P. Frigola, and R.B. Wicker
- c.) “Materials with Controlled Microstructural Architecture (MCMA) Fabricated by Electron Beam Melting”, S.M. Gaytan, D.A. Ramirez, L.E. Murr, E. Martinez, J.L. Martinez, D. Hernandez, B.I. Machado, F. Medina, and R.B. Wicker

Papers presented at 22nd International Solid Freeform Fabrication Symposium, August 8-10, 2011 Austin, TX

- a.) “Orthopedic Implant Compatibility Strategies Using Open-Cellular Monolithic Prototypes Fabricated by EBM” K.N. Amato, L.E. Murr, S.J. Li, Y.X. Tian, S.M. Gaytan, E. Martinez, P.W. Shindo, F. Medina, R.B. Wicker
- b.) “Electron Beam Melting: The New Directional Solidification”, E. Martinez, L.E. Murr, S. M. Gaytan, D.A. Ramirez, F. Medina, R.B. Wicker

Papers presented at Materials Science and Technology 2011 Conference & Exhibition (MS&T 2011), October 16-20, 2011 Columbus Ohio

- a.) “Next Generation Orthopedic Implants by Additive Manufacturing Using Electron Beam Melting”, L.E. Murr, S.M. Gaytan, E. Martinez, F. Medina, R.B. Wicker
- b.) “Comparison of Microstructures and Mechanical Properties for CoCrMo Biomedical Implant Prototypes Fabricated by EBM and Failed Implants by Traditional Manufacturing”, S.M. Gaytan, L.E. Murr, E. Martinez, F. Medina, S. Stafford, U. Ackelid, R.B. Wicker
- c.) “Open-Cellular Co-Base and Ni-Base Superalloys Fabricated by Electron Beam Melting”, K.N. Amato, L.E. Murr, S.J. Li, Y.X. Tian, E. Martinez, F. Medina
- d.) “Novel TiAl Open Cellular Structures Fabricated by Electron Beam Melting” J. Hernandez, L.E. Murr, S.M. Gaytan, E. Martinez, S.J. Li. X. Y. Cheng, F. Medina, R.B. Wicker

Papers presented at 141 Annual TMS (The Minerals, Metals and Materials Society) Conference and Exhibition, March 2012, Orlando, FL “Columnar Microstructural Architecture in Electron and Laser Beam Melting of Metals and Alloys” E. Martinez, L.E. Murr, S.M. Gaytan, K.N. Amato, P.W. Shindo, D.A. Ramirez, F. Medina, J.L. Martinez, B.I. Machado, R.B. Wicker

Paper presented at International Conference on 3D Materials Science 2012 July 8-12, 2012, Seven Springs Mountain Resort, Seven Springs, PA, “3D Microstructural Architectures for Metal and Alloy Components Fabricated by 3D Printing/Additive Manufacturing Technologies”, E. Martinez, L.E. Murr, K.N. Amato, J. Hernandez, P.W. Shindo, S.M. Gaytan, D.A. Ramirez, F. Medina, and R.B. Wicker

Paper presented at 142nd TMS (The Minerals, Metals and Materials Society) Conference and Exhibition, March 3-7, 2013, San Antonio, TX “Microstructures for Niobium Fabricated by Electron Beam Melting”, E. Martinez, L.E. Murr, J. Hernandez, X. Pan, K.N. Amato, P. Frigola, C. Terrazas, S.M. Gaytan, E. Rodriguez, F. Medina, and R.B. Wicker

Vita

Edwin Martinez was born and raised in El Paso, Texas. He attended high school at Bel Air High School where he obtained his high school diploma. His bachelor's degree was obtained at the University of Texas at El Paso in Metallurgical and Materials Science and Engineering. As a high school senior he obtained an internship in the Metallurgy department under the supervision of Dr. Lawrence Murr. Throughout his undergraduate education he obtained multiple awards, including the Henry and Margaret F. Ehrlinger Memorial award, and continued to work as a research assistant under Dr. Murr and the W.M. Keck Center. He also has numerous publications as well as presentations which are attached.

Permanent address: 909 Destello
El Paso, TX 79907

This thesis was typed by Edwin Martinez